Prepared for submission to JHEP

Dark matter scattering in astrophysical media: collective effects

William DeRocco,[a] **Marios Galanis,**[b] **Robert Lasenby**[b]

[a] *Santa Cruz Institute for Particle Physics and Department of Physics, University of California, Santa Cruz, 1156 High Street, Santa Cruz, CA 95064*

[b] *Stanford Institute for Theoretical Physics, Stanford University, Stanford, CA 94305, USA*

E-mail: wderocco@ucsc.edu, mgalanis@stanford.edu, rlasenby@stanford.edu

Abstract: It is well-known that stars have the potential to be excellent dark matter detectors. Infalling dark matter that scatters within stars could lead to a range of observational signatures, including stellar heating, black hole formation, and modified heat transport. To make robust predictions for such phenomena, it is necessary to calculate the scattering rate for dark matter inside the star. As we show in this paper, for small enough momentum transfers, this requires taking into account *collective effects* within the dense stellar medium. These effects have been neglected in many previous treatments; we demonstrate how to incorporate them systematically, and show that they can parametrically enhance or suppress dark matter scattering rates depending on how dark matter couples to the Standard Model. We show that, as a result, collective effects can significantly modify the potential discovery or exclusion reach for observations of compact objects such as white dwarfs and neutron stars. While the effects are more pronounced for dark matter coupling through a light mediator, we show that even for dark matter coupling via a heavy mediator, scattering rates can differ by orders of magnitude from their naive values for dark matter masses $\lesssim 100\,\mathrm{MeV}$. We also illustrate how collective effects can be important for dark matter scattering in more dilute media, such as the Solar core. Our results demonstrate the need to systematically incorporate collective effects in a wide range of astroparticle contexts; to facilitate this, we provide expressions for in-medium self-energies for a variety of different media, which are applicable to many other processes of interest (such as particle production).

Contents

1 Introduction

Discovering the microphysical nature of dark matter (DM) is one of the major goals of fundamental physics. All existing evidence for DM comes from its gravitational interactions, but many different types of DM models result in very similar mass distributions over the galactic scales on which gravitational effects are significant, hence cannot be distinguished by their gravitational interactions alone. Consequently, to distinguish between these models, we need to look for signatures of non-gravitational interactions between DM and the Standard Model (SM).

The most obvious approach is to look for interactions of DM with laboratory systems. Many different types of experiments, aiming to detect various kinds of DM candidates, have been proposed and implemented, but so far no unambiguous evidence of DM has been seen. In many models of DM, this is not unexpected. DM that is some combination of too weakly-interacting, too dilute (due to individual particles being too heavy, or being clustered in clumps), too low-mass (so that individual interaction events are not energetic enough to be detected), or too strongly-interacting (so that DM is slowed down by the Earth's atmosphere and the environment surrounding the experiment, resulting in low-energy events) could evade detection in such experiments.

An alternative approach, which may help to detect some of these models, is to look for the effects of DM on astrophysical objects, such as stars. These are much larger and denser than terrestrial targets, and can consequently have larger interaction rates with DM. The main difficulty is how to observe the effects of such interactions. For DM whose leading interaction with SM matter is via scattering, scattering events inside a star can result in the DM losing energy and being captured onto a gravitationally bound orbit. Such DM

particles then have the potential for further interactions in and around the star, leading to a variety of possible observational signatures. These including heating old, cold stellar remnants (either from the kinetic energy of the DM [1–9], or from its annihilation [10–12]), formation of a black hole inside the star [13–23], modification of heat transport [24–31], or others. Since these signatures usually rely on the accumulation of many dark matter particles, rather than detecting a single event, their sensitivity does not fall off at large and small dark matter masses in the same way as laboratory experiments, and they can potentially probe parameter space which would be very difficult to explore on Earth.

To make predictions for these kinds of stellar observables, one needs to calculate the scattering rate of DM inside stars. For scatterings involving large enough momentum transfers, this is a simple particle-by-particle process, as is familiar from WIMP direct detection; the total scattering rate is simply given by $\Gamma \simeq n_{\rm SM}\sigma_{\chi{\rm SM}}v$, where $n_{\rm SM}$ is the number density of SM target particles, $\sigma_{\chi{\rm SM}}$ is the DM-SM scattering cross section, and v is the relative velocity. However, for smaller momentum transfers, it can be important to take into account collective effects which arise due to coherent interactions with multiple particles in the medium. A very familiar example of such an effect is the coherent scattering of particles off of all of the nucleons within a nucleus when the transferred momentum is $\lesssim 100\,{\rm MeV}$. However, for momentum transfers smaller than the inverse spacing between separate nuclei (or separate electrons), more complicated effects can occur, such as screening phenomena, scattering off of collective excitations (e.g. phonons or plasmons), and others. These types of effects have been studied recently in the context of laboratory experiments searching for the scattering of sub-GeV DM [32–35], but have mostly been ignored in existing treatments of DM scattering in stars. In this paper, we consider such effects systematically, and show that they can make parametrically large differences to DM capture rates. Depending on the DM model, these can be either enhancements or suppressions of the capture rate compared to naive calculations.

Calculating these capture rates requires a model of the stellar interior. In some circumstances, such as the dilute, weakly-coupled plasma inside the Sun, this task is relatively simple. In others, such as the strongly-coupled ion lattice in cold white dwarfs, or the highly uncertain state of matter inside neutron stars, it is much more complicated. Given these complications, we do not attempt to provide detailed or comprehensive analyses of stellar models; instead, we work with simplified models of stellar media, and use these to illustrate the physics of collective effects for DM scattering rates. The systematic approach that we present should be valuable for future, in-depth investigations. Even in circumstances where collective effects are not important, our in-medium formalism can simplify calculations involving thermal distributions, as we illustrate in Section 6.1.

In addition to working with simplified models, we also investigate the bounds that can be placed on scattering and capture rates from general properties such as causality. Specifically, for a dark photon mediator, we show how the Kramers-Kronig relations enable us to place bounds on scattering and capture rates (extending the non-relativistic derivation in [35]), and how these bounds let us draw phenomenologically useful conclusions.

Another contribution of this paper is to systematically consider the in-medium behaviour of vector and scalar mediators. In particular, we present formulae for evaluating

one-loop vector and scalar self-energies in both degenerate Fermi gases and dilute non-relativistic plasmas; as far as we are aware, these expressions are novel. We have made code implementing some of these formulae available online.[1] These and similar calculations should be useful in circumstances beyond DM scattering in stars. For example, in-medium self-energies are important in properly computing the emission rates of light hidden-sector particles from hot media such as supernovae [36] (e.g. in Appendix F, we show how previous calculations of electron-coupled scalar emission from supernovae were parametrically incorrect). Our formalism can also be applied to DM scattering in laboratory experiments, as explored in [35].

The outline of the paper is as follows: in Section 2, we outline the computation of scattering rates using in-medium propagators and give specific examples of such rates. In Section 3, we discuss the kinematics associated with stellar capture, after which we apply our computed capture rates to both white dwarfs (Sec. 4) and neutron stars (Sec. 5). We then discuss scattering in dilute stellar plasmas, and ramifications for various potential signatures in the Sun (Sec. 6) before concluding and discussing future directions in Section 7. Various formulae for the processes discussed are collected in Appendices A-E, while Appendix F discusses particle emission from supernovae.

2 Scattering rates and in-medium propagators

A systematic way to calculate the scattering rate for a particle travelling through a medium is to use the effective in-medium propagator for the particle. If we consider a DM particle χ coupled to the SM via a mediator particle X, then this can be related to the effective in-medium propagator for the mediator X. Diagramatically, at leading order in the (assumed weak) $X-\text{SM}$ and $\chi - X$ couplings, the scattering rate can be related to the imaginary part of the following self-energy diagram,

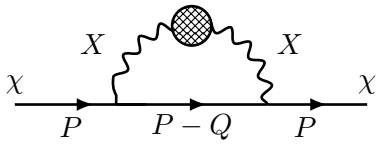

where the filled circle represents the medium (this usually consists of SM particles, but if there is a large density of DM particles, e.g. if DM self-capture in a star is important, then it could include DM as well).[2] Via the optical theorem, the imaginary part of the self-energy corresponds to the scattering rate via mediator exchange with the medium,

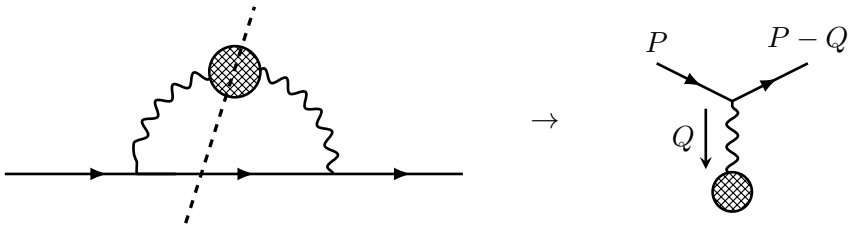

(2.1)

[1] github.com/wderocco/DarkScatter

[2] While we have drawn the mediator X as a vector, it may be a vector or a scalar.

For the explicit example of Dirac fermion DM, scattering via a vector mediator of mass m_X, the total scattering rate, integrating over momentum transfers Q, is given by (Appendix A)

$$\Gamma = \frac{2g_\chi^2}{E}\int \frac{d^3q}{(2\pi)^3}\frac{1}{2E'}(1+f(q_0))\frac{1}{(Q^2-m_X^2)^2}\times \\ \left(2\left(E^2-p^2\cos^2\theta\right)\mathrm{Im}\,\Pi_L^X(Q)-\left(-Q^2+2p^2\sin^2\theta\right)\mathrm{Im}\,\Pi_T^X(Q)\right) \tag{2.2}$$

where g_χ is the DM-mediator coupling, $P=(E,p)$ is the initial 4-momentum of the DM particle, $Q=(q_0,q)$ is the scattering 4-momentum, $E'=E-q_0$ is the post-scattering DM energy, $f(q_0)\equiv(e^{q_0/T}-1)^{-1}$ is the bosonic occupation number corresponding to the temperature T of the medium, θ is the angle beteween p and q, $\Pi_L^X(Q)$ is the in-medium self-energy for the longitudinal mode of X, and $\Pi_T^X(Q)$ is for the transverse mode (Eq. (2.2) assumes a uniform, isotropic medium).[3] Eq. (2.2) computes the total scattering rate for a DM particle passing through a spatially uniform medium; we can compute other quantities of interest, such as the scattering rate into particular parts of phase space or the momentum transfer rate, via similar expressions, as we discuss below. There are also similar expressions for other kinds of DM particles (e.g. spin-0 DM) and other types of mediators; for more details, see Appendix A.

We have seen how, to compute the DM scattering rate, we want to compute the mediator self-energy in an SM medium. If we have some perturbative description of the SM medium[4], then to leading order in the (assumed weak) SM-mediator coupling, the self-energy is given diagramatically by

(2.3)

where the single-hatched circles on the RHS correspond to one-particle irreducible self-energies, while the bold line corresponds to the in-medium SM photon propagator.[5] Algebraically,

$$\Pi^{XX}_{\mathrm{tot}} = \Pi^{XX} + \frac{(\Pi^{XA})^2}{Q^2-\Pi^{AA}} \tag{2.4}$$

where Π^{XX} and Π^{AA} correspond to the 1PI self-energies, and Π^{XA} to the 1PI mixing self-energy (all self-energies are functions of Q). Eq. (2.4) is schematic, in that the SM photon propagator has vector indices, $D_{\mu\nu}(Q)$, but for an isotropic medium, it will split

[3] Eq. (2.2) assumes that the SM current that X couples to is conserved — more specifically, that current-nonconserving processes are unimportant in the medium. If X does not have flavour-changing couplings, then this is a good approximation at the very sub-weak-scale temperatures in astrophysical media.

[4] This does not necessarily have to be in terms of 'bare' SM particles, but can be in terms of weakly-interacting quasi-particles, e.g. Fermi liquid theory [37].

[5] In principle, we should sum over all SM intermediate states allowed by symmetries. In this paper, we will consider spin-0 and spin-1 mediators, so we are interested in bosonic SM states with no conserved SM quantum numbers. At low energies, this picks out the photon; if we are working in an EFT including the pion, then we can have mixing between a pseudoscalar mediator and the pion, but we will not consider such cases. If we were working in an effective description of the medium that included excitations such as phonons, then these should also be included in the intermediate states.

into longitudinal and transverse parts, each of which can be put into the form of Eq. (2.4) (see Appendix A).

Taking the imaginary part of Eq. (2.4), we obtain

$$\mathrm{Im}\,\Pi^{XX}_{\rm tot} = \Pi^{XX}_i + \frac{\Pi^{AA}_i((\Pi^{XA}_r)^2 - (\Pi^{XA}_i)^2) + 2\Pi^{XA}_r\Pi^{XA}_i(Q^2 - \Pi^{AA}_r)}{(Q^2 - \Pi^{AA}_r)^2 + (\Pi^{AA}_i)^2} \tag{2.5}$$

where Π_r, Π_i indicate the real and imaginary parts of each self-energy. A naive calculation, ignoring collective effects, usually corresponds to the leading-order parts of the Π^{XX}_i term. Diagramatically, cutting the simplest two-loop self-energy diagram corresponds to the leading-order particle-by-particle scattering rate,

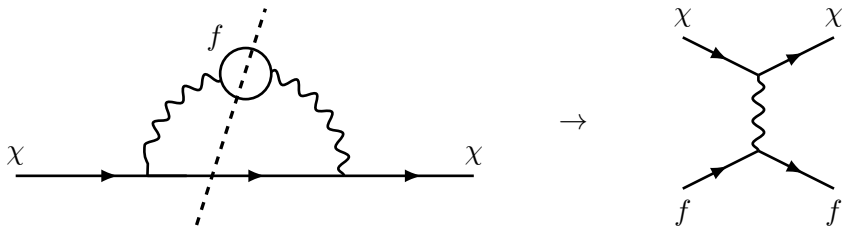

(2.6)

with in-medium initial-state and final-state occupation number factors for f. The other term in Eq. (2.5) corresponds to the 'mixing' contributions to the scattering rate. These can sometimes cancel against the Π^{XX}_i term, resulting in a suppressed scattering rate, or can enhance it, e.g. if the denominator becomes small (giving 'resonant' effects). This is similar to the situation in particle emission calculations [36].

A simple model of phenomenological interest is a 'dark photon' mediator [38], where X is a massive vector which couples to the SM electromagnetic current, $\mathcal{L} \supset \kappa X_\mu J^\mu_{\rm EM}$, with coupling suppressed by the 'kinetic mixing' parameter κ. In this case, we simply have that $\Pi^{AX} = \kappa\Pi^{AA}$ and $\Pi^{XX} = \kappa^2\Pi^{AA}$, so writing $\Pi \equiv \Pi^{AA}$, we have

$$\mathrm{Im}\,\Pi^{XX}_{\rm tot} = \frac{\kappa^2 Q^4\,\mathrm{Im}\,\Pi}{(\mathrm{Re}\,\Pi - Q^2)^2 + (\mathrm{Im}\,\Pi)^2} = \frac{\kappa^2 Q^4\,\mathrm{Im}\,\Pi}{|Q^2 - \Pi|^2} \tag{2.7}$$

We can see that, for large momentum transfers with $|Q^2| \gg |\Pi|$, we have $\mathrm{Im}\,\Pi^{XX}_{\rm tot} \simeq \kappa^2\,\mathrm{Im}\,\Pi$; at leading order, this corresponds to the naive particle-by-particle scattering rate from Eq. (2.6). Collective effects are important when the Π terms in the denominator of Eq. (2.7) are significant. These can either lead to suppression, if $|\Pi| \gg |Q^2|$ (generally referred to as 'screening'), or enhancement, if $Q^2 - \mathrm{Re}\,\Pi \simeq 0$ contributes significantly to the scattering ('resonant' effects).

Analogous analyses apply to other types of mediator, such as scalars. One important general point is that whether medium effects are important depends on the comparison of $|Q^2|$ to $|\Pi(Q)|$, *not* on the comparison between $|Q^2|$ and m_X^2, as is sometimes assumed. In particular, we will see how collective effects can sometimes be very important for scattering via a heavy mediator (corresponding to contact interactions in the low-energy theory).

2.1 EM sum rules

For a dark photon mediator, the expression in Eq. (2.7) corresponds to $\mathrm{Im}(\Pi^{XX}_{\rm tot})_{\mu\nu} = \kappa^2 Q^2\,\mathrm{Im}\,(-iD_{\mu\nu})$, where $D_{\mu\nu}$ is the in-medium propagator for the SM photon, in Lorenz

gauge (more precisely, it is the analytic continuation of the in-medium imaginary-time propagator — see Appendix D). We can also see this directly [39] by changing variables to put the mediator-SM interaction into kinetic mixing form, $\mathcal{L} \supset -\frac{\kappa}{2} F_{\mu\nu} F'^{\mu\nu}$, where F' is the field strength corresponding to A'. Then,

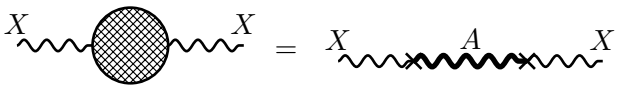

(2.8)

where the crosses correspond to the kinetic mixing interaction. Here, all of the interactions with the medium have been subsumed into the in-medium propagator for the SM photon. Since the properties of the in-medium propagator $D_{\mu\nu}$ are constrained by causality, we can place limits on the scattering rate via a dark photon mediator, as discussed (for non-relativistic DM) in [35]. We go through the derivation of such limits in Appendix D. For example, to derive limits on scattering rates via longitudinal vector exchange, we can use the Kramers-Kronig relations [40] to derive the sum rule

$$\int_0^\infty \frac{dq_0}{q_0} \frac{Q^2}{q^2} \operatorname{Im} D_L(q_0, q) = \frac{\pi}{2} \frac{k_S^2}{q^2(q^2 + k_S^2)} \tag{2.9}$$

where $k_S^2 \equiv \Pi_L(0, q)$ is the (static) longitudinal screening scale. In the circumstances that will be of interest to us, we will usually have $k_S^2 \geq 0$, corresponding to screening rather than anti-screening (see Appendix D), so we can upper-bound Eq. 2.9 by $\pi/(2q^2)$.

Since, for a dark photon mediator, $\operatorname{Im}(\Pi_{\text{tot}}^{XX})_{\mu\nu} = \kappa^2 Q^2 \operatorname{Im}(-iD_{\mu\nu})$, and the DM scattering rate can be written in terms of an integral over $\operatorname{Im}\Pi^X(Q)$ for different Q (Eq. (2.2)), we can use Eq. (2.9) (and an analogous sum rule for the transverse propagator) to bound the DM scattering rate. Specifically, we can write the scattering rate as a nested integral of the form $\int \cdots \int \frac{dq_0}{q_0} \frac{Q^2}{q^2} \ldots \operatorname{Im} D_L(q_0, q)$, and then upper-bound the $\int \frac{dq_0}{q_0}$ integral by assuming that $D_L(q_0, q)$ (for given q) is a delta-function at the value maximizing the rest of the integrand, with the delta-function's weight set by Eq. (2.9) (see Appendix D for details). For a non-relativistic DM particle χ with velocity $v_\chi \ll 1$, and taking the temperature to be negligible, this implies that the scattering rate via longitudinal mediator exchange is upper-bounded by

$$\Gamma_L \lesssim \begin{cases} \dfrac{g_\chi^2 \kappa^2}{4\pi} m_\chi v_\chi & m_X \ll m_\chi v_\chi \\ \dfrac{16}{15} \dfrac{g_\chi^2 \kappa^2}{4\pi} m_\chi v_\chi \left(\dfrac{m_\chi v_\chi}{m_X} \right)^4 & m_X \gg m_\chi v_\chi \end{cases} \tag{2.10}$$

where we give the forms for very light and very heavy mediators (compared to the DM momentum scale). The scattering rate limit via transverse mediator exchange is further suppressed by v_χ^2 compared to the longitudinal rates:

$$\Gamma_T \lesssim \begin{cases} 0.53 \times \dfrac{g_\chi^2 \kappa^2}{4\pi} m_\chi v_\chi^3 & m_X \ll m_\chi v_\chi \\ 1.16 \times \dfrac{g_\chi^2 \kappa^2}{4\pi} \dfrac{m_\chi^5 v_\chi^7}{m_X^4} & m_X \gg m_\chi v_\chi \end{cases} \tag{2.11}$$

as follows from the form of Γ_T (Appendix A). For relativistic χ, the rate limits will be larger than these formulae; see Appendix D. We can also use similar arguments to place sum rule limits on other quantities, such as total capture rates, as we discuss in the next Section. As we will see in Sections 4 and 5, these limits allow us to set reliable bounds on the scattering rate through a dark photon mediator, even without using an explicit model of the stellar medium.

3 Stellar capture rates

We can use the formalism for calculating scattering rates outlined in Section 2 to calculate quantities of physical interest, such as the capture rate for halo DM into gravitationally bound orbits in and around a star. For situations in which the star is optically thin, and capture is dominated by individual scattering events, the capture rate can be derived from the DM velocity distribution at each point inside the star, that arises from the infall under gravity of halo DM.

At a given point inside the star, an infalling halo DM particle with energy E (as measured by a stationary observer at that point) had energy $E_\infty = \sqrt{B}E$ far from the star, where $\sqrt{B}$ is the gravitational redshift at that point ($B = g_{00}$ in Schwarzschild coordinates). In most circumstances of interest, an isotropic halo DM velocity distribution leads to an isotropic distribution of infalling DM at points inside the star.[6] Consequently, if we assume for simplicity that the halo DM velocity distribution is isotropic, with phase space density $f_\infty(E_\infty)$, then since (from Liouville's theorem) the phase space density is preserved during gravitational infall, the phase space density at a point inside the star is set by $f(E) = f_\infty(\sqrt{B}E)$.

We can relate f_∞ to the velocity distribution of halo DM by noting that we must have

$$n_\chi = g_s \int \frac{d^3p}{(2\pi)^3} f_\infty = \frac{g_s m_\chi^3}{(2\pi)^3} \int d^3v f_\infty \quad \Rightarrow \quad f_\infty(p) = (2\pi)^3 \frac{n_\chi}{g_s m_\chi^3} p_v(p/m_\chi) \tag{3.1}$$

where we have taken the halo DM to be non-relativistic, g_s is the spin degeneracy of the DM, and $p_v(v)$ is the halo DM velocity distribution. Going forwards, we will define $\hat{f}_\infty \equiv g_s f_\infty/(2\pi)^3 = \frac{n_\chi}{m_\chi^3} p_v(p/m_\chi)$ for notational convenience (and more generally, $\hat{A} \equiv \frac{g_s}{(2\pi)^3} A$ for other quantities A).

[6] The halo DM velocity distribution at a point inside the star is isotropic as long as there are not bound orbits inside the star with $E_\infty > m_\chi$ (i.e. with $P_0 > m_\chi$, where P is the 4-momentum in Schwarzschild coordinates), which we will call 'positive orbits'. In Newtonian gravity, positive orbits are not possible. At a given point inside the star, all test particle trajectories with a given energy either escape to infinity, if the total energy (kinetic plus potential) is non-negative, or enter bound orbits, if the total energy is negative. In particular, the direction of the trajectory does not affect whether it is escaping or bound. This is not necessarily true in GR, for sufficiently compact objects. If some of the trajectories passing through a point inside the star form positive orbits, then infalling halo DM cannot travel along these trajectories, even though the total energy might be $\geq m_\chi$; it can only travel along escaping trajectories. As we discuss at the end of this Section, heavy neutron stars may be just compact enough for positive orbits to exist. However, even for e.g. the heaviest neutron star model from [41], positive orbits can only exist in a small volume of phase space near the edge of the star. Consequently, their existence cannot have a large effect on our capture rate calculations, and we ignore them here.

In terms of $f(E)$, the scattering rate per volume at a point within the star, considering only scatterings from unbound to bound orbits, is (as measured by a stationary local observer)

$$\frac{\Gamma}{\text{vol}} = g_s \int \frac{d^3p}{(2\pi)^3} f(p) \Gamma_{E\to E'<E_{\rm esc}} = 4\pi \int dE\, Ep\, \hat{f}(E) \Gamma_{E\to E'<E_{\rm esc}} \tag{3.2}$$

where $\Gamma_{E\to E'<E_{\rm esc}}$ indicates the scattering rate into bound orbits (with energy $< E_{\rm esc} = m_\chi/\sqrt{B}$), and we have assumed that the DM velocity distribution is isotropic, so that f is only a function of E (if the DM distribution is non-isotropic but the medium's response is isotropic, then we can equivalently consider averaging over different orientations to obtain an isotropized velocity distribution — see Appendix E). Writing this in terms of E_∞, we have

$$\begin{aligned}\frac{\Gamma}{\text{vol}} &= 4\pi B^{-3/2} \int_{m_\chi}^{\infty} dE_\infty\, E_\infty^2 \sqrt{1 - \frac{m_\chi^2 B}{E_\infty^2}}\, \hat{f}_\infty(E_\infty) \Gamma_{E\to E'<E_{\rm esc}} \\ &\simeq 4\pi \frac{\sqrt{1-B}}{B^{3/2}} m_\chi^2 \int_{m_\chi}^{\infty} dE_\infty\, \hat{f}_\infty(E_\infty) \Gamma_{E\to E'<E_{\rm esc}}\end{aligned} \tag{3.3}$$

where in the second line we used that the halo DM is non-relativistic, so $E_\infty \simeq m_\chi$. This is the *local* rate, as measured by a stationary observer inside the star; due to time dilation, the total capture rate, as measured by a stationary observer at infinity, is

$$C = 4\pi m_\chi^2 \int dV \frac{v_{\rm esc}}{B} \int_{m_\chi}^{\infty} dE_\infty \hat{f}_\infty(E_\infty) \Gamma_{E\to E'<E_{\rm esc}} \tag{3.4}$$

If the escape velocity $v_{\rm esc} = \sqrt{1-B}$ inside the star is much greater than the velocity dispersion of the incoming DM, then the kinetic energy of DM in the star will be dominated by the energy acquired during its infall and almost all of the halo DM particles at a point inside the star will have energy just above $E_{\rm esc}$. In some circumstances, this will mean that $\Gamma_{E\to E'<E_{\rm esc}}$ can be treated as approximately constant over the small range of relevant E, and we can take it out of the $\int dE_\infty$ integral. This is not always possible; if soft scatterings are strongly enhanced, as they can be for light mediators, then how close a particle's energy is to the $E_{\rm esc}$ threshold can make a significant difference to the capture rate. However, if we can take $\Gamma_{E\to E'<E_{\rm esc}}$ outside the integral (e.g. if hard scatterings dominate the capture rate), then

$$\begin{aligned}C &\simeq 4\pi m_\chi^2 \int dV \frac{v_{\rm esc}}{B} \Gamma_{\rm down-scatter} \int_0^{\infty} v_\infty dv_\infty \hat{f}_\infty(v_\infty) \\ &= n_\chi \left\langle \frac{1}{v_\infty} \right\rangle \int dV \frac{v_{\rm esc}}{B} \Gamma_{\rm down-scatter}\end{aligned} \tag{3.5}$$

where $\Gamma_{\rm down-scatter}$ is the rate of scatterings from higher to lower energies for a DM particle with velocity $v_{\rm esc}$, v_∞ is the DM velocity at infinity, and the angle brackets denote the average over the DM velocity distribution at infinity. Eq. 3.5 matches the capture rate expression from [41].

If we cannot take $\Gamma_{E\to E'<E_{\rm esc}}$ outside the $\int dE_\infty$ integral, it is still possible to simplify Eq. (3.4). For clarity, we will consider the explicit example of spin-1/2 DM scattering through the longitudinal mode of a vector mediator, which gives a contribution to the capture rate of

$$\frac{dC}{dV} = \frac{2g_\chi^2}{\pi}\frac{v_{\rm esc}}{B}m_\chi^2\int_{m_\chi}^\infty dE_\infty \hat{f}_\infty(E_\infty)\frac{1}{Ep}\int dq\, q \int_{E-E_{\rm esc}}^{q_{0,\rm max}} dq_0(1+f(q_0))\frac{1}{(Q^2-m_X^2)^2}(E^2-p^2\cos^2\theta)\,\mathrm{Im}\,\Pi_L^X(q_0,q) \tag{3.6}$$

where $q_{0,\rm max}$ is the maximum value of q_0 possible for given q and E, derived by taking the outgoing χ to be on-shell. Here, we are taking the mediator self-energy to be isotropic, i.e. to be independent of the direction of q — for non-isotropic media, this can be viewed as the average over different directions for q. If the escape velocity inside the star is much larger than the typical halo DM velocity, then $q_{0,\rm max}$ and $E^2-p^2\cos^2\theta$ will depend only weakly on E_∞. Consequently, the E_∞ dependence of the $\int dq_0$ integral arises mostly from the E_∞ dependence of its lower limit, $E-E_{\rm esc}=(E_\infty-m_\chi)/\sqrt{B}$ (if the energy transfer is below this limit, the DM will still have enough energy left over to escape the star after the collision). So, denoting the kinetic energy of the DM far from the star as $E_K\equiv E_\infty-m_\chi$, we have

$$\begin{aligned}\int_{m_\chi}^\infty dE_\infty \hat{f}_\infty(E_\infty)\int_{(E_\infty-m_\chi)/\sqrt{B}}^{q_{0,\rm max}} dq_0 &\simeq \int_0^{q_{0,\rm max}} dq_0\left(\int_0^{\sqrt{B}q_0} dE_K\,\hat{f}_\infty(m_\chi+E_K)\right)\\ &\equiv \int_0^{q_{0,\rm max}} dq_0 \hat{F}_\infty(\sqrt{B}q_0)\end{aligned} \tag{3.7}$$

Consequently,

$$\frac{dC}{dV} \simeq \frac{2g_\chi^2}{\pi}\int dq\, q\int_0^{q_{0,\rm max}} dq_0\hat{F}_\infty(\sqrt{B}q_0)(1+f(q_0))\frac{1}{(Q^2-m_X^2)^2}(E^2-p^2\cos^2\theta)\,\mathrm{Im}\,\Pi_L^X \tag{3.8}$$

Appendix E gives explicit expressions for $\hat{F}_\infty$ for an (offset) Maxwell velocity distribution. For q_0 much larger than typical halo DM kinetic energies, we have

$$\hat{F}_\infty(q_0)\simeq\hat{F}_\infty(\infty)=\frac{n_\chi}{4\pi m_\chi^2}\left\langle\frac{1}{v_\infty}\right\rangle \tag{3.9}$$

corresponding to Eq. (3.5). For q_0 much smaller than such values, we have $\hat{F}_\infty(q_0)\simeq\frac{n_\chi}{m_\chi^3}p_v(0)q_0$, so the small-energy-transfer capture rate is linearly suppressed in q_0. This corresponds to there being fewer DM particles with energy close enough to $E_{\rm esc}$ to be trapped by losing energy q_0.

For a dark photon mediator, we can use these formulae to place sum rule bounds on the total capture rate, similarly to the bounds on the scattering rate per volume from Section 2.1. These are applied in Sections 4.6 and 5.

Eq. (3.8) contains a factor of $1+f(q_0)=(1-e^{-q_0/T})^{-1}$, so for energy transfers $\lesssim$ the temperature T of the stellar medium, the down-scattering rate from unbound to bound

orbits is enhanced by $\sim \frac{T}{q_0}$. However, this also means that up-scatterings from bound to unbound orbits can be important. When T is large enough that the $q_0 \lesssim T$ phase space becomes important, we are not necessarily just interested in the rate of unbound-to-bound scatterings. Often, we are interested in the properties of the dynamic equilibrium which arises once enough dark matter has been captured that up-scatterings from bound orbits become significant. To understand this behaviour properly, one would generally need a full model of the capture and evolution of DM within the star. Here, we will not attempt to do that, but will note when energy transfers $q_0 \lesssim T$ are important for capture rates (e.g. Solar capture via a light mediator, Sec. 6.1).

3.1 Geometric capture rate

The $C = \int dV \frac{dC}{dV}$ formula for the total capture rate derived above holds when the star is optically thin to DM. If, on the other hand, the star is optically thick, then the maximum possible value for the capture rate is given by the geometric rate, i.e. the rate at which halo DM particles intersect with the star. To compute this correctly, one needs to take into account gravitational focusing. For $R > 4GM$, where R is the radius of the star and M is its mass, a trajectory grazing the star's surface can come from and escape to infinity. The angular momentum (per unit mass) of such a trajectory is $L = \sqrt{\frac{2R_g R}{1-2R_g/R}}$, where $R_g \equiv GM$. For a DM particle with velocity at infinity v_∞, the corresponds to impact parameter $b_{\max} = L/v_\infty$, so the geometric capture rate is [13]

$$C = \left\langle \pi b_{\max}^2 n_\chi v_\infty \right\rangle = \frac{2\pi R_g R}{1 - 2R_g/R} n_\chi \left\langle \frac{1}{v_\infty} \right\rangle \tag{3.10}$$

where the angle brackets denote averaging over the DM velocity distribution at infinity. If the star is more compact, so $R \leq 4GM$, then trajectories grazing the star's surface are bound; all incoming-from-infinity DM trajectories have inwards radial velocity, and the geometric capture rate is the same as an object with radius $R = 4GM$, giving

$$C = 16\pi R_g^2 n_\chi \left\langle \frac{1}{v_\infty} \right\rangle \tag{3.11}$$

i.e. the same rate as a black hole. Only the heaviest neutron stars have radius close to the $4GM$ threshold, so in general, the expression from Eq. (3.10) will be fine for our purposes. For dense stellar remnants such as white dwarfs and neutron stars, capture rates not too far from the geometric limit are often needed to obtain observable signatures, as we discuss in subsequent sections.

4 White dwarfs

White dwarfs are the densest astrophysical objects whose physics we understand fairly well (as we discuss in Section 5, the physics of neutron star cores is very poorly understood). Consequently, they represent a promising target for signatures of DM scattering, with the potential for large and reliably-computable scattering rates. In this Section, we will discuss how to perform such computations for some representative DM models, and how such

scatterings might lead to observational signatures. We begin by briefly summarizing some of the signatures of DM capture in white dwarfs proposed in the existing literature, before outlining our calculations of the DM capture rate in white dwarfs. At low DM masses, we find that this rate is dominated by collective scattering with longitudinal phonons, which we calculate analytically. We discuss a number of different DM mediator models; heavy vector mediators, light dark photon mediators, and heavy scalar mediators.

4.1 Observational signatures

DM scattering in a white dwarf (WD) can lead to a variety of possible observational consequences. The simplest such signature is heating of the star. Old WDs are expected to cool down to temperatures $\mathcal{O}(10^5\,\mathrm{K})$ [42] in their cores; their thin outer layers are significantly cooler, at temperatures $\sim$ few $\times\, 10^3\,\mathrm{K}$ [43]. If enough of the energy carried by DM can be deposited into a WD, then in regions of sufficiently high DM density, the WD's temperature could be appreciably raised.

Since the escape velocity in a WD is non-relativistic, the kinetic energy carried by infalling DM is only a small fraction (at most $\sim 10^{-2}$) of its total energy. Consequently, very large ambient DM densities would be required for purely kinetic heating of WDs to be significant, even at the geometric capture rate. One way to deposit more energy is for captured DM to annihilate inside the WD [11, 44–46]. After the initial scattering event that captures a DM particle into a bound orbit, further scatterings will cause the particle to lose more energy, thermalizing it down into a smaller volume within the WD, where it may annihilate with other captured DM particles. In most models, the cross sections required to capture enough DM for detectable heating mean that these subsequent stages of thermalization and annihilation always happen fast enough to set up an equilibrium between DM capture and annihilation. In particular, to capture enough DM, capture rates not too far from the geometric limit are usually required [46]. Consequently, to calculate the heating rate, we just need to calculate the DM capture rate, as discussed in Section 2.

Other possible signatures include, for example, the formation of black hole inside the WD, destroying it from the inside [14], which is possible for sufficiently heavy, bosonic, asymmetric DM. To understand this process, one needs to understand the initial capture of the DM, and its subsequent scattering inside the WD, both with the SM medium and with other DM particles. Alternatively, the decay of very heavy DM particles inside WDs [47] (or other kinds of energy injection processes [48, 49]) could ignite supernovae. We leave analysis of such possibilities to future work.

4.2 Scattering calculations

Depending on its composition and temperature, the matter in a WD core can exist in different states [50, 51]. In this paper, our focus will be on illustrating the physics of collective effects, rather than performing detailed or comprehensive phenomenological investigations. Accordingly, we will focus on a particular nominal WD model, and leave investigations of broader parameter space to future work.

As discussed in [46], the best prospects for detecting WD heating signatures appear to come from the heaviest WDs. Consequently, we will take as our nominal model the

heaviest WD model considered in [46]. This has basic parameters

$$M_* \simeq 1.38 M_\odot \quad R_* \simeq 1250\,\text{km} \quad v_{\text{esc,core}} \simeq 0.1 \quad \rho_{\text{core}} \simeq 10^{10}\,\text{g}\,\text{cm}^{-3} \quad \mu_{e,\text{core}} \simeq 8\,\text{MeV} \tag{4.1}$$

where M_* is the WD mass, R_* is its radius, and $v_{\text{esc,core}}$, ρ_{core}, and $\mu_{e,\text{core}}$ are the escape velocity, density, and electron chemical potential in the WD core. We will assume that the WD is old, with core temperature $T_{\text{core}} \simeq 10^5\,\text{K}$. [46] takes the core to be composed entirely of carbon ions and electrons; at such low temperatures; the core consists of a lattice of carbon nuclei, embedded in a degenerate electron gas. This is very analogous to a typical metal; the major differences are that the ions in the WD are bare nuclei, and the electrons are at much higher (relativistic) velocities.

The most comprehensive previous study of DM scattering in WDs appears to be [46]. This takes into account Pauli blocking for scattering off electrons, but does not consider other collective effects. As discussed in Section 2, this corresponds to calculating the scattering rate using the leading-order part of the 1PI self-energy $\text{Im}\,\Pi_L^{XX}$ (Eq. (2.6)), and ignoring the 'mixing' contributions. We will see that, even for the heavy-mediator case that [46] considered, collective effects can make significant differences to the scattering rates for DM lighter than $\sim 100\,\text{MeV}$. For DM scattering through a light mediator, collective effects are important up to much higher masses.

To compute scattering rates properly, the first quantity we need to calculate is the photon self-energy in the WD medium. The leading-order electron contribution is fairly simple, being very well-approximated by that of a fully degenerate ($T \ll \mu_e$), free electron gas (see Appendix B.3). To check that the free approximation is good, we can compare the Coulomb interaction energy between electrons to their kinetic energy; for a relativistic electron gas, this gives

$$\frac{e^2/r_s}{E_F} \sim e^2 \left(\frac{2}{9\pi}\right)^{1/3} v_F \simeq 4 \times 10^{-2} \ll 1 \tag{4.2}$$

where E_F is the electron Fermi energy, v_F is the Fermi velocity, and r_s is the 'typical distance' between electrons, defined via $n_e^{-1} = \frac{4}{3}\pi r_s^3$. This ratio being small corresponds to interactions acting as a small perturbation [52].[7] The leading-order formulae for the contribution to $\Pi^{AA}(Q)$ from a degenerate fermion gas are given in Appendix B.3 — as far as we are aware, the exact forms for the leading-order self-energy that we present have not been derived previously.

The contribution to $\Pi^{AA}(Q)$ from the ions is somewhat more complicated, since Coulomb interactions are strong enough to make the ions form a lattice [52]; approximating them as a free, non-relativistic gas will not always be viable. In particular, for q_0 smaller than the lattice band gap (which for our nominal parameters will be $\mathcal{O}(50\,\text{keV})$ [54]), we expect the ion contribution to the imaginary part to vanish as incoming DM cannot transfer sufficient energy to excite ions above the lattice band gap. Additionally, for q comparable

[7] This in contrast to the situation in e.g. metals, where this ratio is typically $\sim 2-3$ [53]. The electron gas in a metal can still be analyzed in terms of weakly-interacting quasi-particles with renormalized parameters, using Fermi liquid theory [37].

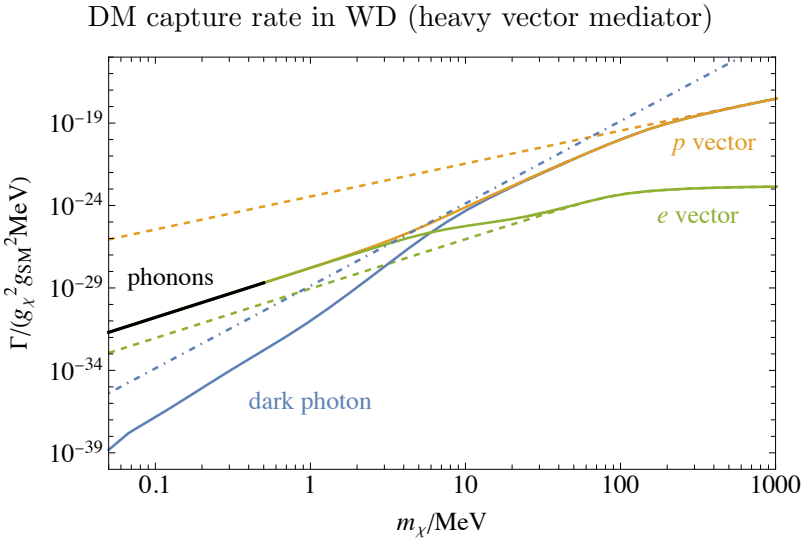

Figure 1. Rates for down-scattering to a gravitationally-bound orbit in the core of a heavy WD, for a DM particle with halo velocity $v_\infty = 10^{-3}$, coupling through a heavy (m_X = TeV) vector mediator. The blue curve corresponds to a dark photon mediator, the green curve to an electron-coupled vector, and the orange curve to a proton-coupled vector. The dashed green and orange curves correspond to calculations ignoring collective effects, while the solid curves take collective effects into account — as can be seen from the plot, the solid curves match up with the dashed curves at high enough DM masses, where scattering is dominated by momentum transfers above screening scales. The dot-dashed blue curve corresponds to the sum rule limit (Section 2.1) on the scattering rate for a dark photon mediator; as expected, the dark photon curve lies below this limit. The dark photon rate is also well below those for other mediators at small DM masses, due to charge screening in the WD. The black curve labelled 'phonons' corresponds to the rate for resonantly scattering into longitudinal phonons, given by Eq. (4.12). As derived in Section 4.3, the scattering rate for proton- and electron-coupled vector mediators is dominated by scattering into longitudinal phonons at small DM masses, accounting for the green and orange curves matching onto the black curve at low DM masses.

to lattice scales, the self-energy will be non-isotropic, since the lattice picks out preferred directions.

One could treat the ion lattice properly via e.g. a density functional theory calculation, of the type performed in [55, 56]. Here, we will work with simpler approximations. For large momentum transfers, we will treat the ions as a free, dilute, non-relativistic gas (see Appendix B.4). For small momentum transfers, we will use the zero-velocity approximation $\Pi_L(Q) \simeq \omega_i^2 Q^2/q_0^2$, where $\omega_i^2 \equiv e^2 Z_i^2 n_i/m_i$ is the ion plasma frequency, with Z_i the ion charge, n_i the ion number density, and m_i the ion mass (this will be valid for q much smaller than inverse lattice scales, and q_0 much smaller than the lattice band gap). This is how the ion lattice in a metal is treated in basic condensed-matter calculations for longitudinal excitations in metals [57]. Figure 1 shows the resulting scattering rates for different kinds of heavy vector mediators[8], where for DM masses $m_\chi \geq 25\,\text{MeV}$ we use the free ion gas

[8]These rates are computed by numerical integration of Eq. (A.7), with $\text{Im}\,\Pi_L^X(Q)$ computed using the

approximation, while for $m_\chi \leq 45\,\mathrm{MeV}$ we use the zero-velocity approximation. In the overlap regimes, the different curves match up well enough (to within $\sim 1\%$) that the difference is invisible on the plot, suggesting that a proper treatment of the ion lattice would also show similar behaviour.

The very low WD core temperatures we are considering, along with the large WD escape velocity, mean that DM evaporation will only be important for rather small DM masses [46, 58]. Quantitatively, if DM thermalizes in the WD core, its thermal velocity dispersion is $\sigma_\chi \simeq 10^{-2}\sqrt{T/10^5\,\mathrm{K}}\sqrt{100\,\mathrm{keV}/m_\chi}$, compared to the escape velocity $v_{\mathrm{esc}} \simeq 0.1$. [46] finds that, for this nominal WD model, evaporation becomes significant for DM masses $m_\chi \lesssim 50\,\mathrm{keV}$, in agreement with these parametrics.

While numerical calculations like those in Figure 1 are, in some sense, all that we need to make predictions, it is important to understand the physics behind these behaviours. To that end, Figure 2 plots the imaginary part of the longitudinal photon propagator. For large momentum transfers (for which we approximate the ions as a free gas), illustrated in the left-hand panel, the imaginary part is dominated by an electron scattering component at small q, and an ion scattering component with $q_0 \simeq \frac{q^2}{2m_i}$ (the latter dominates the rate for $m_\chi \gg E_F$).[9] The electron Fermi momentum sets the width of the electron-scattering band; for $q \gg m_e$, we must have $q - q_0 \lesssim 2E_F$ in order for up-scattering from inside the Fermi sea to be kinematically possible (see Appendix B.3). For smaller momentum transfers, illustrated in the right-hand panel, the dominant feature is the longitudinal phonon pole (this plot looks almost the same for both free gas and zero-velocity ion models). As we derive below, resonant scattering into these longitudinal phonons dominates the scattering rate at small DM masses, and we can obtain analytic expressions for this rate.

For a vector mediator, there will also be contributions to the scattering rate from transverse modes. However, since transverse modes couple to the DM particle current rather than the particle density, these rates are suppressed by $v_{\mathrm{esc}}^2 \sim 10^{-2}$ relative to the longitudinal contributions, and only compete when the longitudinal modes are heavily screened (which can occur for light DM scattering through a dark photon mediator, as we discuss in Section 4.6).

4.3 Longitudinal phonons

As noted above, our nominal WD core consists of an ionic lattice embedded in a degenerate electron gas, and is very analogous to a metal. Its collective excitations are correspondingly similar to those of a metal; in particular, the low-energy collective excitations are phonons (compression and shear waves). Since the ions are expected to form a BCC lattice [52], only the acoustic modes are expected to be present, rather than additional optical phonon

formulae given in Appendix B. The Π^{XX} and Π^{XA} contributions are computed analogously to Π^{AA}.

[9] Properly, at momentum transfers $q \gtrsim 100\,\mathrm{MeV}$, the finite size of the carbon ions will start to become important. We neglect these effects for simplicity; as we will see below, they are generally not important for parameter space in which collective effects are significant. For example, in Figure 1, we see that the no-mixing calculations match up well with full calculations for $m_\chi \gtrsim$ few $\times\, 100\,\mathrm{MeV}$. Since the escape velocity in the WD core is $\simeq 0.1$, we need DM masses $m_\chi \gtrsim$ GeV for ion form factors to be important.

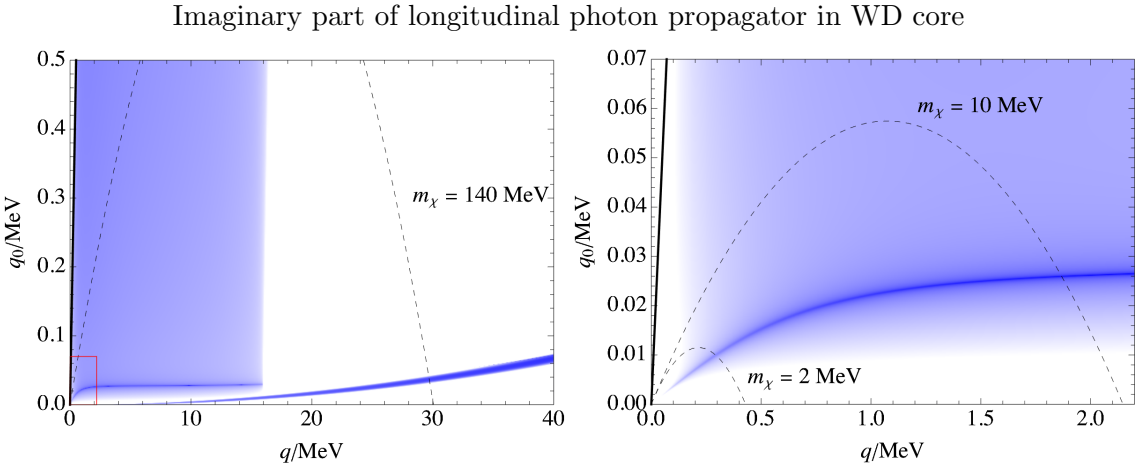

Figure 2. Density plot of the imaginary part of the longitudinal photon propagator $\mathrm{Im}\, D_L(q_0, q)$ for a nominal white dwarf core model (see Section 4.2). Darker shades correspond to larger values of the imaginary part, on a logarithmic scale. In the left-hand panel, the band on the left corresponds to scattering with the relativistic electrons, while the parabolic band corresponds to scattering with (non-relativistic) ions. The electron band is cut off at $q \simeq 2E_F$ by kinematics, where $E_F \simeq 8\,\mathrm{MeV}$ is the electron Fermi energy. The solid black line corresponds to the light cone, while the dashed black line corresponds to the maximum possible value $q_{0,\mathrm{max}}$ of q_0 for given q, for a DM particle of mass $m_\chi = 140\,\mathrm{MeV}$ (travelling at the escape velocity $v_{\mathrm{esc,core}} \simeq 0.1c$). The right panel shows the imaginary part at smaller momentum transfers, corresponding to the red rectangle on the left-hand plot, along with $q_{0,\mathrm{max}}$ curves for $m_\chi = 10$ MeV and 2 MeV. The main feature at these small momenta is the longitudinal phonon dispersion relation.

modes. As we discuss in this Section, scattering from longitudinal phonons (compression waves) can dominate the DM scattering rate at small DM masses.

Firstly, we review the basic theory of longitudinal phonons in a WD core [54]. For small momentum transfers, and phase velocities ($v_{\mathrm{ph}} = q_0/q$) significantly larger than the ion velocities, then as discussed above, we can use the zero-velocity approximation $\Pi_L(Q) \simeq \omega_i^2 Q^2/q_0^2$ for the ion contribution to the photon self-energy. The electron contribution is well-approximated by that for a free, degenerate Fermi gas; at small momentum transfers, this gives $\Pi_L(Q) \simeq -\frac{4\alpha}{\pi} E_F p_F \frac{Q^2}{q^2} \equiv \frac{-Q^2}{q^2} k_{\mathrm{TF}}^2$. So, the inverse longitudinal photon propagator is given by

$$Q^2 - \Pi_L(Q) \simeq Q^2 \left(1 + \frac{k_{\mathrm{TF}}^2}{q^2} - \frac{\omega_i^2}{q_0^2}\right) \tag{4.3}$$

The longitudinal photon propagator has a pole, $Q^2 - \Pi_L \simeq 0$, at

$$q_0^2 = \omega(q)^2 \equiv \frac{\omega_i^2 q^2}{q^2 + k_{\mathrm{TF}}^2} \simeq \begin{cases} \frac{\omega_i^2}{k_{\mathrm{TF}}^2} q^2 & q^2 \ll k_{\mathrm{TF}}^2 \\ \omega_i^2 & q^2 \gg k_{\mathrm{TF}}^2 \end{cases} \tag{4.4}$$

This gives the dispersion relation for longitudinal phonons.[10] The approximation to the electron contribution to Π_L will be valid for $q \lesssim E_F$, while the ion approximation should

[10] As is the case for metals, the acoustic dispersion relation for longitudinal phonons arises because of

be valid at q small compared to lattice scales, i.e. $q \lesssim$ few $\times$ MeV. If there is only a single ion species, then its number density is $n_i = n_e/Z_i = \frac{p_F^3}{3\pi^2 Z_i}$. This gives a sound speed of

$$c_s = \frac{\omega_i}{k_{\rm TF}} = \sqrt{\frac{Z_i}{3}\frac{E_F}{m_i}}v_F \tag{4.5}$$

Taking our nominal WD core parameters, for which $E_F \simeq 8\,\text{MeV}$, $k_{\rm TF} \simeq 0.8\,\text{MeV}$ and $\omega_i \simeq 30\,\text{keV}$, we obtain $c_s \simeq 0.036$. This is illustrated in the right-hand panel of Figure 2, which shows how $\text{Im}\, D_L(Q)$ is maximised on the phonon dispersion relation, for low momentum transfers. The narrow dark-shaded region (the shading is logarithmic in $\text{Im}\, D_L(Q)$) corresponds to a weakly-damped pole.[11]

Since c_s is smaller than the escape velocity in the WD core, $v_{\rm esc} \simeq 0.1$, it is kinematically possible to scatter into phonons for all DM masses. For weakly-damped phonons, the phonon scattering rate is dominated by momenta close to the dispersion relation, and can be calculated analytically. The escape velocity is non-relativistic, so the leading-order scattering rate is

$$\Gamma_L \simeq \frac{1}{2\pi^2}\frac{g_\chi^2}{v_\chi}\int dq dq_0\, q(1+f(q_0))\frac{1}{(q^2+m_X^2)^2}\,\text{Im}\,\Pi_L^X(Q) \tag{4.7}$$

(where we have assumed a vector mediator for simplicity — we discuss scalar mediators in Section 4.7). From Section 2, $\text{Im}\,\Pi_L^X(Q)$ is given by

$$\text{Im}\,\Pi_L^X(Q) = \Pi_i^{XX} + \frac{\Pi_i^{AA}((\Pi_r^{XA})^2-(\Pi_i^{XA})^2) + 2\Pi_r^{XA}\Pi_i^{XA}(Q^2-\Pi_r^{AA})}{(Q^2-\Pi_r^{AA})^2+(\Pi_i^{AA})^2} \tag{4.8}$$

So, if we fix q and integrate over q_0, the resonant contribution is dominated by the $\frac{\Pi_i^{AA}((\Pi_r^{XA})^2-(\Pi_i^{XA})^2)}{(\Pi_r^{AA}-Q^2)^2+(\Pi_i^{AA})^2}$ term for q_0 close to the dispersion relation value $\omega(q)$. If we expand $Q^2-\Pi_r^{AA}$ to linear order around the dispersion relation $q_0=\omega$, writing $Q^2-\Pi_r^{AA} \simeq C(q_0-\omega) \equiv Cy$, then

$$\begin{aligned}\int dq_0\,\text{Im}\,\Pi_L^X(q_0,q)(\dots) &\simeq \int dy \frac{\Pi_i^{AA}((\Pi_r^{XA})^2-(\Pi_i^{XA})^2)}{C^2y^2+(\Pi_i^{AA})^2}(\dots)\\ &\simeq \frac{\pi}{|C|}\left\{(\Pi_r^{XA})^2-(\Pi_i^{XA})^2(\dots)\right\}_{(\omega,q)}\end{aligned} \tag{4.9}$$

From Eq. (4.3), we have that

$$\begin{aligned}\frac{d}{dq_0}(Q^2-\Pi_L) &\simeq \frac{2}{q_0}\left((1+k_{\rm TF}^2)q_0^2-\frac{q^2\omega_i^2}{q_0^2}\right)\\ &= \frac{2(Q^2-\Pi_L)}{Q^2}+\frac{2\omega_i^2Q^2}{q_0^3}\end{aligned} \tag{4.10}$$

screening from the electron gas; an ion lattice in a *fixed* negative charge background would have gapped longitudinal oscillations [57].

[11] At small momentum transfers, the imaginary part of the ion contribution to Π_L will be very small, while the contribution from the electrons is

$$\Pi_L(Q) \simeq k_{\rm TF}^2\left(1+i\frac{\pi}{2}\frac{q_0/q}{v_F}\right) \tag{4.6}$$

so the imaginary part is suppressed relative to the real part by at least $c_s/v_F \sim \sqrt{E_F/m_i}$.

Evaluating this on the dispersion relation, we have $C \simeq 2\omega_i^2 Q^2/\omega^3$. Thus, the resonant scattering rate is

$$\Gamma_{\rm res} \simeq \frac{1}{4\pi}\frac{g_\chi^2}{v_\chi}\int \frac{dq}{q}(1+f(\omega))\frac{\omega^3}{\omega_i^2}\frac{(\Pi_r^{AX})^2-(\Pi_i^{AX})^2}{(q^2+m_X^2)^2} \tag{4.11}$$

The simplest situation in which to evaluate this integral is for m_χ small enough that $q_{\rm max} \simeq 2m_\chi v_{\rm esc} \lesssim k_{\rm TF} \sim$ MeV. In that case, we are scattering off the acoustic (rather than flat) part of the dispersion relation, so $\omega \simeq c_s q \simeq \omega_i q/k_{\rm TF}$. The value of $(\Pi_r^{AX})^2-(\Pi_i^{AX})^2$ on the dispersion relation depends on the mediator's couplings. The contribution to the mixing self-energy from electrons is $\Pi_r^{AX}/Q^2 \simeq -\frac{g_{Xe}}{e}k_{\rm TF}^2/q^2 \simeq -\frac{g_{Xe}}{e}\omega_i^2/\omega^2$ (where g_{Xe} is the mediator coupling to electrons), while the contribution from ions is $\Pi_r^{AX}/Q^2 \simeq \frac{g_{Xp}}{e}\omega_i^2/\omega^2$ (where we have assumed a vector coupling to protons with coupling g_{Xp}). This shows that mediator-electron and mediator-proton couplings give rise to the same resonant scattering rate — this is as we'd expect, since the ions and electrons move together in low-frequency phonons — while the rate for dark photons, for which these contributions cancel, is suppressed. Taking the example of a heavy vector coupling purely to electrons (or to protons), the resonant scattering rate is

$$\Gamma_{\rm res} \simeq \frac{1}{4\pi}\frac{g_\chi^2 g_{eX}^2}{e^2 m_X^4 v_\chi}\omega_i k_{\rm TF}\int dq\, q^2 \simeq \frac{2}{3\pi}\frac{g_\chi^2 g_{eX}^2}{e^2 v_\chi}\omega_i k_{\rm TF}\frac{m_\chi^3(v_\chi-c_s)^3}{m_X^4} \tag{4.12}$$

(ignoring the temperature of the medium), since the maximum q for which we can scatter into an acoustic phonon is $q_{\rm max} = 2m_\chi(v_\chi - c_s)$. This analytic rate is drawn as the black line in Figure 1, showing that it matches up with the scattering rates for electron- and proton-coupled vectors at small m_χ.

For a dark photon mediator, we have $\mathrm{Im}\,\Pi_L^X(Q) = \frac{\kappa^2 Q^4 \Pi_i^{AA}}{(\Pi_r^{AA}-Q^2)^2+(\Pi_i^{AA})^2}$, so the resonant scattering rate is given by

$$\Gamma_{\rm res} \simeq \frac{g_\chi^2\kappa^2}{4\pi}\frac{1}{m_X^4 v_\chi}\int \frac{dq}{q}\frac{\omega^3}{\omega_i^2}q^4 = \frac{32}{7\pi}\frac{g_\chi^2\kappa^2}{v_\chi}\omega_i k_{\rm TF}\frac{m_\chi^4}{k_{\rm TF}^4}\frac{m_\chi^3(v_\chi-c_s)^7}{m_X^4} \tag{4.13}$$

As expected, this is suppressed by higher powers of m_χ and v_χ compared to Eq. (4.12) — at small enough m_χ, this suppression is strong enough that transverse scattering can dominate instead, as we discuss in Section 4.6.

From Figure 1, we can see that the resonant scattering rate from Eq. (4.12) is larger than the naive scattering rate for an electron-coupled vector, but smaller than that for a proton-coupled vector. We can understand this behaviour parametrically. For an electron-coupled vector, the contribution to the imaginary part of the self-energy from the degenerate electron gas is $\mathrm{Im}\,\Pi_L \simeq \frac{g_{eX}^2}{2\pi}E_F^2\frac{q_0}{q}\mathbb{1}_{q_0<qv_F}$, where $\mathbb{1}$ denotes the indicator function. So, assuming that $v_\chi \ll v_F$, the 'no-mixing' scattering rate (i.e. using only the first term in Eq. (2.5)) is

$$\Gamma_{\rm no-mix} \simeq \frac{1}{30\pi^3}\frac{g_\chi^2 g_{eX}^2}{v_\chi}\frac{E_F^2 m_\chi^3 v_\chi^5}{m_X^4} \tag{4.14}$$

Compared to the resonant scattering rate,

$$\frac{\Gamma_{\rm res}}{\Gamma_{\rm no-mix}} \simeq \frac{20\pi^2 k_{\rm TF}\omega_i}{e^2 E_F^2 v_\chi^2}\left(1-\frac{c_s}{v_\chi}\right)^3 = 20\frac{v_F c_s}{v_\chi^2}\left(1-\frac{c_s}{v_\chi}\right)^3 \tag{4.15}$$

If c_s is not too much smaller than v_χ, then this ratio can be reasonably large for high v_F — for our nominal WD core, $\Gamma_{\rm res}/\Gamma_{\rm no-mix} \simeq 20$.

For an ion-coupled vector, the most naive scattering rate we can compute is to use the Yukawa cross-section for scattering with stationary ions;

$$\Gamma_{\rm no-mix} = n_i \sigma_{\chi i} v_\chi \quad , \quad \sigma_{\chi i} \simeq \frac{g_\chi^2 g_{Xp}^2 Z_i^2}{\pi}\frac{\mu_{\chi i}^2}{m_X^4} \tag{4.16}$$

where we have assumed a heavy mediator ($m_X \gg m_\chi v_\chi$), and $\mu_{\chi i} \equiv m_\chi m_i/(m_\chi + m_i)$ is the DM-ion reduced mass. This corresponds to the dotted orange line in Figure 1, which matches the full scattering rate at large m_χ. Compared to the resonant scattering rate at small m_χ,

$$\frac{\Gamma_{\rm res}}{\Gamma_{\rm no-mix}} \simeq \frac{2}{3Z_i^2 e^2}\frac{k_{\rm TF}\omega_i m_\chi^3 (v_\chi - c_s)^3}{n_i \mu_{\chi i}^2 v_\chi^2} \simeq \frac{2}{Z_i}\frac{m_\chi}{E_F}\frac{v_\chi c_s}{v_F^2}\left(1-\frac{c_s}{v_\chi}\right)^3 \tag{4.17}$$

where we have used $\mu_{\chi i} \simeq m_\chi$, since we are interested in the small-m_χ regime. Since $c_s < v_\chi \ll v_F$, the resonant scattering rate is much smaller than the naive rate unless $m_\chi \gg E_F$, as illustrated in Figure 1.

For low-velocity ions, the scattering rate in Eq. (4.16) is a good approximation to the no-mixing scattering rate obtained from modelling the ions as a free gas (since, as per Eq. (4.14), the no-mixing scattering rate from electrons is much smaller). Furthermore, since the imaginary part of the ion contribution to Π_L is unimportant for the resonant scattering rate into phonons, and the real part of the ion contribution is very similar for a free gas or a zero-velocity model (at the momentum transfers of interest), the resonant rate $\Gamma_{\rm res}$ computed above is very close to the full scattering rate for the free ion gas model. Consequently, the small $\Gamma_{\rm res}/\Gamma_{\rm no-mix}$ ratio in Eq. (4.17) corresponds to a strong cancellation between the Π_i^{XX} and mixing terms in Eq. (2.5).

This cancellation arises because of the kinematics of scattering with low-velocity ions. To scatter off a stationary ion, we need $q_0 = q^2/(2m_i)$, so $q_0/q = q/(2m_i) \leq m_\chi v_\chi/m_i$. For small m_χ, this phase velocity is $\ll c_s$. Consequently, the ion contribution to Π_L, which is $\propto 1/q_0^2$, is much larger than the electron contribution. Since the Π_i^{XX} term is also dominated by the ion contribution (for a free ion gas model), we obtain a cancellation between this term and the mixing term in Eq. (2.5), similarly to a dark photon mediator. Both this example, and the electron-coupled vector example above, illustrate that even for mediators other than dark photons, collective effects can give rise to parametrically large differences between the full and naive calculations (and that these can be either enhancements or suppressions).

4.4 Transverse mediator modes

The above calculations all applied to scattering via the vector mediator's longitudinal mode. For mediators other than dark photons, the scattering rate via transverse modes is orders

of magnitude smaller, over the entire m_χ range in Figure 1. For an electron-coupled vector, the transverse rate is suppressed by v_χ^2 from the form of Γ_T (Eq. (A.6)), and in addition, is not enhanced by resonant scattering with phonons (the transverse phonons — shear waves — arise from the ion lattice, rather than through the lattice's interactions with the electron gas, and couple more weakly to an electron-coupled mediator, since they do not involve long-wavelength charge density perturbations). For an ion-coupled vector, in addition to the v_χ^2 suppression, the imaginary parts of $\mathrm{Im}\,\Pi_T^{XX}$ and Π_T^{AX} are suppressed by the small ion velocities; e.g. from Appendix B.4, if we approximate the ions by a free, non-relativistic gas, then the ion contribution to vector self-energies is

$$\Pi_T = \omega_p^2 - \left(\sigma_i^2 - \frac{Q^2}{4m_i^2}\right)\Pi_L \tag{4.18}$$

where $\sigma_i = \sqrt{T/m_i} \sim 3 \times 10^{-5}$ is the typical ion velocity. The only situation in which scattering via transverse modes contributes significantly to the rate is with a dark photon mediator, for which the longitudinal modes are screened most strongly. In contrast, there is no static screening for transverse modes (i.e. $\Pi_T(q_0, q) \to 0$ as $q_0 \to 0$ — see Appendix D), and Π_T is mostly imaginary in relevant parts of the small-Q phase space (Eq. (B.13) and (B.14)), so the transverse rate can compete with the longitudinal one at small enough momentum transfer. At the smallest m_χ shown in Figure 1, the dark photon rate begins to be dominated by the transverse rate; we will discuss this kind of behaviour in more detail (for a light dark photon mediator) in Section 4.6.

4.5 Heavy dark photon mediator

Using the calculations outlined above, we can compare the potential reach of DM scattering signatures in WDs to other constraints on DM parameter space. This comparison will depend on the DM model. Here, we will consider the illustrative example of a 'heavy' dark photon mediator; specifically, $m_X \sim 2m_\chi$. This is heavy enough that the mediator mass is significantly larger than scattering momentum transfers, but light enough that cross-sections are not suppressed by a parametrically higher scale.

Figure 3 shows the constraints on this model, in terms of the standard σ_e parameter used in the direct detection literature,

$$\sigma_e \equiv \frac{g_\chi^2 g_e^2}{\pi} \frac{\mu_{\chi e}^2}{((\alpha m_e)^2 + m_X^2)^2} \tag{4.19}$$

(this roughly corresponds to the DM-electron cross section appropriate for direct detection experiments relying on electron excitations). The green shaded regions correspond to constraints from existing direct detection experiments [59–65], while the dashed green curves corresponds to sensitivity projections for future direct detection experiments (specifically, SENSEI [66–68] and SuperCDMS [69]).

To place firm constraints on DM models from WD observations, we would need to observe old, sufficiently cold white dwarfs in a location where we can be confident the DM density is high. So far, it is not possible to be certain that these criteria are met. However,

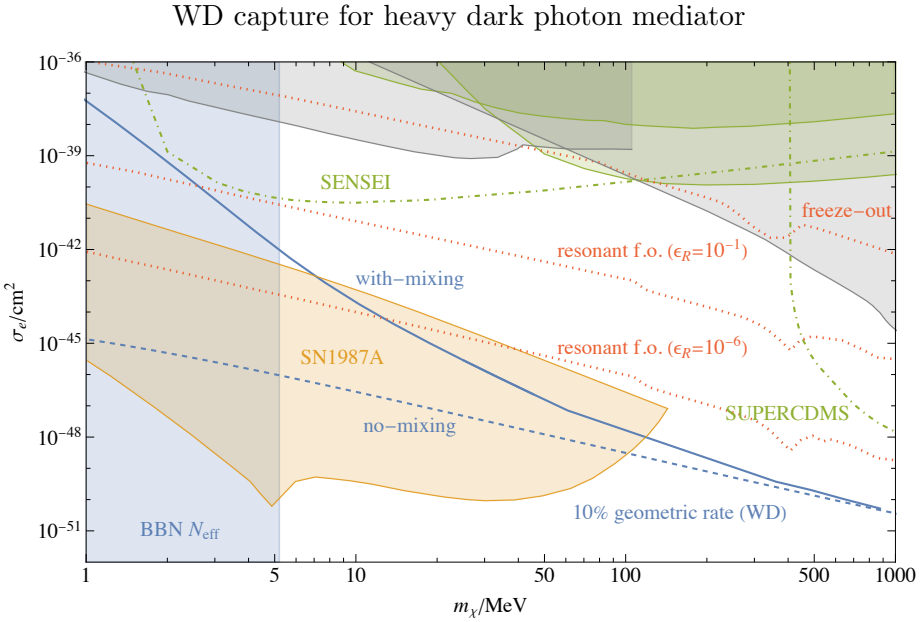

Figure 3. Plot of constraints on a scalar DM particle coupled via a heavy dark photon mediator, taking the mediator to have mass $m_X \sim 2m_\chi$, with coupling $\alpha_\chi \equiv \frac{g_\chi^2}{4\pi} = 0.005$ to the DM χ. The blue curve shows the coupling required to obtain 10% of the geometric capture rate for our nominal WD model from Section 4; this corresponds to the approximate capture rate required for observable heating from DM annihilations, under the assumptions in [46]. The dashed blue curve shows the same calculation ignoring mixing effects. The other curves correspond to existing constraints on the DM model — see Section 4.5 for details.

[46] argues that, from observations of WDs in the M4 globular cluster, one can set plausible constraints on the DM scattering rate for models in which in the DM would subsequently annihilate in the WD, assuming that the ambient DM density in the globular cluster is $\mathcal{O}(10^3\,\mathrm{GeV\,cm^{-3}})$. To be in tension with observations, the capture rate for such DM in heavy WDs would need to be $\gtrsim 10\%$ of the geometric capture rate [46]. We indicate the coupling values needed to attain this capture rate, for the nominal WD model introduced above, via the solid blue curve in Figure 3.

To calculate the DM capture rate in our nominal WD, we take the DM halo velocity dispersion to be $\sigma = 8\,\mathrm{km\,s^{-1}}$, and the velocity of the WD relative to the halo to be $v_\star = 20\,\mathrm{km\,s^{-1}}$, as in [46]. We approximate the capture rate over the whole star by taking the per-volume capture rate in the core, and multiplying it by the WD volume. Since the core comprises the majority of the WD's volume, and has a higher per-volume DM capture rate than the less dense outer layers, this should be a good approximation. It would obviously be possible to do a more proper calculation, but the large uncertainties in parameters such as the halo DM density in the globular cluster mean that other unknowns dominate the uncertainty in the calculation; we leave a more careful treatment to future work. As mentioned above, the main goal of our paper is to illustrate the physics of collective effects. To this end, we can compare our full calculation to a calculation ignoring

mixing effects, shown as the dashed blue curve in Figure 3. This illustrates how, for DM masses $\lesssim \mathcal{O}(100\,\mathrm{MeV})$, collective effects suppress the scattering rate via a heavy dark photon mediator by orders of magnitude.

The WD and direct detection signatures apply to a particle that makes up 100% of the DM abundance. While, for a DM particle making up a fraction f of the local DM abundance, direct detection experiments are sensitive to couplings $f^{-1/2}$ larger, WD heating signatures are unobservable for sufficiently small f (for [46], $f \lesssim 0.1$), due to the geometric capture rate ceiling. Consequently, it is valuable to understand the parameter space for which a candidate particle can make up 100% of the DM abundance.

The simplest way to produce the correct DM abundance is via thermal freeze-out, i.e. for the DM to be in chemical equilibrium with the SM until $T \sim 0.1 m_\chi$, after which point the exponentially Boltzmann-suppresssed χ abundance means that χ-χ annihilations fall out of equilibrium. Since freeze-out relies on χ-χ annihilations being fast enough, it implies a related χ-χ annihilation rate in the late universe, which could be detected through cosmic rays or its effects on the CMB. These constraints rule out standard freeze-out scenarios for fermionic DM coupled to a vector mediator, in which the annihilation rate is dominated by a DM-velocity-independent component [70]. For scalar DM, on the other hand, the annihilation rate scales $\sim v_\chi^2$ since s-wave annihilation is forbidden by angular momentum conservation [70]. Since the DM velocity is high during freeze-out, $v_\chi \sim 0.1$, and much lower in the late universe, scalar DM annihilating through a dark photon mediator can attain the correct freeze-out abundance at couplings for which late-universe annihilation signatures are not constraining [70]. Consequently, for Figure 3, we have assumed a scalar DM particle (though this does not make a large difference to the WD calculations).

The upper red-dotted line in Figure 3 corresponds to the couplings required for the correct freeze-out abundance, when m_X is $\mathcal{O}(1)$ different from $2m_\chi$ (e.g. $m_X = 3m_\chi$). As the figure shows, these couplings are large enough to be almost excluded by existing experiments. To obtain the correct DM freeze-out abundance at smaller couplings, we need to increase the annihilation rate around freeze-out. The simplest way to do this is to make the process resonant, which occurs when $m_X \simeq 2m_\chi$ (so that annihilation via an s-channel mediator is almost on-shell). The lower red-dotted lines in Figure 3 correspond to different resonant scenarios, with $\epsilon_R \equiv \frac{m_X^2}{4m_\chi^2} - 1$ quantifying how close to resonance a zero-velocity annihilation is. These curves illustrate that, by tuning the parameters, we can obtain the correct DM abundance for a wide range of couplings below current bounds.[12]

Another constraint on DM freeze-out scenarios, for sufficiently light DM, is the effect of extra relativistic particles at $\sim$ MeV temperatures on BBN [71]. This rules out thermal freeze-out DM for $m_\chi \lesssim 5.2\,\mathrm{MeV}$ [71] (for scalar DM), as illustrated by the blue shaded region in Figure 3.

At higher DM masses, the only astrophysical systems with sufficiently high temperatures to produce χ particles in large numbers are supernovae. In particular, χ and X

[12]For scalar DM, $\epsilon_R \lesssim 10^{-6}$ results in the dark photon dominantly decaying into SM states, since the decay into DM particles is phase space suppressed [70], changing the phenomenology. This can be avoided in other models, which can allow even smaller σ_e [70].

production in SN1987A would have modified the observed neutrino signal, placing constraints on their couplings [72]. Since X production can also be significant (for m_X not too large), the SN1987A constraints will depend on g_χ and κ separately, rather than just on their product. In Figure 3, we show the constraints calculated in [72] for fermionic DM, coupled to a dark photon with mass $m_X = 3m_\chi$, with $\alpha_\chi \equiv \frac{g_\chi^2}{4\pi} = 0.005$ (this coupling is chosen so that DM self-interactions are weak enough to be unconstrained [73]). Though scalar DM with a slightly different dark photon mass will behave somewhat differently inside the SN, the overall constraints should be similar [72].

As well as being produced in supernovae, χ and X particles could also be produced in accelerator experiments. Figure 3 show the constraints from LSND [74], E137 [75] and BaBar [76] as gray shaded regions. At DM masses $\gtrsim 40\,\mathrm{MeV}$, where self-interaction constraints are weaker, the accelerator constraints can be relaxed by taking larger α_χ (since production is mostly via on-shell X, which scales as κ^2 rather than $\kappa^2\alpha_\chi$).

Putting all of these constraints and projections together, Figure 3 illustrates how DM scattering in WDs could potentiallly probe much weaker couplings than even next-generation direct detection experiments. It also illustrates how, for DM masses $\lesssim \mathcal{O}(100\,\mathrm{MeV})$, collective effects suppress the capture rate by orders of magnitude relative to a naive calculation. While the difference between the mixing and no-mixing curves happens to be mostly within the SN1987A-disfavoured region for this model, it is still important to have done the calculation correctly, both to confirm that the rate is not even further suppressed, and since the SN1987A constraints are subject to some uncertainties [77]. For other dark matter models, the relationship between WD signatures and existing constraints will differ; the main point of Figure 3 is to provide a worked example of how these might fit together.

A possible caveat to our capture rate calculations is self-capture; if the DM-mediator coupling g_χ is much larger than the mediator-SM couplings κe, then even if only a small amount of DM is captured via SM interactions, it may come to dominate the capture rate, and allow this to increase past the SM-only value. For asymmetric DM models, in which DM does not annihilate, but simply builds up in the WD, self-capture could be important — we leave investigations of DM models and signatures in this regime to future work. For symmetric DM, as we have been considering for WD heating signatures, the fairly short timescale on which DM annihilates within the star means that, according to basic estimates, self-capture should not be significant for the mass range in Figure 3 (above the BBN bound). We leave a more detailed treatment to future work.

4.6 Light dark photon mediator

The comparison between WD scattering signatures and other constraints is somewhat different for a very light mediator, as low-momentum-transfer scatterings are enhanced. In this Section, we will focus on the case of an ultra-light dark photon mediator; for other types of light mediators, there are typically strong constraints on the mediator-SM couplings, arising from high-energy experiments [78], stellar production [36], or fifth force tests [79].

Collisions in a WD occur at significantly higher relative velocities ($\sim 0.1c$) than typical halo DM velocities ($\lesssim 10^{-3}c$), so we expect the WD scattering rate to be relatively

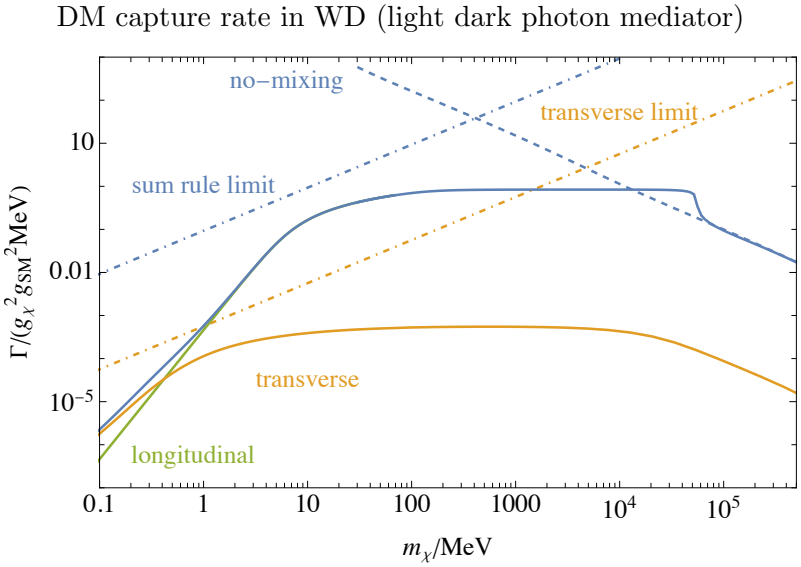

Figure 4. Rates for down-scattering to a gravitationally-bound orbit in the core of a heavy WD, for a DM particle with $v_\infty = 10^{-3}$, coupling through a light dark photon mediator. The dashed blue curve corresponds to the rate calculated ignoring collective effects, while the solid blue curve incorporates collective effects, which become significant for $m_\chi \lesssim$ few $\times\, 10^4\,$MeV (corresponding to the bump in the solid blue curve). The dot-dashed blue curve corresponds to the EM sum rule limit for the scattering rate (Section 2.1), while the dot-dashed orange curve corresponds to the sum rule limit for scattering through transverse dark photon exchange. The orange curve shows the contribution of scattering through transverse dark photon exchange — this is relatively suppressed at higher DM masses, but dominates at lower DM masses, due to the lack of screening at small momenta for transverse excitations.

enhanced for heavy mediators, but not for light mediators. Consequently, we expect that WD scattering signatures for light mediators should be less competitive with other probes, such as direct detection experiments, than in the heavy mediator case.

To illustrate the physics of scattering via a light dark photon mediator (or equivalently, for millicharged DM — see e.g. Appendix D of [73]), Figure 4 shows the capture rate for DM with a particular v_∞ $(= 10^{-3})$, comparing the full calculation to a naive particle-by-particle one (we show the results for spin-1/2 DM, but those for spin-0 DM are very similar). For the naive calculation, the capture rate increases as we decrease m_χ, since smaller momentum transfers are required to lose enough energy for capture. Specifically, for capture to a bound orbit, we need $q_0 > \frac{1}{2} m_\chi v_\infty^2$ (taking velocities to be non-relativistic). For Yukawa scattering off stationary ions, we have $q_0 = \frac{\mu_{\chi i}^2 v_\chi^2}{m_i}(1 - \cos\theta)$, where θ is the scattering angle in the CoM frame, so we need $(1 - \cos\theta) > \frac{m_i m_\chi}{2\mu^2}\frac{v_\infty^2}{v_\chi^2} \equiv \epsilon$ for capture. So, the total cross section for sufficiently hard scatterings is

$$\sigma = \frac{1}{8\pi}\frac{g_\chi^2 \kappa^2 e^2}{\mu^2 v_\chi^4}\left(\frac{1}{\epsilon} - \frac{1}{2-\epsilon}\right) \overset{\epsilon \ll 1}{\simeq} \frac{g_\chi^2 \kappa^2 e^2}{4\pi}\frac{1}{m_i m_\chi}\frac{1}{v_\chi^2 v_\infty^2} \tag{4.20}$$

showing that the small-momentum-transfer enhancement more than compensates for the

smaller $\mu_{\chi i}$ as m_χ is decreased, leading to a $\sigma \propto 1/m_\chi$ dependence, as per the dashed blue line in Figure 4. Recalling that the total capture rate, from Eq. 3.4, behaves as

$$\frac{dC}{dV} \propto \int_0^\infty dv_\infty v_\infty f(v_\infty) \Gamma_{v_\infty} \tag{4.21}$$

we see that attempting to calculate the total capture rate, integrating over all v_∞ using the no-mixing rates, would result in a $\int \frac{dv_\infty}{v_\infty}$ logarithmic divergence driven by small v_∞ [80]. This is why we displayed the capture rate for a *fixed* v_∞ in Figure 4; to obtain a finite total capture rate, we always need to take into account mixing effects in some way, and there is no sensible comparison to a fully naive calculation.

From Figure 4, we can see that once the momentum transfer required for capture is smaller than the screening scale in the WD (i.e. $m_\chi v_\infty^2 / v_{\rm esc} \lesssim$ MeV, rather roughly), the small-momentum enhancement is cut off by screening effects.[13] This results in a roughly constant scattering rate as m_χ is decreased (since the rate is dominated by momentum transfers around the screening scale), until m_χ becomes small enough that all of the accessible momentum transfer range is below the screening scale, after which the scattering rate decreases with m_χ. For small enough m_χ, the weaker screening of transverse modes is enough to make up for the extra v_χ^2 suppression, and transverse scattering starts to dominate the capture rate, as illustrated in Figure 4.[14] The figure also displays the EM sum rules limits from Section 2.1, illustrating how the calculated rate gets within a factor few of this limit, for m_χ such that the typical momentum transfer approximately matches the appropriate screening scale in the WD.

Using the formulae from Section 3, we can compute the total capture rate, integrated over the v_∞ distribution. Figure 5 illustrates the results, showing the coupling required to obtain 10% of the geometric capture rate (as per the WD heating discussion in Section 4.5), using the same assumptions and approximations as described in the previous section[15] (we

[13] Even though Figure 4 shows DM masses up to $m_\chi \gg$ GeV, capture is dominated by low-momentum-transfer scatterings, so nuclear form factors are not important (they only become important for $m_\chi \gtrsim$ 100 TeV).

[14] As discussed in Section 4.2, a proper treatment of the ion lattice is somewhat complicated, and this is even more true for its transverse mode response. Transverse phonons (shear waves) can be supported by the lattice, even without dynamical electrons, so we cannot determine the transverse phonon properties via calculations like those in Section 4.3. However, at the relevant momentum transfer scales, the total transverse response function will be dominated by the electron response, and different models for the ion response will make little difference. For example, we compared two different toy models for the ion contribution to the transverse response; treating ions as a free gas (Appendix B.4), and taking a single-pole response function for transverse phonons, assuming the shear wave velocity is $\sim \sqrt{2}$ of the compression wave velocity [37], with quality factor $Q = 100$. For the m_χ range shown in Figure 4, these models result in almost the same behaviour.

[15] While the dependence of the per-volume DM scattering rate on medium density is weaker for a light dark photon mediator than for a heavy mediator, it still generally increases with density (as per the limits in Section 2.1). This is in contrast to the case of dark photon *production*, where the per-volume production rate of very light dark photons is larger in less dense media [81, 82] — intuitively, the sterile mode decouples from SM particles as $m_{A'} \to 0$, so its production rate vanishes, but DM-SM scattering is mediated by the active mode. Since the per-volume scattering rate in the denser core is larger than in the less dense outer layers of the WD, the approximation of only using the scattering rate in the core should be good.

display the results for fermionic DM — the rates for scalar DM are very similar). The coupling is shown in terms of the 'effective millicharge' $q_{\rm eff} \equiv \kappa g_\chi / e$. The gray shaded regions correspond to existing constraints; at $m_\chi \lesssim 10\,\mathrm{MeV}$, these arise from production in SN1987A [72] or in stellar cores [83], while at higher masses, they come from direct detection experiments [84, 85]. Figure 5 illustrates that, over the whole m_χ range, the couplings required for close-to-geometric capture rates in WDs lie within already-excluded parameter space. The EM sum rule bound, indicated by the dashed line, shows that this statement is almost independent of our model of the WD interior; for DM masses $\lesssim$ GeV, any causal model of the WD medium would result in significantly-below-geometric capture rates, for unconstrained couplings (modulo the anti-screening issues discussed in Appendix D).

One possible caveat to this statement is self-capture. For millicharged DM (or somewhat equivalently, for a very light dark photon mediator with $\kappa \sim \mathcal{O}(1)$), self-capture is not enhanced. If $\kappa \ll 1$, then g_χ can be much larger (for a given $q_{\rm eff}$), and it might be possible for self-scatterings to become important. However, it is worth noting that light mediators somewhat complicate the possible signatures of DM scattering in WDs — in particular, if DM annihilates to a light mediator, this generally escapes from the WD, so does not deposit its energy. Millicharged DM, which interacts with the SM photon, would lead to energy depositions from annihilations, but could only make up a small sub-component of the DM density (at the relevant couplings), since long-range interactions with SM matter would alter the galactic dynamics of DM halos [86–92]. In fact, as demonstrated in recent work [92], it is likely that dark photon models are also constrained by galactic dynamics, and are only viable as DM subcomponents at these couplings.

Overall, there are a number of points worth emphasizing. For scattering via a light mediator, collective effects are important even for large DM masses, since the naive calculation for the capture rate is dominated by soft scatterings. However, since soft scatterings are enhanced, we obtain less benefit from the high velocity of collisions in a WD, so obtaining close-to-geometric capture rates requires couplings above those allowed by other constraints. In addition, it can be more complicated to obtain observable signatures, such as WD heating, from light mediator models.

4.7 Scalar mediator

So far, we have been considering vector mediators, with couplings of the form $X_\mu \bar{f} \gamma^\mu f$. Our formalism can also be applied to other types of mediators, such as scalars. In Figure 6, we show the scattering rates via different kinds of heavy scalar mediators (with couplings of the form $\phi \bar{f} f$) in our nominal WD core.

For a scalar coupling to electrons, $\mathcal{L} \supset \phi \bar{e} e$, Figure 6 shows that the scattering rate is the same as an electron-coupled vector for large m_χ, but significantly smaller for small m_χ. This is because, at large momentum transfers, the relevant scale for both the vector-vector (Π_L) and scalar-scalar ($\Pi^{\phi\phi}$) self-energies is Q^2, whereas at small momentum transfer, the scale for $\Pi^{\phi\phi}$ is m_e^2, whereas the scale for Π_L is $\sim E_F^2$ (for relativistic electrons). Consequently, the scalar rate is suppressed by $\sim 1/\gamma_F^2$. We see this same parametric difference between the no-mixing rates (shown as dashed lines), and the full rates, which

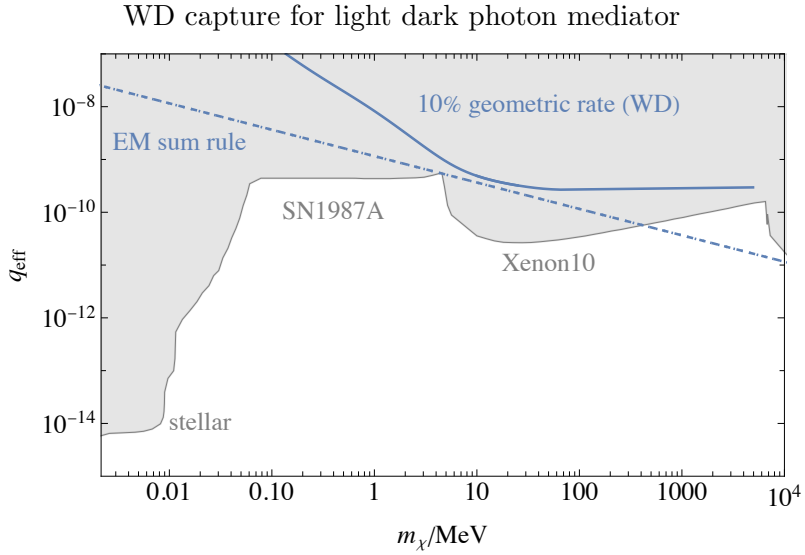

Figure 5. Bounds on the effective millicharge $q_{\rm eff}$ for a DM particle coupling through an ultra-light dark photon mediator (or via the SM photon). The gray shaded region corresponds to existing constraints from stellar cooling [83], SN1987A [72], and the Xenon10 experiment [84, 85]. The blue solid curve corresponds to the approximate $q_{\rm eff}$ required to obtain 10% of the geometric capture rate for the heavy WD model in Section 4.2. This corresponds to the approximate capture rate that could be constrained by DM capture and then annihilation, for WDs in the M4 globular cluster, according to [46]. The dashed line corresponds to the EM sum rule limit for this capture rate.

are dominated by resonant scattering off longitudinal phonons, since the mixing self-energy $\Pi^{\phi L} \sim m_e E_F$ is also suppressed compared to $\Pi^{XL} \sim E_F^2$.

Figure 6 also shows the scattering rate for a scalar with opposite couplings to electrons and protons, $\mathcal{L} \supset \phi(\bar{e}e - \bar{p}p)$. The scattering rate is almost exactly the same as the proton-coupled vector in Figure 1; this is because the ions in the WD core are non-relativistic, whereas the electrons are relativistic, so the scalar coupling to electrons is relatively suppressed, but not the coupling to ions. This illustrates how, even though an $e - p$ scalar mediator — which for non-relativistic SM matter, couples in the same way as a dark photon — can somewhat suppress scattering rates in e.g. direct detection experiments [32, 35], this suppression is easily lifted by relativistic effects.

5 Neutron stars

Many of the possible observational signatures of DM scatterings in WDs also apply to DM scattering in neutron stars (NSs), including black hole formation [13–21, 23] and stellar heating [1–12]. A benefit of the increased density of NSs is that the much higher escape velocity (up to $\sim 0.9c$ in a NS core) means that the kinetic energy of infalling DM is comparable to its rest mass energy, so purely kinetic heating from DM scattering events could potentially result in observable heating (if an old, cold neutron star is observed in a region of sufficiently large DM density) [8, 93].

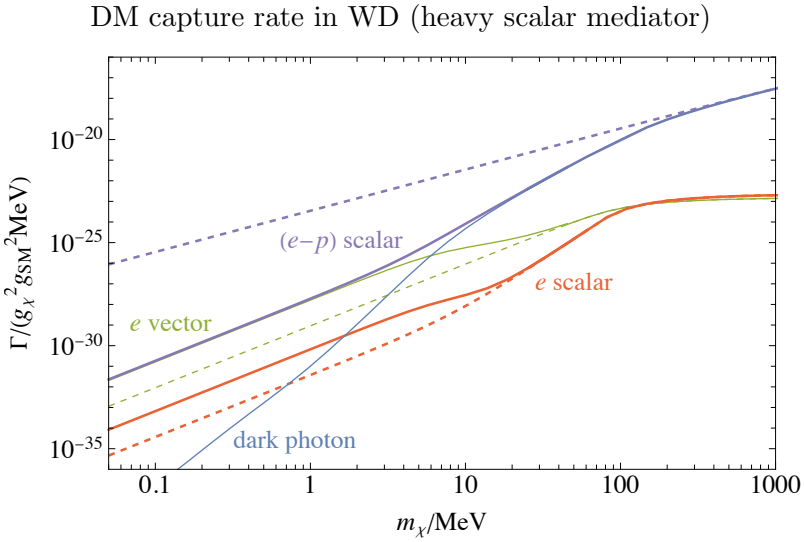

Figure 6. Rates for down-scattering to a gravitationally-bound orbit in the core of a heavy WD for a DM particle with $v_\infty = 10^{-3}$ coupling through a TeV-mass mediator of different types. The dashed curves show rates calculated ignoring collective effects, while the solid curves include collective effects. The red curves correspond to a scalar mediator coupling to electrons. These can be compared to the rate for a electron-coupled vector mediator with the same mass (thin green curves). The purple curves show the rate for a scalar mediator coupling with opposite strengths to electrons and protons. The thin blue curve shows the rate for a heavy dark photon mediator; comparing to the $e - p$ scalar mediator, we see that the suppression at small DM masses is much less for the scalar mediator than for a dark photon mediator.

The major issue for predicting the results of DM scatterings in NSs is our poor understanding of the physics of NS interiors. The 'crust' of a NS — effectively, the region in which the physics is somewhat understood — extends to a depth of $\sim 1\,\mathrm{km}$ (compared to a total radius $\sim 10\,\mathrm{km}$ for the star). Its outer layers consist of an ionic lattice embedded within a degenerate electron gas; as the depth and density increase, this transitions to a complicated 'nuclear pasta' structure of nucleons [8].[16] At smaller radii (the 'core'), where the densities are higher, a range of possible behaviours have been proposed, including various types of meson condensates, or unconfined quark matter [94, 95]. In the latter case, it is even possible that the QCD matter is neutral by itself, forbidding the presence of an electron gas [95, 96]. Consequently, the behaviour of the lepton and QCD sectors in the NS core, which makes up the vast majority of the star's mass and volume, are very uncertain.

Given these uncertainties, one can either attempt to place bounds on DM scattering rates, e.g. by considering scattering only within the NS crust [8], or one can consider toy models of the NS core. Here, we adopt the latter approach; we will consider a very simple toy model, in which the electrons, muons and protons are all represented by free, degenerate Fermi gases, while QCD dynamics are ignored. We emphasize that, given this

[16] [8] considers some collective effects for DM scattering in NS crust, e.g. scattering off phonons, but does not seem to perform a systematic calculation including screening effects.

unrealistic toy model, the following calculations should not be used to place constraints or make precise predictions — their main point is to illustrate how mixing effects are likely to have a significant impact on scattering and capture rates. As well as this toy model, we can calculate the EM sum rule bounds for a dark photon mediator, which will be valid for any physical model of the NS interior (modulo the anti-screening issues discussed in Appendix D).

For our nominal NS parameters, we will take the heaviest NS model from [41], which has

$$M_* \simeq 2.2 M_\odot \quad R_* \simeq 12\,\mathrm{km} \quad v_{\mathrm{esc,core}} \simeq 0.91$$
$$\rho_{\mathrm{core}} \simeq 1.4 \times 10^{15}\,\mathrm{g\,cm^{-3}} \quad \mu_{e,\mathrm{core}} \simeq \mu_{\mu,\mathrm{core}} \simeq 300\,\mathrm{MeV} \tag{5.1}$$

The muon and electron chemical potential determine the proton number density, which corresponds to a proton chemical potential of $\sim 70\,\mathrm{MeV}$ (i.e. $\mu_p \simeq m_p + 70\,\mathrm{MeV}$). We will approximate the photon self-energy as the combination of the free, degenerate Fermi gas contributions from these three species (see Appendix B.3). Neutrons, while uncharged, do interact with photons via their magnetic moments [97], but rough estimates indicate that this contribution will be subdominant. The more worrying omission is that protons (if they are even a sensible degree of freedom in the NS core) strongly interact with themselves, and with the rest of the strongly-interacting QCD matter in the core. We leave a more careful treatment of such effects to future work.

Neutron stars are born at high temperatures in supernovae, but cool down over time; if heating is insignificant, old and isolated NSs are expected to reach temperatures $\sim \mathcal{O}(100\,\mathrm{K})$ [8, 93]. For kinetic heating via DM scattering to be visible with projected instruments, it would need to maintain a NS at a temperature $\gtrsim 10^3\,\mathrm{K}$ [2]. In either case, the temperatures of old NSs will generally be negligible for the purposes of our scattering calculations. These low temperatures, and the very high escape velocity, mean that DM evaporation will only be significant at very low DM masses [58, 98].

Figure 7 takes the same heavy dark photon mediator model that we considered in Section 4.5, and shows the approximate couplings for which one would obtain $\sim$ geometric DM capture rates in our nominal NS, for our toy model. For reasonable DM densities, one generally needs close-to-geometric DM capture rates for signatures such as kinetic heating to be potentially observable [2] (the DM capture rate required for other signatures such as BH formation is more model-dependent). We calculate the capture rate assuming a DM velocity distribution similar to the Milky Way halo, with velocity dispersion $v_0 \simeq 160\,\mathrm{km\,s^{-1}}$ and velocity offset $v_\star \simeq 240\,\mathrm{km\,s^{-1}}$ [99] (in the notation of Appendix E). Figure 7 shows that, for $m_\chi \lesssim 100\,\mathrm{MeV}$, collective effects start to make a significant difference to the capture rate, even for a heavy mediator; for $m_\chi \lesssim 20\,\mathrm{MeV}$, the EM sum rule bounds show that almost any NS interior physics leads to scattering rates below the naive particle-by-particle value, for a heavy dark photon mediator. Since the SN1987A constraints are subject to considerable systematic uncertainties [77], these rates are important to compute correctly, even within the nominally disfavoured parameter space.

Figure 8 shows the parameter space for an ultra-light dark photon mediator (or millicharged DM), as per Section 4.6. Since the NS escape velocity is even higher than for

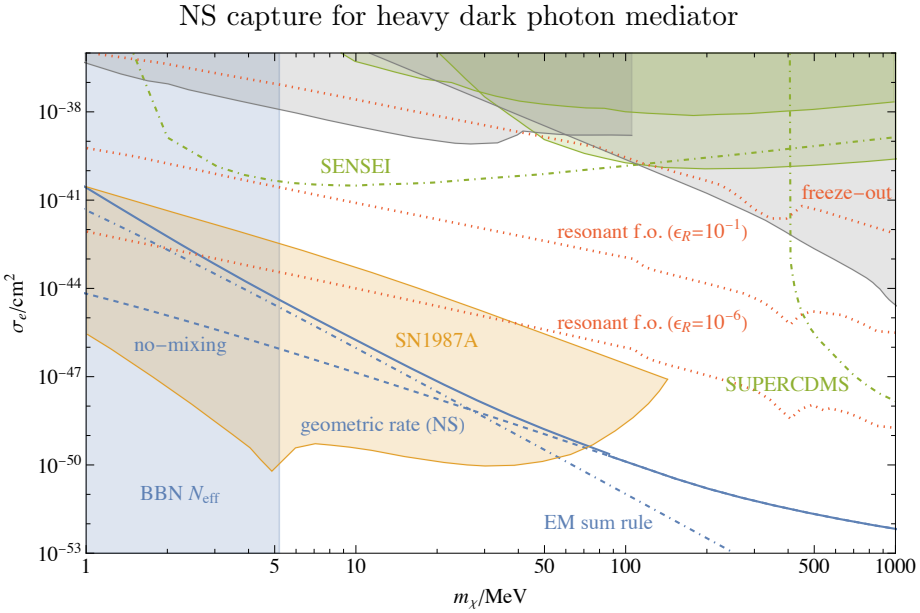

Figure 7. Plot of constraints on a scalar DM particle coupled via a heavy dark photon mediator, taking the mediator to have mass $m_X \sim 2m_\chi$, with coupling $\alpha_\chi \equiv \frac{g_\chi^2}{4\pi} = 0.005$ to the DM χ. The solid blue curve corresponds to the approximate coupling required to obtain of order the geometric capture rate for DM in the toy NS model described in Section 5. The dot-dashed blue curve corresponds to the EM sum rule limit for the capture rate (Section 2.1). The dashed blue curve corresponds to the capture rate computed ignoring mixing effects. The other curves and shaded areas are as per Figure 3.

a WD, we expect constraints involving lower DM velocities (such as direction detection experiments) to be comparatively even better relative to NS scattering, for an ultralight mediator. Correspondingly, our toy model gives a capture rate that is always well below geometric, for couplings in unconstrained parameter space, while the EM sum rule limit is sub-geometric for $m_\chi \lesssim 10\,\mathrm{GeV}$.

6 Dilute stellar plasmas

As well as the compact remnants discussed in previous sections, DM scattering in other types of stars could also lead to observable signatures. In this Section, we will give a brief overview of such signatures, and then sketch how collective effects can modify DM behaviour, for a number of illustrative cases involving our Sun.

The dilute, non-relativistic, weakly-coupled plasma that makes up stars such as the Sun is rather simpler than the dense media in WDs and NSs. However, the relatively high temperature inside the Sun ($T \sim$ keV in the core) means that upscattering needs to be taken into account. For light enough DM (not too much heavier than m_e), the fact that the electron velocity in the Solar core is much larger than the escape velocity ($v_{\rm th} \sim \sqrt{3T/m_e} \simeq 2 \times 10^4\,\mathrm{km\,s^{-1}} \gg v_{\rm esc,core} \simeq 10^3\,\mathrm{km\,s^{-1}}$) means that scattering of halo

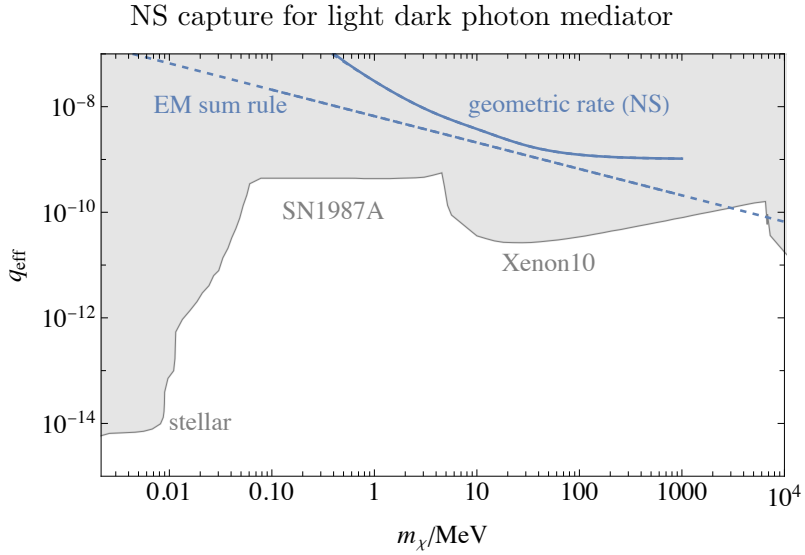

Figure 8. Bounds on the effective millicharge $q_{\rm eff}$ for a DM particle coupling through an ultra-light dark photon mediator (or via the SM photon). The gray shaded region corresponds to existing constraints from stellar cooling [83], SN1987A [72], and the Xenon10 experiment [84, 85]. The blue solid curve corresponds to the approximate $q_{\rm eff}$ required to obtain of order the geometric capture rate for the heavy NS model in Section 5. This corresponds to the approximate capture rate that could be constrained by kinetic heating signatures [2]. The dashed line corresponds to the EM sum rule limit for this capture rate.

DM can result in a higher-energy population of reflected DM, if the optical depth of the Sun is small enough [100]. The flux of this reflected component at Earth will be smaller than the halo DM flux, but its higher energy means that it can be a useful signal in direct detection experiments [100, 101].

For heavier DM, the Solar core temperature means that if $m_\chi \lesssim$ few $\times$ GeV, evaporation of previously-captured DM (i.e. up-scattering to an unbound orbit) is not Boltzmann-suppressed enough to be ignorable [58, 102]. Consequently, it is not possible for a large population of captured DM to be built up, though the evaporating flux, which includes some particles at very high velocities, may be useful target for direct detection experiments [102].

At yet higher DM masses, scattering of halo DM can lead to a captured population, which thermalizes down to a smaller volume within the Sun. If annihilation events occur, but the products are absorbed and thermalize within the Sun, not enough energy is deposited to have an observable effect on the Sun (even if DM is captured at the maximum possible geometric rate). However, if the annihilation products escape, such as neutrinos or long-lived hidden sector particles, then these could give signatures in detectors on Earth [103–111]. For DM heavy enough for this scenario to be of interest, collective effects are only likely to be important for the capture rate if scattering is via a light mediator.

If the dark matter is asymmetric, or otherwise unable to efficiently annihilate, then other types of observational signatures are possible. The simplest of these is anomalous heat

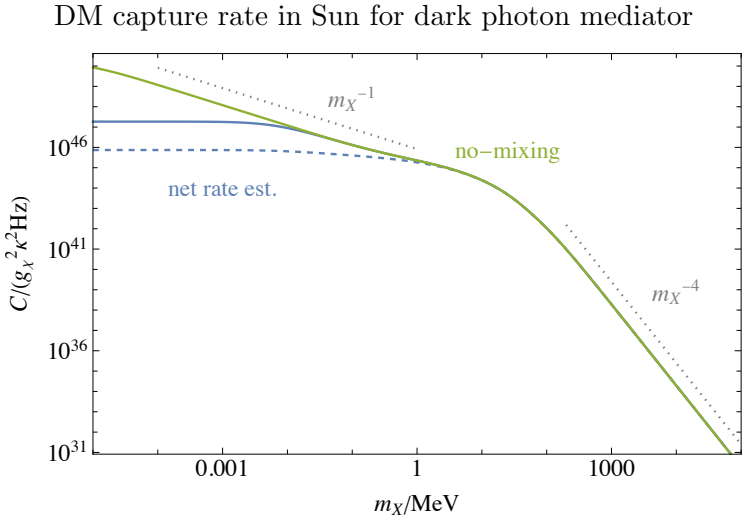

Figure 9. Estimate of total DM capture rate in the Sun for DM particles of mass $m_\chi = 50\,\mathrm{GeV}$ coupling through a dark photon mediator of mass m_X. The solid blue curve corresponds to the total down-scattering rate from unbound orbits into gravitational bound orbits, while the green curve corresponds to the capture rate ignoring mixing effects. The dashed blue curve corresponds to the approximate net capture rate described in Section 6.1. The dotted gray lines indicate different power law dependences on m_X.

transport. If DM has a significantly longer mean free path than photons in the star, then despite its much lower number density, it could contribute to heat transport, potentially changing the structure of the star by a detectable amount [24, 29–31]. For Population III stars, which may have formed at the cores of dense DM halos, other possible signatures such as BH formation have been proposed [23].

These potential observational signatures, in the Sun and in other stars, motivate proper calculations of DM scattering rates. In Appendix B.4, we derive formulae for vector self-energies in dilute non-relativistic plasmas (which translate simply to scalar self-energies, since all particles are non-relativistic); as far as we are aware, these formulae are novel. Below, we use these results to derive some features of DM scattering inside the Sun, illustrating how collective effects can be important, and how our formalism simplifies scattering calculations. We do not attempt a comprehensive investigation of DM scattering and its signatures in the Sun, though our methods should be useful for future work on these topics.

6.1 Solar capture with light mediator

Since, as mentioned above, collective effects (during the capture of halo DM particles) are most likely to be important for light mediators, we will investigate the effects of mediator mass on the capture rate of DM in the Sun. For DM coupling through a dark photon mediator, Figure 9 shows the capture rate for halo DM in the Sun, as a function of mediator mass (taking $m_\chi = 50\,\mathrm{GeV}$). This rate is estimated via calculating the per-volume capture rate in the core of the Sun, and multiplying this by the Solar volume. We take the halo DM velocity distribution to be an offset Maxwell distribution as described in Appendix E,

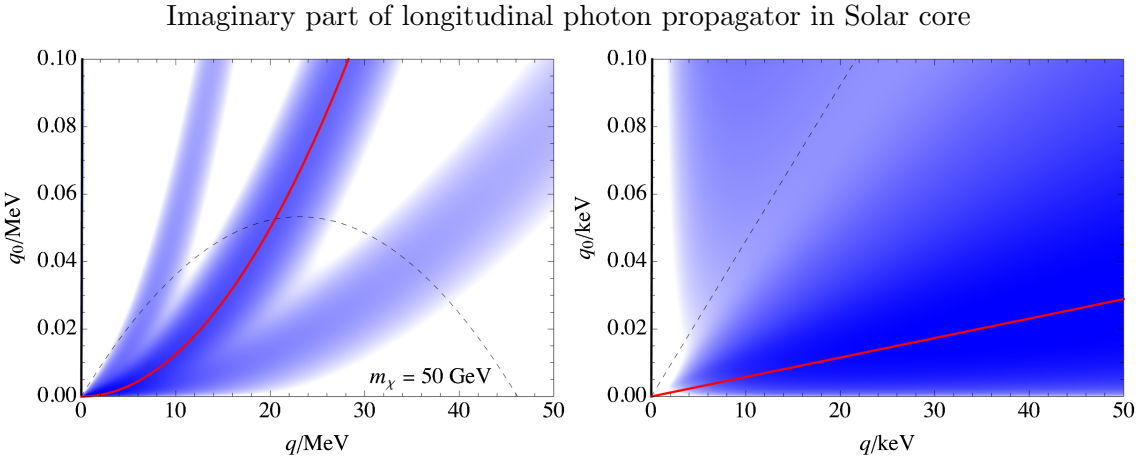

Figure 10. Density plot of the imaginary part of the longitudinal photon propagator Im $D_L(q_0, q)$ in the Solar core. Darker shades correspond to larger values of the imaginary part, on a logarithmic scale. The left panel shows the imaginary part at larger momentum transfers; the three bands correspond to scattering off H, ^{4}He, and heavier ions (from left to right). The dashed black line corresponds to $q_{0,\max}$ for a DM particle of mass $m_\chi = 50\,\text{GeV}$, travelling at the Solar core escape velocity. The red line corresponds to the zero-velocity ion dispersion relation $q_0 = \frac{q^2}{2m_i}$ for ^{4}He. The right panel shows the imaginary part at smaller momentum transfers. Here, the dashed black line is as per the left panel, while the red line corresponds to $q_0 = q\sigma_i$, where $\sigma_i \equiv \sqrt{T/m_i}$ is the thermal velocity dispersion for ^{4}He. As discussed in Section 6.1, the phase space around the red curve in the left-hand panel dominates the scattering rate for large mediator masses, while the space around the red curve in the right-hand panel dominates for small mediator masses.

with $v_0 \simeq 160\,\text{km}\,\text{s}^{-1}$ and $v_\star \simeq 240\,\text{km}\,\text{s}^{-1}$, and use the BS2005 model [112] for Solar core properties, taking into account scattering off H, ^{4}He, C, N, and O ions (heavier ions can be important for hard scatterings and heavier DM, but will not be significant for us).[17] More detailed computations are easily done, but our calculations are mostly intended to illustrate the physics involved. As we will see, even when collective effects are not important, the kinematics of scattering against a thermal distribution of SM target particles can lead to non-trivial behaviour, which our formalism makes it simple to compute.

For high enough mediator masses, scattering is effectively via contact interactions, and we have $C \sim m_X^{-4}$.[18] We start to deviate from this behaviour once m_X is small enough that momentum transfers $q \gtrsim m_X$ contribute significantly to the scattering rate, i.e. $m_X \lesssim m_\chi v_{\text{esc,core}} \simeq 3 \times 10^{-3} m_\chi$; this power-law break is visible in Figure 9. If the Solar core were cold, then as calculated in Section 4.6, the capture rate would scale as $\sim \log(1/m_X)$ for smaller m_X. However, the Solar core temperature is high enough that this does not hold for sufficiently small m_X; instead, as we can see from Figure 9, the scaling changes to $\sim m_X^{-1}$. In the full calculation, taking into account mixing effects, this

[17] More up-to-date Solar models, such as AGSS09 [113], are available, but are not importantly different for our purposes.

[18] The DM mass $m_\chi = 50\,\text{GeV}$ is small enough that nuclear form factor effects are not important for Solar capture, even for a heavy mediator.

scaling holds until m_X becomes small compared to screening scales (in the Solar core, the Debye scale $k_D \simeq 11\,\mathrm{keV}$).

We can derive these scalings analytically. Ignoring mixing effects, and taking the non-relativistic limit of Eq. (3.8), we have

$$\frac{dC}{dV} \simeq \frac{2g_\chi^2}{\pi} \int dq \frac{q}{(q^2+m_X^2)} \int_0^{q_{0,\max}} dq_0 \hat{F}_\infty(q_0)(1+f(q_0))\,\mathrm{Im}\,\Pi_L \tag{6.1}$$

For $q_0 \ll q$ (as is true for non-relativistic scattering), the contribution to the imaginary part of the photon self-energy from each plasma species is (from Appendix B.4)

$$\mathrm{Im}\,\Pi_L^{(i)} \simeq \frac{2\sqrt{\pi}e^2 Z_i^2 n_i}{q\sigma_i} \frac{1}{1+f(q_0)} e^{-(\xi_i-\delta_i)^2} \tag{6.2}$$

where the index i ranges over ion species plus electrons, and we have defined $\xi_i \equiv \frac{q_0}{\sqrt{2}q\sigma_i}$, $\delta_i \equiv \frac{q}{2\sqrt{2}m_i\sigma_i}$, where m_i is the mass of the i-th species, and $\sigma_i \equiv \sqrt{T/m_i}$ is its thermal velocity dispersion. The $1/(1+f(q_0))$ term in Eq. (6.2) cancels with the $1+f(q_0)$ term in Eq. (6.1), so the q_0 dependence of the integrand in Eq. (6.1) is purely through the ξ_i term in $e^{-(\xi_i-\delta_i)^2}$, and the $\hat{F}_\infty(q_0)$ term.

For small σ_i, the $e^{-(\xi_i-\delta_i)^2}$ term gives an exponential suppression unless the momentum transfer almost matches the on-shell ion dispersion relation, $q_0 \simeq q^2/(2m_i)$, as we would expect.[19] For $q_0 \ll m_\chi v_0^2$, where v_0 is the typical halo DM velocity, we have $\hat{F}_\infty(q_0) \underset{\sim}{\propto} q_0$ (see Figure 14), so the $\int dq_0$ integral in Eq. 6.1 scales as $\sim q^2$. Consequently, if we ignore mixing terms in $\mathrm{Im}\,\Pi_L$, the $\int dq$ integral in Eq. 6.1 scales as $\int dq \frac{q^3}{(q^2+m_X^2)^2} \sim \log m_X^{-1}$ for small enough m_X, and we have re-derived the logarithmic dependence we expected.

This derivation applies if we can always treat σ_i as small. However, for q small enough that $\delta_i \lesssim 1$, we simply need $\xi_i \lesssim \mathcal{O}(1)$ in order for $e^{-(\xi-\delta_i)^2}$ not to be an exponential suppression, rather than $\xi_i \simeq \delta_i$. That is, we simply need the transfer phase velocity $v_{\mathrm{ph}} \equiv q_0/q$ to be $\lesssim \sigma_i$, rather than almost equal to $q/(2m_i)$, the phase velocity on the ion dispersion relation. This is illustrated in Figure 10; for $q \gtrsim 2m_i\sigma_i$, the dispersion relation bands are separated from the horizontal axis, while for smaller q, they are not (as per the right-hand panel of Figure 10).

For these smaller q, the $\int dq_0$ integral is dominated by $q_0 \sim q\sigma_i$ (assuming $v_\chi > \sigma_i$, which is the case for the Sun, as illustrated in Figure 10). If this q_0 is small enough to be in the $\hat{F}_\infty(q_0) \sim q_0$ regime, then the $\int dq$ integral scales as $\int dq \frac{q^2}{(q^2+m_X^2)^2} \sim m_X^{-1}$ overall. For the $m_\chi = 50\,\mathrm{GeV}$ DM mass considered in Figure 9, we have $m_i\sigma_i^2 = T \simeq \mathrm{keV} \ll m_\chi v_0^2 \simeq 14\,\mathrm{keV}$, where v_0 is the halo DM velocity dispersion, so if $q \lesssim 2m_i\sigma_i$, then $q_0 \sim q\sigma_i$ is small enough for $\hat{F}_\infty(q_0)$ to be in the linear regime (Figure 14). Consequently, for m_X small enough that $\delta_i \lesssim 1$ dominates the capture rate integral, the total capture rate scales

[19] Unlike in the WD case analysed in Section 4.3, there are not narrow acoustic resonances that we can resonantly scatter into. Since the electron and ion velocities in the Sun are thermal, with the same temperature, the imaginary part of Π_L is comparable to the real part, along the $Q^2 - \mathrm{Re}\,\Pi_L = 0$ 'dispersion relation' [114], and we do not have a narrow pole, as illustrated in Figure 10. In a cold WD, the electrons have large velocities due to the Fermi sea, and we do obtain a well-defined pole for the ion acoustic mode, as per Figure 2.

as m_X^{-1}. In the Solar core, $m_i\sigma_i \sim$ few $\times$ MeV (for the different ion species), so the capture rate should scale as m_X^{-1} for $m_X \ll$ MeV, as we observe in Figure 9.[20] This calculation illustrates how, even in settings where collective effects are not important, our formalism can make including thermal kinematic effects simple, since the self-energies incorporate all of the necessary information about the velocity distributions of the SM particles.

One caveat regarding these capture rates is that they apply to down-scattering of halo DM from unbound to bound orbits. As discussed in Section 3, if the temperature of the star is important for capture, then we also expect *up-scattering* of captured DM into unbound orbits to be significant, once enough captured DM has been built up. Correspondingly, the solid curves shown in Figure 9 give the net DM capture rate before DM has built up in the Sun. To compute the net capture rate once dynamic equilibrium has been reached would require a full treatment of DM scattering and evolution post-capture. We do not attempt that here — instead, Figure 9 shows a plausible estimate for the equilibrium net capture rate (the dashed blue curve), from assuming that the DM phase space density in bound orbits is the same as the halo DM phase space density in just-escaping orbits. That is, we take

$$\frac{dC_{\rm net}}{dV} \simeq \frac{2g_\chi^2}{\pi}\int dq \frac{q}{(q^2+m_X^2)}\int_0^{q_{0,\rm max}} dq_0 \left(\hat{F}_\infty(q_0)(1+f(q_0)) - q_0\hat{f}_\infty(0)f(q_0)\right) \mathrm{Im}\,\Pi_L \tag{6.3}$$

In situations where the capture rate is dominated by low-q_0 scatterings, it is plausible that the phase space density for bound orbits just below $E_{\rm esc}$ is similar to the phase space density for halo DM trajectories just above $E_{\rm esc}$, in which case Eq. (6.3) should be a good approximation. We leave a more careful treatment of DM build-up in the Sun to future work.

6.1.1 Solar basin scattering

A non-DM example in which Solar scattering via a light mediator can be important is the scenario of a 'Solar Basin' of millicharged particles [116]. The idea is that light ($\lesssim$ keV mass) particles with a small coupling to the photon (or to a light dark photon mediator) would be produced in the Sun, and in particular, some would be produced on bound orbits. These may survive in the Solar system over very long timescales, and so build up in density until they are detectable in Earth-based experiments [117–121]. To calculate the present-day density of such particles at Earth, it is important to take into account possible scatterings within the Sun, which may scatter Solar basin particles into different orbits (or eject them from the Solar system entirely).

Doing these scattering calculations properly requires taking into account the thermal velocities of the SM particles inside the Sun, and the Q-dependent screening of the mediator, as our formalism automatically includes. Compared to the estimate in [116], which ignores

[20] In recent work [115], it was claimed that the capture rate (from a no-mixing calculation) scales as m_X^{-2} in this regime. [115] appears to derive this conclusion from somewhat complicated numerical calculations, rather than analytic arguments, and it is not clear where they differ from our analyses. We have confirmed that our calculations match the results of directly simulating scattering events for many randomly-generated particles.

thermal velocities and approximates screening with a constant Debye scale, preliminary calculation using our approach give a scattering rate $\mathcal{O}(100)$ times larger, which could be significant for the evolution of Solar basin particles. We leave a full calculation to future work.

6.2 Solar reflection

As mentioned above, light enough DM can be significantly accelerated by scattering with electrons in the Solar core, resulting in a high-energy 'reflected' flux which could be detected on Earth. The most recent calculations [101] for this Solar reflection scenario consider models with DM coupling through a heavy mediator, as well as models with DM coupling via a light dark photon. For the latter, they do attempt to take screening into account. In our terms, their formulae correspond to $\mathrm{Im}\,\Pi_L/(|Q^2 - \Pi_L^{\mathrm{Vlasov}}|^2)$, compared to the full expression $\mathrm{Im}\,\Pi_L/(|Q^2 - \Pi_L|^2)$, where Π_L^{Vlasov} is the fluid approximation to the self-energy, as reviewed in Appendix B.4. However, since $\xi_e \lesssim 1$ and $\delta_e \lesssim 1$ in electron scattering events (the DM is accelerated to at most the electron speed), the Vlasov approximation to Π_L will be $\mathcal{O}(1)$ correct, and using our full expressions makes only a small difference to the overall rates.

For other mediators, [101] neglected collective effects, whereas we have emphasised that these apply even to heavy mediators. However, since the DM masses of interest are generally $\gtrsim 100\,\mathrm{keV}$, to avoid other constraints, we need momentum transfers $\gtrsim 10\,\mathrm{keV}$ to give the DM $\gtrsim$ keV kinetic energies, relevant for detection in experiments on Earth. Since the Debye scale in the Sun is also $\sim 10\,\mathrm{keV}$, we would expect collective effects to have $\mathcal{O}(1)$ (rather than parametrically large) effects on signal rates. We leave more precise calculations to future work. Nevertheless, it is likely that, for the lower end of the DM mass range considered in [101], collective effects could be quantitatively important even for heavy mediator models.

7 Conclusions

In this paper, we have showed how collective effects in dense stellar media can significantly modify DM scattering rates. For DM scattering via contact interactions, we illustrated that scattering rates in WDs and NSs for DM masses $\lesssim 100\,\mathrm{MeV}$ can be either parametrically above or parametrically below the results of naive calculations, depending on the model. For scattering via a light mediator, naive capture rate calculations diverge due to long-range interactions, so collective effects are always important; our formalism allows them to be computed systematically. While collective effects of these kinds have been investigated in a range of contexts relevant to laboratory DM detection experiments (though even there, our setup can offer new insights, e.g. [35]), they have predominantly been ignored for scattering in astrophysical media. Since DM scattering in stars could lead to a wide range of potential observational signatures that could give strong constraints or discovery potential for DM, understanding the physics of such scatterings is phenomenologically important.

The aim of this paper has been to present a systematic formalism for computing scattering rates in media, and to illustrate its application with some simple examples. We

have not attempted to perform comprehensive analyses of different stellar models, different DM models, and their phenomenological consequences. This is the most obvious avenue for future work based on our results.

For stellar media whose underlying physics is known, performing such analyses is a fairly well-defined exercise. Properly treating DM scattering in NSs, on the other hand, is more difficult problem. While our toy calculations, and EM sum rule bounds for dark photon mediators, suggest that collective effects will be significant for DM masses $\lesssim 100\,\mathrm{MeV}$ even for contact interactions, they do not provide reliable predictions. Given the current uncertainty surrounding the basic physics of neutron star cores, making precise predictions is likely to be difficult, but it may be possible to derive useful bounds on scattering rates, e.g. by considering scattering in the better-understood crust [8].

Among different DM candidates, a class of models where our techniques will apply, but may have qualitatively different behaviour, is inelastic DM [122]. Compact stars are excellent potential probes of inelastic DM, since the large kinetic energy of infalling DM enables upscattering to states separated by larger energy splittings than in a terrestrial detector [2]. Upscattering can also be important in the Sun, from the high thermal velocities of electrons in the Solar core [123]. Inelastic scatterings involve different regions of (q_0, q) parameter space from the elastic scattering events we have considered in this paper, but can be treated via obvious extensions of our methods.

Another area in which our calculations should prove useful is the computation of particle emission rates from astrophysical media. The impact of collective effects on such processes has been explored in a wide range of papers, and was presented systematically in [36]. However, there are a range of particle candidates and emission environments for which only partial or flawed calculations have been presented (e.g. the example of resonant scalar emission from supernovae discussed in Appendix F). Important ingredients for all of these calculations are particle self-energies, as presented in Appendices B and C.

In addition to stars, another obvious astrophysical setting for dense plasmas is the hot early universe. At some level, collective effects will apply to DM scattering with the SM plasma in the early universe. For contact interactions, a generic issue is that, post-electron-freezeout, the number density of charged particles in the universe is very small (compared to the photon number density), and the collective scales are correspondingly small. Pre-electron-freezeout, relativistic abundances of charged particles are present, and collective scales can be large; however, effects from this era are often hard to observe in the late universe, having been thermalised along the way. For light mediators, on the other hand, collective effects in DM-SM scattering can be important even for small screening scales, as explored in various papers [124–126]. These generally use a fixed 'Debye mass' to incorporate screening, rather than the full thermal effects, which may sometimes make an appreciable difference.

In some circumstances, it is useful to treat the hidden sector itself as a medium with which particles can scatter. For example, if we consider DM interacting via a light mediator, then DM self-scattering can be calculated using the self-energy of the mediator in the DM medium. This provides a systematic way to perform such calculations, and should allow discrepancies between existing treatments [127, 128] to be resolved, as well as encompassing

collective effects such as those investigated in [92].

All of these avenues remain open and are ripe for further research. Regardless, the examples presented in this paper illustrate the importance of considering collective effects when studying DM in astrophysical settings. We hope that the formalism presented here, as well as the equations presented in the Appendices, will be useful to researchers seeking to robustly understand the dynamics of DM in astrophysical settings.

Acknowledgments

We thank Asimina Arvanitaki, Masha Baryakhtar, Tongyan Lin, Tanner Trickle, Ken Van Tilburg, and Zhengkang Zhang for helpful conversations, and Masha Baryakhtar and Maxim Pospelov for comments on a draft of this paper. Some of the computing for this project was performed on the Sherlock and Farmshare clusters. We would like to thank Stanford University and the Stanford Research Computing Center for providing computational resources and support that contributed to these research results. RL and MG's research is supported in part by the National Science Foundation under Grant No. PHYS-2014215, and the Gordon and Betty Moore Foundation Grant GBMF7946. WD is supported by the U.S.A. Department of Energy, Grant No. DE-SC0010107.

A In-medium scattering rates

As discussed in Section 2, the scattering rate for a particle passing through a medium can be related to the imaginary part of the particle's effective in-medium propagator. For a weakly-coupled, thermal medium, we can calculate this using the tools of thermal field theory [40]. In this Appendix, we will give explicit formulae for the scattering rate in some simple situations, considering spin-0 and spin-1/2 particles, coupled via spin-0 and spin-1 mediators (with scalar and vector couplings). Straightforward extensions of these formulae apply to other kinds of DM-mediator couplings, e.g. pseudoscalar couplings, DM form factors, inelastic scattering, etc.

A.1 Spin-1/2 DM

A.1.1 Vector mediator

Suppose that we have a Dirac fermion χ (our DM particle), coupled to a vector mediator X of mass m_X, $\mathcal{L} \supset g_\chi X_\mu \bar{\chi}\gamma^\mu\chi$. If a χ particle is passing through a uniform (though not necessarily isotropic) medium, then at leading order in the (assumed weak) couplings between χ and X and between X and the medium, its scattering rate can be obtained from the imaginary part of the self-energy diagram

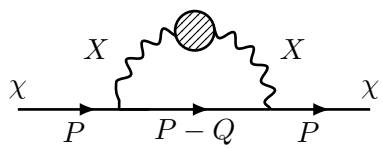

and is given by [40]

$$\Gamma = -\frac{2g_\chi^2}{E}\int \frac{d^3q}{(2\pi)^3}\frac{1}{2E'}(1+f(q_0))\frac{1}{(Q^2-m_X^2)^2}\,\mathrm{Im}\,\Pi^X_{\mu\nu}(Q)(P\cdot Q\eta^{\mu\nu}+P^\mu(P-Q)^\nu+P^\nu(P-Q)^\mu) \tag{A.1}$$

where $\Pi^X_{\mu\nu}$ is the in-medium self-energy for the mediator, $P=(E,p)$, and q_0 is such that $P-Q=(E',p')$ puts χ on-shell. If the SM current that the mediator couples to is conserved (or more generally, if current non-conserving processes are unimportant in the medium), then we have the Ward identity $Q^\mu\Pi_{\mu\nu}(Q)=0$, which we can use to write

$$\Gamma = -\frac{2g_\chi^2}{E}\int \frac{d^3q}{(2\pi)^3}\frac{1}{2E'}(1+f(q_0))\frac{1}{(Q^2-m_X^2)^2}\,\mathrm{Im}\,\Pi^X_{\mu\nu}(Q)\left(\frac{Q^2}{2}\eta^{\mu\nu}+2P^\mu P^\nu\right) \tag{A.2}$$

Specializing to an isotropic medium, we can decompose the self-energy as

$$\Pi_{\mu\nu} = \Pi_L\epsilon^L_\mu\epsilon^L_\nu + \Pi_T\sum_{i=1,2}\epsilon^i_\mu\epsilon^i_\nu \tag{A.3}$$

where ϵ^L_μ is the unit longitudinal polarization vector perpendicular to Q, and $\epsilon^{1,2}_\mu$ are the unit transverse polarization vectors (all quantities are functions of Q). Explicitly, if we take e.g. $Q_\mu=(q_0,0,0,q)$, then we can take

$$\epsilon^1_\mu=(0,1,0,0)\quad,\quad \epsilon^2_\mu=(0,0,1,0)\quad,\quad \epsilon^L_\mu=\frac{-1}{\sqrt{Q^2}}(q,0,0,q_0)=\frac{i}{\sqrt{|Q^2|}}(q,0,0,q_0) \tag{A.4}$$

where the last equality holds for $Q^2<0$, as we are interested in for scattering. Using this decomposition, we have $\Gamma=\Gamma_L+\Gamma_T$, where

$$\Gamma_L = \frac{4g_\chi^2}{E}\int \frac{d^3q}{(2\pi)^3}\frac{1}{2E'}(1+f(q_0))\frac{1}{(Q^2-m_X^2)^2}\left(E^2-p^2\cos^2\theta\right)\mathrm{Im}\,\Pi^X_L(Q) \tag{A.5}$$

and

$$\Gamma_T = \frac{2g_\chi^2}{E}\int \frac{d^3q}{(2\pi)^3}\frac{1}{2E'}(1+f(q_0))\frac{1}{(Q^2-m_X^2)^2}\left(-Q^2+2p^2\sin^2\theta\right)(-\,\mathrm{Im}\,\Pi^X_T(Q)) \tag{A.6}$$

We can change the integration variables to q_0, q to get

$$\Gamma_L = \frac{g_\chi^2}{2\pi^2}\frac{1}{Ep}\int dq\,dq_0\,q(1+f(q_0))\frac{1}{(Q^2-m_X^2)^2}\left(E^2-p^2\cos^2\theta\right)\mathrm{Im}\,\Pi^X_L(Q) \tag{A.7}$$

and analogously for Γ_T. For non-relativistic scattering, the leading term in small v_χ is

$$\Gamma_L \simeq 2g_\chi^2\int \frac{d^3q}{(2\pi)^3}(1+f(q_0))\frac{1}{(q^2+m_X^2)^2}\,\mathrm{Im}\,\Pi^X_L(Q) \tag{A.8}$$

A.1.2 Scalar mediator

For a scalar mediator ϕ of mass m_ϕ, coupling to χ via $\mathcal{L} \supset g_\chi \phi \bar{\chi}\chi$, we have a similar formula for the scattering rate,

$$\Gamma = -\frac{2g_\chi^2}{E}\int \frac{d^3q}{(2\pi)^3}\frac{1}{2E'}(1+f(q_0))\frac{1}{(Q^2-m_\phi^2)^2}\left(2m_\chi^2 - Q^2/2\right)\mathrm{Im}\,\Pi^\phi(Q) \tag{A.9}$$

For a non-relativistic χ particle, this has leading-order form

$$\Gamma \simeq -2g_\chi^2\int \frac{d^3q}{(2\pi)^3}(1+f(q_0))\frac{1}{(Q^2-m_\phi^2)^2}\,\mathrm{Im}\,\Pi^\phi(Q) \tag{A.10}$$

Since $\bar{f}f \simeq \bar{f}\gamma^0 f$, we expect $\Pi^\phi \simeq \Pi^X_{00} = \frac{q^2}{Q^2}\Pi^X_L \simeq -\Pi^X_L$ if ϕ and X couple to SM fermions in same way, and the SM fermions are non-relativistic. So, in this limit, scattering via scalar and vectors mediators results in the same rate, as expected. (Note that nucleons in nuclei move at speeds $\mathcal{O}(0.1c)$, so we have deviations at the $\mathcal{O}(10^{-2})$ level even for non-relativistic matter — this can be important for lifting cancellations etc. [35]).

A.2 Spin-0 DM

A.2.1 Vector mediator

For complex scalar DM χ, interacting with a vector mediator X via $\mathcal{L} \supset i g_\chi X_\mu(\chi^*\partial^\mu\chi - \chi\partial^\mu\chi^*)$ (writing the three-particle coupling, which is the only one that contributes to the leading-order scattering rate), the scattering rate is given by

$$\Gamma = -\frac{4g_\chi^2}{E}\int \frac{d^3q}{(2\pi)^3}\frac{1}{2E'}(1+f(q_0))\frac{1}{(Q^2-m_X^2)^2}P^\mu P^\nu\,\mathrm{Im}\,\Pi^X_{\mu\nu}(Q) \tag{A.11}$$

where we have used the Ward identity $Q_\mu\Pi^{\mu\nu}(Q) = 0$ as above. For an isotropic medium, splitting this into transverse and longitudinal parts gives

$$\Gamma = \frac{4g_\chi^2}{E}\int \frac{d^3q}{(2\pi)^3}\frac{1}{2E'}(1+f(q_0))\frac{1}{(Q^2-m_X^2)^2}\left(p^2\sin^2\theta(-\,\mathrm{Im}\,\Pi^X_T(Q)) - \frac{Q^2}{q^2}(E-q_0/2)^2\,\mathrm{Im}\,\Pi^X_L(Q)\right) \tag{A.12}$$

with leading non-relativistic form

$$\Gamma \simeq 2g_\chi^2\int \frac{d^3q}{(2\pi)^3}(1+f(q_0))\frac{1}{(Q^2-m_X^2)^2}\,\mathrm{Im}\,\Pi^X_L(Q) \tag{A.13}$$

This matches the expression for Dirac fermion DM, as expected.

A.2.2 Scalar mediator

For complex scalar DM χ, interacting with a scalar mediator ϕ as $\mathcal{L} \supset c_\chi\phi\chi^*\chi$, the scattering rate is given by

$$\Gamma = -\frac{c_\chi^2}{E}\int \frac{d^3q}{(2\pi)^3}\frac{1}{2E'}(1+f(q_0))\frac{1}{(Q^2-m_\phi^2)^2}\,\mathrm{Im}\,\Pi^\phi(Q) \tag{A.14}$$

(note that c_χ has dimensions of energy) with leading non-relativistic form

$$\Gamma \simeq -\frac{c_\chi^2}{2m_\chi^2}\int \frac{d^3q}{(2\pi)^3}(1+f(q_0))\frac{1}{(Q^2-m_\phi^2)^2}\,\mathrm{Im}\,\Pi^\phi(Q) \tag{A.15}$$

B Vector self-energies

As discussed in Section 2 and Appendix A, the scattering rate for DM passing through a uniform medium can be expressed in terms of the in-medium self-energy of the mediating particle. In this Appendix, we calculate the self-energy for a vector mediator X, which couples to SM Dirac fermions as $X_\mu \bar{f}\gamma^\mu f$, at leading order (i.e. treating the SM fermions as free). For weakly-coupled plasmas, this will give a good approximation, with other contributions being suppressed by higher powers of $\alpha_{\rm EM}$. Even for strongly-coupled plasmas, if there is an effective description in terms of weakly interacting quasi-particles (e.g. as per Fermi liquid theory [37]), these calculations can still apply.

B.1 One-loop free fermion

The leading-order self-energy in a medium of free Dirac fermions corresponds to the one-loop diagram

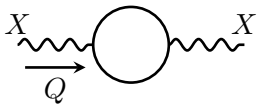

If we consider the electron contribution to the photon self-energy, we have

$$\Pi^{\mu\nu}(Q) = 4e^2 \int \frac{d^3k}{(2\pi)^3}\frac{1}{2E_k}(f_e(E_k)+f_{\bar{e}}(E_k))\frac{Q\cdot K(K^\mu Q^\nu + Q^\mu K^\nu) - Q^2 K^\mu K^\nu - (Q\cdot K)^2 g^{\mu\nu}}{(Q\cdot K)^2 - Q^4/4} \tag{B.1}$$

where f_e is the in-medium occupation number for electrons, and $f_{\bar{e}}$ for positrons. This expression agrees with those in [129] and [40]. In a thermal medium, with temperature T and chemical potential μ_e, we have $f_e(E) = (e^{(E-\mu_e)/T}+1)^{-1}$, and $f_{\bar{e}}(E) = (e^{(E+\mu_e)/T}+1)^{-1}$.[21] For Dirac fermions with an anomalous magnetic moment (e.g. neutrons), there are extra contributions, which are given in [97].

In [52, 129], it is mentioned that the $-Q^4/4$ term in the denominator of Eq. (B.1) 'can be ignored at $\mathcal{O}(e^2)$', and moreover, that it should be neglected to avoid introducing a spurious imaginary part. These statements are only true for timelike Q with $Q^2 = \mathcal{O}(eE)$, where E is the typical electron energy scale. For our scattering calculations, where we are interested in $Q^2 < 0$, keeping the $-Q^4/4$ term does not introduce any spurious imaginary part, and it is important to retain it to correctly treat scatterings with larger momentum transfers.

While the expressions we give in this section are presented for the electron contribution to the photon self-energy, it is simple to find the contribution to general vector mediator self-energies from general Dirac fermion species. We simply substitute the fermion-mediator coupling g_{Xf} for e, the fermion mass m_f for m_e, and the species' chemical potential μ_f for μ_e.

[21] our convention for the chemical potential is different from that of [41], which takes $f_e(E) = (e^{(E-m_e-\mu_e)/T}+1)^{-1}$ etc.

B.1.1 Imaginary part

We can evaluate the imaginary part of the self-energy either directly from Eq. (B.1), or by evaluating the cut self-energy [40]. From either method, we obtain (for the longitudinal mode)

$$\begin{aligned}\mathrm{Im}\,\Pi_L(Q) = -\frac{e^2}{4\pi}\frac{Q^2}{q^2}\frac{1}{q}\frac{\mathrm{sgn}(q_0)}{1+f(q_0)}\int_{R_Q} dE\,\mathrm{sgn}(E)\,\mathrm{sgn}(E')\times \\ (1-\tilde{f}(E))\tilde{f}(E')\left(\frac{Q^2}{2}+2EE'\right)\end{aligned} \tag{B.2}$$

where $E' = E - q_0$, and $\tilde{f}(E) \equiv (e^{(E-\mu_e)/T}+1)^{-1}$ is the fermionic occupation number for a medium with electron chemical potential μ_e and temperature T. The integration is over the range of E for which K and $K-Q$ can be on mass-shell, for appropriate directions of $\vec{k}$, i.e. $R_Q = \{E : |2Eq_0 - Q^2| \le |2kq| \text{ and } |E| \ge m_e\}$, where $k = \sqrt{E^2 - m_e^2}$. For the transverse modes,

$$\begin{aligned}\mathrm{Im}\,\Pi_T(Q) = -\frac{e^2}{4\pi}\frac{1}{q}\frac{\mathrm{sgn}(q_0)}{1+f(q_0)}\int_{R_Q} dE\,\mathrm{sgn}(E)\,\mathrm{sgn}(E')\times \\ (1-\tilde{f}(E))\tilde{f}(E')\left(-\frac{Q^2}{2}+k^2-\frac{(2Eq_0-Q^2)^2}{4q^2}\right)\end{aligned} \tag{B.3}$$

B.1.2 Real part

To evaluate the longitudinal and transverse self-energies in an isotropic medium, we can reduce the integral in Eq. (B.1) to an integral over the fermion energy, by doing the angular integrals analytically. Taking $K = (E, k)$ to be the four-momentum of the fermion in the loop, we can define $x \equiv Q\cdot K = Eq_0 - kq\cos\theta$, with extreme values $x_\pm \equiv Eq_0 \pm kq$ (where E and k are such that $K^2 = m_e^2$). In terms of $x_\pm$, the real parts of the self-energy are

$$\begin{aligned}\mathrm{Re}\,\Pi_L(Q) = \frac{Q^2}{q^2}\frac{e^2}{2\pi^2}\frac{1}{q}\int_{m_e}^{\infty} dE(f_e(E)+f_{\bar{e}}(E))\times \\ \left[-2kq-\left(E(E-q_0)+\frac{Q^2}{4}\right)\log\left|\frac{x_+-\frac{Q^2}{2}}{x_--\frac{Q^2}{2}}\right|\right. \\ \left.+\left(E(E+q_0)+\frac{Q^2}{4}\right)\log\left|\frac{x_++\frac{Q^2}{2}}{x_-+\frac{Q^2}{2}}\right|\right]\end{aligned} \tag{B.4}$$

and

$$\begin{aligned}\mathrm{Re}\,\Pi_T(Q) = \frac{e^2}{2\pi^2}\frac{1}{q}\int_{m_e}^{\infty} dE(f_e(E)+f_{\bar{e}}(E))\times \\ \left[2kq\left(1+\frac{Q^2}{2q^2}\right)\right. \\ +\frac{1}{2}\left(-k^2+\frac{Q^2}{2}+\frac{(Eq_0-Q^2/2)^2}{q^2}\right)\log\left|\frac{x_+-\frac{Q^2}{2}}{x_--\frac{Q^2}{2}}\right| \\ \left.+\frac{1}{2}\left(k^2-\frac{Q^2}{2}-\frac{(Eq_0+Q^2/2)^2}{q^2}\right)\log\left|\frac{x_++\frac{Q^2}{2}}{x_-+\frac{Q^2}{2}}\right|\right]\end{aligned} \tag{B.5}$$

B.2 Small-Q approximations

If we expand Eq. (B.4) and Eq. (B.5) in small Q^2, we obtain

$$\mathrm{Re}\,\Pi_L(Q) \simeq \frac{Q^2}{q^2}\frac{e^2}{\pi^2}\int_{m_e}^{\infty} dE\, k\,(f_e(E)+f_{\bar{e}}(E))\left[-1+\frac{Eq_0}{kq}\log\left|\frac{x_+}{x_-}\right|-\frac{Q^2E^2}{x_+x_-}\right] \tag{B.6}$$

in agreement with [129] (equation A17), and with [40] (equation 9.5), and

$$\mathrm{Re}\,\Pi_T(Q) \simeq \frac{e^2}{\pi^2}\int_{m_e}^{\infty} dE\, k\,(f_e(E)+f_{\bar{e}}(E))\left[\frac{q_0^2}{q^2}-\frac{Q^2}{q^2}\frac{Eq_0}{2kq}\log\left|\frac{x_+}{x_-}\right|\right] \tag{B.7}$$

in agreement with [40] (equation 9.4). These approximations are valid if $|Q^2| \ll |x_\pm|$ for the E that contribute significantly to the integral. For example, if the distribution is dominated by highly relativistic electrons, then this condition becomes $q \ll E$.

B.3 Degenerate fermion gas

For simple forms of $\tilde{f}(E)$, we can evaluate the one-loop self-energy expressions analytically. An example is a fully degenerate Fermi gas, for which $\tilde{f}(E) = \mathbb{1}_{0\le E<\mu_e}$ (if μ_e is positive). For physical systems, this is a good approximation if $T \ll \mu_e$, as we discuss in Section B.3.1.

We will mostly be interested in scattering events resulting in energy loss, so we will assume $Q^2 < 0$ and $q_0 > 0$ for simplicity (other kinematic regions can be analysed similarly). To obtain $\mathrm{Im}\,\Pi_L$, we can perform the integral in Eq. (B.2) over final state energies in the range $[E_+, \mu_e + q_0]$, where

$$E_+ \equiv \max\left(\mu_e, \frac{1}{2}\left(q_0 + q\sqrt{1-4\frac{m_e^2}{Q^2}}\right)\right) \tag{B.8}$$

(if $E_+ \ge \mu_e + q_0$, the integral is zero). This gives

$$\mathrm{Im}\,\Pi_L(Q) \simeq -\frac{e^2}{4\pi}Q^2q^3\,\mathrm{sgn}(q_0)\left(-\frac{2E_+^3}{3}+\frac{2\mu_e^3}{3}+E_+^2q_0+\mu_e^2q_0-\frac{q_0^3}{3}-\frac{E_+Q^2}{2}+\frac{\mu_eQ^2}{2}+\frac{q_0Q^2}{2}\right) \tag{B.9}$$

For the transverse part,

$$\begin{aligned}\mathrm{Im}\,\Pi_T(Q) \simeq -\frac{e^2}{4\pi}\frac{1}{q}\,\mathrm{sgn}(q_0)\Big(&-m_e^2(-E_+ +\mu_e+q_0)+\frac{-E_+^3+(\mu_e+q_0)^3}{3}\\ &-\frac{q_0^2(-E_+^3+(\mu_e+q_0)^3))}{3q^2}-\frac{(-E_+ +\mu_e+q_0)Q^2}{2}\\ &+\frac{q_0(-E_+^2+(\mu_e+q_0)^2)Q^2)}{2q^2}-\frac{(-E_+ +\mu_e+q_0)Q^4}{4q^2}\Big)\end{aligned} \tag{B.10}$$

We can also integrate the expressions for the real parts in Eq. (B.4) and Eq. (B.5) analytically, but the expressions are significantly more complicated — they are available in the code repository associated with this paper (github.com/wderocco/DarkScatter).

In the small Q^2 limit, Eq. (B.6) gives:

$$\mathrm{Re}\,\Pi_L(Q) \simeq \frac{e^2}{\pi^2}\frac{Q^2}{q^2}E_Fp_F\left(-1+\frac{z_F}{2}\log\left|\frac{1+z_F}{1-z_F}\right|\right) \tag{B.11}$$

and the imaginary part is

$$\operatorname{Im}\Pi_L(Q) \simeq -\frac{e^2 E_F p_F}{2\pi}\frac{Q^2}{q^2} z_F \Theta(1-|z_F|) \tag{B.12}$$

where $z_F \equiv \frac{q_0}{q v_F}$, with $v_F \equiv p_F/E_F$. The imaginary part is zero for $q_0 < 0$. The transverse equivalents are

$$\operatorname{Re}\Pi_T(Q) \simeq -\frac{e^2 E_F p_F}{2\pi^2}\left[-1 + \frac{z_F}{2\gamma_F^2}\log\left|\frac{1+z_F}{1-z_F}\right| + \frac{Q^2}{q^2}\left(-1 + \frac{z_F}{2}\log\left|\frac{1+z_F}{1-z_F}\right|\right)\right] \tag{B.13}$$

and

$$\operatorname{Im}\Pi_T(Q) \simeq \frac{e^2}{4\pi} E_F p_F z_F \left(\frac{Q^2}{q^2} + \frac{1}{\gamma_F^2}\right)\Theta(1-|z_F|) \tag{B.14}$$

where $\gamma_F \equiv E_F/m_e$.

B.3.1 Temperature effects

The formulae above were computed using the zero-temperature electron distribution functions. It turns out that these are good approximations when $T \ll \mu_e$, even for $q_0, q \ll T$.

For the real parts, this is fairly obvious — the formulae in Eqs. (B.4) and (B.5) do not depend strongly on the sharpness of the step function in $f_e(E)$. For the imaginary parts, the $(1-\tilde{f}(E))\tilde{f}(E-q_0)$ term in Eqs. (B.2) and (B.3) has integral

$$\int_{-\infty}^{\infty} dE(1-\tilde{f}(E))\tilde{f}(E-q_0) = \frac{q_0}{1-e^{-q_0/T}} = q_0(1+f(q_0)) \tag{B.15}$$

Consequently, the effect of changing T on the kernel $\frac{(1-\tilde{f}(E))\tilde{f}(E-q_0)}{1+f(q_0)}$ is simply to spread out the function in E, while keeping its integral fixed. Since the energy range $\sim T$ over which this kernel gets spread is small compared to the energies $\sim \mu_e$ at which it has support, the zero-temperature result is a good approximation for $T \ll \mu_e$.

From Appendix A, the total scattering rates depend on $\int\cdots\int dq_0(1+f(q_0))\operatorname{Im}\Pi_L^X(Q)$. Consequently, if the self-energy is dominated by degenerate Fermi gas contributions, then only the $1+f(q_0)$ part depends strongly on T, and we have that scatterings with $q_0 \ll T$ are enhanced by $\sim T/q_0$, as observed in [46, 98].

B.4 Dilute non-relativistic gas

Another situation in which we can evaluate Eq. (B.1) analytically is when our plasma species are dilute and non-relativistic. From Eq. (3.1), the occupation number is given by $f_e(E_v) = (2\pi)^3 \frac{n_e}{2m_e^3} p(v)$, where E_v is the energy of an electron with velocity v, and $p(v)$ is the probability distribution for electron velocities. The longitudinal mode self-energy is given by $\Pi_L = \frac{Q^2}{q^2}\Pi^{00}$, so

$$\begin{aligned}\Pi_L &\simeq \omega_p^2 \frac{Q^2}{q^2}\int d^3v\, p(v)\frac{2q_0(q_0 - v\cdot q) - Q^2 - (q_0 - v\cdot q)^2}{(q_0 - v\cdot q)^2 - \frac{Q^4}{4m_e^2}} \\ &= \omega_p^2 \frac{Q^2}{q^2}\int d^3v\, p(v)\frac{q^2 - (v\cdot q)^2}{(q_0 - v\cdot q)^2 - \frac{Q^4}{4m_e^2}}\end{aligned} \tag{B.16}$$

where $\omega_p^2 \equiv e^2 n_e/m_e$ is the plasma frequency. Since we are assuming that v is non-relativistic, the $(v\cdot q)^2$ term in the denominator will be negligible compared to the q^2 term. The integrand in Eq. (B.16) only depends on $v\cdot q \equiv q v_q$, where v_q is the component of the velocity parallel to q, so

$$\Pi_L \simeq \omega_p^2 Q^2 \int dv_q\, p_q(v_q) \frac{1}{(q_0 - q v_q)^2 - \frac{Q^4}{4m_e^2}} \equiv \omega_p^2 Q^2 S \tag{B.17}$$

where p_q is the probability distribution for v_q. We can write the integral S as

$$\begin{aligned} S &= \int dv\, p_q(v) \frac{1}{(q_0 - qv)^2 - \frac{Q^4}{4m_e^2}} \\ &= -\frac{m_e}{Q^2} \int dv\, p_q(v) \left(\frac{1}{\frac{Q^2}{2m_e} + q_0 - qv} - \frac{1}{-\frac{Q^2}{2m_e} + q_0 - qv} \right) \end{aligned} \tag{B.18}$$

For a Maxwell velocity distribution, $p_q(v) = \frac{1}{\sqrt{2\pi\sigma^2}} e^{-v^2/(2\sigma^2)}$, this gives

$$S = -\frac{m_e}{\sqrt{2} Q^2 \sigma} \int dv \frac{1}{\sqrt{\pi}} e^{-v^2/(2\sigma^2)} \left(\frac{1}{\frac{Q^2}{2m_e} + q_0 - qv} - \frac{1}{-\frac{Q^2}{2m_e} + q_0 - qv} \right) \tag{B.19}$$

Using the integral definition of the plasma dispersion function [114],

$$Z(\xi) = \frac{1}{\sqrt{\pi}} \int_{-\infty}^{\infty} dx \frac{e^{-x^2}}{x - \xi} \tag{B.20}$$

and writing $\xi = \frac{q_0}{\sqrt{2}\sigma q}$, we have

$$\begin{aligned} S &= \frac{m_e}{q_0 Q^2} \xi \left[Z\left(\xi \left(1 + \frac{Q^2}{2 q_0 m_e} \right) \right) - Z\left(\xi \left(1 - \frac{Q^2}{2 q_0 m_e} \right) \right) \right] \\ &\equiv \frac{m_e}{q_0 Q^2} \xi (Z(\xi - \delta) - Z(\xi + \delta)) \end{aligned} \tag{B.21}$$

where $\delta = \frac{-Q^2}{2\sqrt{2} q m_e \sigma}$. So,

$$\Pi_L \simeq \omega_p^2 \frac{m_e}{q_0} \xi (Z(\xi - \delta) - Z(\xi + \delta)) \tag{B.22}$$

To connect this to the usual approximations for Π_L, we can consider situations in which δ is small (we make this more precise below). Then, using the fact that $Z'(\xi) = -2(1 + \xi Z(\xi))$, we have that

$$Z(\xi - \delta) - Z(\xi + \delta) \simeq -2\delta Z'(\xi) = \frac{Q^2}{q_0 m_e} \xi Z'(\xi) = -\frac{2Q^2}{q_0 m_e} \xi (1 + \xi Z(\xi)) \tag{B.23}$$

This is a good approximation if $|\delta| \ll \max(1, |\xi|)$. In this regime,

$$\Pi_L \simeq -\omega_p^2 \frac{Q^2}{q^2} \frac{1}{\sigma^2} (1 + \xi Z(\xi)) \tag{B.24}$$

This is the 'Vlasov' approximation to the self-energy [114], which only depends on e, n_e and m_e through ω_p^2. It corresponds to treating each plasma species as a fluid, characterized by its charge-to-mass ratio e/m_e and its charge density en_e, rather than taking into account the kinematics of individual scattering events. For small $|\xi|$, corresponding to phase velocities small compared to electron velocities, the condition on δ is equivalent to $q \ll m_e\sigma$, so the Vlasov approximation is valid for momentum transfers much smaller than the typical electron momenta. For large $|\xi|$, we need $\frac{q^2}{2m_e} \ll q_0$. The useful aspect of our full formula, Eq (B.22), is that it simultaneously includes the kinematics of 'hard' scattering events, for which these conditions are not satisfied, as well as the coherent response to low-wavenumber perturbations.

To understand the behaviour of Π_L, we need the behaviour of the plasma dispersion function Z. In terms of the complex error function, we can write $Z(z) = i\sqrt{\pi}e^{-z^2}\,\mathrm{erfc}(-iz)$. Evaluated at real arguments (as is the case above), we have [130]

$$Z(x) = i\sqrt{\pi}e^{-x^2} - 2xY(x) \tag{B.25}$$

where

$$Y(x) = \frac{e^{-x^2}}{x}\int_0^x dt\, e^{t^2} \tag{B.26}$$

The real and imaginary parts of $Z(x)$ for real x are plotted in the left-hand panel of Figure 11. For large $|x|$, we have

$$\mathrm{Re}\, Z(x) \sim -\frac{1}{x}\left(1 + \frac{1}{2x^2} + \ldots\right) \tag{B.27}$$

while for small $|x|$,

$$\mathrm{Re}\, Z(x) \sim -2x\left(1 - \frac{2x^2}{3} + \ldots\right) \tag{B.28}$$

Figure 11 also plots the real and imaginary parts of $1 + xZ(x)$, which gives the Vlasov approximation to the self-energy (Eq. (B.24)).

It is easy to see that Eq. (B.24) corresponds to the expected plasma behaviour in the static and zero-momentum limits. In the static ($q_0 \to 0$) limit, we have $\xi \to 0$, so $\xi Z(\xi) \sim i\sqrt{\pi}\xi$, and consequently $\Pi_L \simeq \omega_p^2/\sigma^2$, giving the usual Debye screening scale. In the zero-momentum limit, $q \to 0$, we have $\xi \to \infty$, so $\xi Z(\xi) \sim -\left(1 + \frac{1}{2\xi^2}\right)$, so $\Pi_L \simeq \omega_p^2$, as expected.

We can obtain a simplified expression for the imaginary part of Eq. (B.22) when $q_0 \ll q$. In that case, $\delta \simeq \frac{q}{2\sqrt{2m_e\sigma}}$, and we have $\xi\delta \simeq \frac{q_0}{4T}$. Consequently,

$$\mathrm{Im}(Z(\xi-\delta) - Z(\xi+\delta)) \simeq 2\sqrt{\pi}e^{-(\xi^2+\delta^2)}\sinh\left(\frac{q_0}{2T}\right) = \sqrt{\pi}e^{-(\xi-\delta)^2}\frac{1}{1+f(q_0)} \tag{B.29}$$

so

$$\mathrm{Im}\,\Pi_L \simeq \frac{\pi}{\sqrt{2}}\frac{e^2 n_e}{q\sigma}\frac{1}{1+f(q_0)}e^{-(\xi-\delta)^2} \tag{B.30}$$

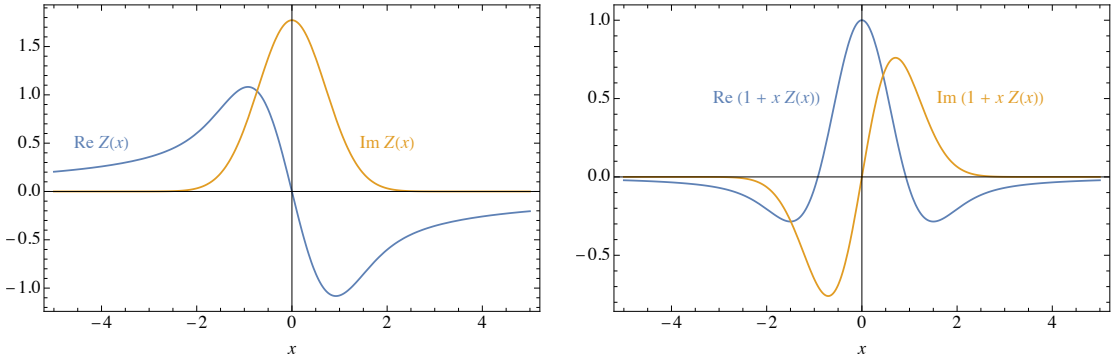

Figure 11. *Left:* plots of real (blue curve) and imaginary (orange curve) parts of the plasma dispersion function $Z(z) = i\sqrt{\pi}e^{-z^2}\mathrm{erfc}(-iz)$, evaluated for real arguments. *Right:* real (blue) and imaginary (orange) parts of $1 + zZ(z)$, as arises in Vlasov approximations to self-energies (Eq. (B.24)).

B.4.1 Yukawa scattering rate

As an illustration, we can put together the scattering rate expressions from Appendix A with the $\mathrm{Im}\,\Pi_L$ expression from Eq. (B.30) to see how, for a sufficiently dilute non-relativistic plasma, we recover the particle-by-particle Yukawa scattering rate. The total Yukawa cross section for particle-by-particle scattering is

$$\sigma_{\chi e} = \frac{g_\chi^2 g_e^2}{\pi} \frac{\mu_{\chi e}^2}{m_X^2(m_X^2 + 4k_{\mathrm{CM}}^2)} \tag{B.31}$$

where $\mu_{\chi e}$ is the DM-electron reduced mass, and k_{cm} is the momentum in the CoM frame. If we consider a heavy mediator, and assume that the relative velocity is dominated by the DM velocity v_χ in the plasma rest frame, then the scattering rate is

$$\Gamma_L \simeq n_e \sigma_{\chi e} v_\chi \simeq \frac{g_\chi^2 g_e^2}{\pi} \frac{\mu_{\chi e}^2}{m_X^4} n_e v_\chi \tag{B.32}$$

From Eq. (A.8), the rate for non-relativistic DM scattering, in terms of the mediator self-energy, is

$$\Gamma_L \simeq \frac{g_\chi^2}{2\pi^2} \frac{1}{v_\chi} \int dq\, dq_0\, q(1 + f(q_0)) \frac{1}{(q^2 + m_X^2)^2} \mathrm{Im}\,\Pi_L^X(Q) \tag{B.33}$$

If the medium is dilute enough for the mixing terms in $\mathrm{Im}\,\Pi_L^X$ to be unimportant, then using Eq. (B.30), this gives

$$\Gamma_L \simeq \frac{1}{2\pi^2}\sqrt{\frac{\pi}{2}} \frac{g_e^2 g_\chi^2 n_e}{v_\chi \sigma m_X^4} \int dq \int dq_0\, e^{-(\xi-\delta)^2} = \frac{1}{4\pi} \frac{g_e^2 g_\chi^2 n_e}{v_\chi m_X^4} q_{\mathrm{max}}^2 = \frac{g_\chi^2 g_e^2}{\pi} \frac{\mu_{\chi e}^2 n_e v_\chi}{m_X^4} \tag{B.34}$$

matching the standard Yukawa rate. A useful aspect of the self-energy calculation is that it is very simple to take into account the electron velocity distribution and collective effects.

B.4.2 Transverse modes

For non-relativistic electrons, the transverse self-energy is given by

$$\Pi_T \simeq \omega_p^2 \int d^3v\, p(v) \frac{-Q^2 v^2 \cos^2\phi \sin^2\theta + (q_0 - vq\cos\theta)^2}{(q_0 - v\cdot q)^2 - \frac{Q^4}{4m_e^2}} \tag{B.35}$$

where θ is the angle between q and v. Doing the angular integrals, we obtain

$$\Pi_T \simeq \omega_p^2 \int dv_q p_1(v_q) \frac{(q_0 - qv_q)^2 - Q^2\sigma^2}{(q_0 - qv_q)^2 - \frac{Q^4}{4m_e^2}} \tag{B.36}$$

We can rewrite this in terms of Π_L,

$$\begin{aligned}
\Pi_T &\simeq \omega_p^2 \int dv_q p_1(v_q) \left(1 - \frac{Q^2\sigma^2 - \frac{Q^4}{4m_e^2}}{(q_0 - qv_q)^2 - \frac{Q^4}{4m_e^2}}\right) = \omega_p^2 \left(1 - Q^2\left(\sigma^2 - \frac{Q^2}{4m_e^2}\right) S\right) \\
&= \omega_p^2 \left(1 - \left(\sigma^2 - \frac{Q^2}{4m_e^2}\right) \frac{m_e}{q_0} \xi (Z(\xi - \delta) - Z(\xi + \delta))\right) \\
&= \omega_p^2 - \left(\sigma^2 - \frac{Q^2}{4m_e^2}\right) \Pi_L
\end{aligned} \tag{B.37}$$

A distinct qualitative feature of the transverse modes is their lack of static screening. Taking the limit of ξ small, so $\xi Z(\xi) \sim -i\sqrt{\pi}\xi$, we have

$$\Pi_T \simeq -i\omega_p^2 \sqrt{\frac{\pi}{2}} \frac{q_0}{q\sigma} \tag{B.38}$$

which goes to zero as $q_0 \to 0$, for fixed q. Consequently, there is no screening of static fields, only 'dynamical screening' of finite-frequency perturbations (this is actually a general property of QED plasmas, which holds at all orders in perturbation theory [40]).

C Scalar self-energies

In this section, we calculate the leading-order (one-loop) self-energies for a scalar mediator, coupling as $\mathcal{L} \supset \phi \bar{f} f$, to Dirac fermions f. As well as the scalar-scalar self-energy $\Pi^{\pi\phi}$, we also calculate the mixing self-energy $\Pi^{\phi\mu}$ with the SM photon. Similarly to the vector mediator case considered in Appendix B, the one-loop result will be a good approximation for weakly-coupled plasmas. This is less obvious in the scalar case, since the mixing self-energy is proportional to the (in-vacuum) electron mass m_e; in cases where $\alpha E^2 \gg m_e^2$, where E is a typical electron energy, one might worry that higher-order contributions dominate (as assumed in some papers [73]). However, we show that corrections to the one-loop result are subleading (with consequences as discussed in Appendix F).

C.1 One-loop free fermion

The scalar-scalar self-energy is given by

$$\Pi^{\phi\phi}(Q) = 4g_\phi^2 \int \frac{\mathrm{d}^3k}{(2\pi)^3} \frac{1}{2E_k} \left(f_e(E_k) + f_{\bar{e}}(E_k)\right) \frac{(Q\cdot K)^2 - m_e^2 Q^2}{(Q\cdot K)^2 - Q^4/4} \tag{C.1}$$

while the scalar-vector mixing self-energy is

$$\Pi^{\phi\mu}(Q) = 4g_\phi e m_e \int \frac{d^3k}{(2\pi)^3}\frac{1}{2E_k}(f_e(E_k) - f_{\bar{e}}(E_k))\frac{(Q\cdot K)Q^\mu - Q^2K^\mu}{(Q\cdot K)^2 - Q^4/4} \tag{C.2}$$

We note here that the expressions (C.1) and (C.2) correct some typos in the corresponding expressions from [81]. In particular, both have an extra overall factor of 4, and (C.2) has a minus sign between the electron and positron phase-space distributions. One way to understand this relative sign is to remember that, in the non-relativistic limit, a Yukawa potential is universally attractive, whereas a vector mediator couples to particles and antiparticles with opposite charges. While in diagrams such as Π^{AA} and $\Pi^{\phi\phi}$ this does not appear, as the relative sign gets squared, in the mixing diagram $\Pi^{\phi\mu}$ it survives.

C.1.1 Imaginary parts

For an isotropic medium, the imaginary parts are

$$\mathrm{Im}\,\Pi^{\phi\phi}(Q) = -\frac{g_\phi^2}{4\pi}\frac{\mathrm{sgn}(q_0)}{1+f(q_0)}\frac{2m_e^2 - Q^2/2}{q}\int dE\,\mathrm{sgn}(E)\,\mathrm{sgn}(E')(1-\tilde{f}(E))\tilde{f}(E') \tag{C.3}$$

and

$$\mathrm{Im}\,\Pi^{\mu}_{\phi A}(Q) = -\frac{\mathrm{sgn}(q_0)}{1+f(q_0)}\frac{g_\phi e m_e}{4\pi q}\int \mathrm{d}E\ (2K^\mu - Q^\mu)\,\mathrm{sgn}(E)\,\mathrm{sgn}(E')(1-\tilde{f}(E))\tilde{f}(E'), \tag{C.4}$$

where the integration is over R_Q, as defined in Section B.1.1.

The transverse part of $\Pi^{\mu}_{\phi,A}$ does not contribute in the corrections to the scalar propagator (there is no preferred direction). The longitudinal projection vector depends on the sign of Q^2. Using the convention

$$e_{L,\mu} \equiv -\frac{1}{q\sqrt{Q^2}}(q^2, q_0 q_i) = -\frac{1}{q}(q^2, q_0 q_i) \times \begin{cases} \frac{1}{\sqrt{Q^2}}, & Q^2 > 0 \\ \frac{1}{i\sqrt{|Q^2|}}, & Q^2 < 0 \end{cases} \tag{C.5}$$

we find

$$\mathrm{Im}\,\Pi^{L}_{\phi A}(Q) = -\frac{g_\phi e}{4\pi}\frac{\mathrm{sgn}(q_0)}{1+f(q_0)}\frac{m_e Q^2}{q^2\sqrt{Q^2}}\int dE\,(2E - q_0)\,\mathrm{sgn}(E)\,\mathrm{sgn}(E')(1-\tilde{f}(E))\tilde{f}(E') \tag{C.6}$$

$$\text{if } Q^2 > 0$$

$$= -\frac{g_\phi e m_e}{2\pi^2}\frac{Q^2}{q^2\sqrt{|Q^2|}}\int \mathrm{d}E\ [f_e(E) - f_{\bar{e}}(E)]\left[E\log\left|\frac{\left(x_- - \frac{Q^2}{2}\right)\left(x_+ + \frac{Q^2}{2}\right)}{\left(x_- + \frac{Q^2}{2}\right)\left(x_+ - \frac{Q^2}{2}\right)}\right| + \right.$$
$$\left. + \frac{q_0}{2}\log\left|\frac{\left(x_+ + \frac{Q^2}{2}\right)\left(x_+ - \frac{Q^2}{2}\right)}{\left(x_- + \frac{Q^2}{2}\right)\left(x_- - \frac{Q^2}{2}\right)}\right|\right] \tag{C.7}$$

$$\text{if } Q^2 < 0$$

C.1.2 Real parts

The real part of the scalar-scalar self-energy in an isotropic medium is

$$\mathrm{Re}\Pi_{\phi\phi} = 4g_\phi^2 \int_{m_e}^{+\infty} \frac{\mathrm{d}E}{(2\pi)^2} \left(\tilde{f}_e(E) + \tilde{f}_{\bar{e}}(E)\right) \left[k + \frac{m_e^2 - \frac{Q^2}{4}}{2q} \log\left|\frac{\left(x_+ + \frac{Q^2}{2}\right)\left(x_- - \frac{Q^2}{2}\right)}{\left(x_+ - \frac{Q^2}{2}\right)\left(x_- + \frac{Q^2}{2}\right)}\right|\right] \tag{C.8}$$

while the mixing self-energy with a longitudinal vector mode is

$$\mathrm{Re}\Pi^L_{\phi A} = \frac{g_\phi e m_e}{2\pi^2} \frac{Q^2}{q^2\sqrt{Q^2}} \int \mathrm{d}E\ (f_e(E) - f_{\bar{e}}(E)) \left[E \log\left|\frac{\left(x_- - \frac{Q^2}{2}\right)\left(x_+ + \frac{Q^2}{2}\right)}{\left(x_- + \frac{Q^2}{2}\right)\left(x_+ - \frac{Q^2}{2}\right)}\right| + \right.$$
$$\left. + \frac{q_0}{2} \log\left|\frac{\left(x_+ + \frac{Q^2}{2}\right)\left(x_+ - \frac{Q^2}{2}\right)}{\left(x_- + \frac{Q^2}{2}\right)\left(x_- - \frac{Q^2}{2}\right)}\right|\right] \tag{C.9}$$

$$\text{if } Q^2 > 0$$

$$= -\frac{g_\phi e}{4\pi} \frac{\mathrm{sgn}(q_0)}{1 + f(q_0)} \frac{m_e Q^2}{q^2\sqrt{|Q^2|}} \int dE\,(2E - q_0)\,\mathrm{sgn}(E)\,\mathrm{sgn}(E')(1 - \tilde{f}(E))\tilde{f}(E') \tag{C.10}$$

$$\text{if } Q^2 < 0$$

C.2 Degenerate Fermi gas – Small-Q approximations

Similarly to Appendix B.3, we can evaluate the self-energies analytically for a degenerate Fermi gas. Here, we write down the small-Q approximations:

$$\mathrm{Re}\,\Pi_{\phi\phi} \simeq \frac{g_\phi^2}{2\pi^2}\left[E_F p_F + 3m_e^2 \log\frac{m_e}{E_F + p_F} + m_e^2 \frac{q_0}{q} \log\left|\frac{E_F q_0 + p_F q}{E_F q_0 - p_F q}\right|\right] \tag{C.11}$$

$$\mathrm{Im}\,\Pi_{\phi\phi} \simeq -\frac{g_\phi^2}{2\pi} m_e^2 \frac{q_0}{q} \Theta\left(\left|\frac{v_F q}{q_0}\right| - 1\right) \tag{C.12}$$

For $Q^2 < 0$, the mixing self-energy is

$$\mathrm{Re}\,\Pi^L_{\phi A}(Q) \simeq -\frac{g_\phi^2}{2\pi} E_F m_e \frac{q_0}{q} \frac{q}{\sqrt{|Q^2|}} \Theta\left(\left|\frac{v_F q}{q_0}\right| - 1\right) \tag{C.13}$$

$$\mathrm{Im}\,\Pi^L_{\phi A}(Q) \simeq -\frac{g_\phi e m_e}{\pi^2} \frac{Q^2}{q^2} \frac{q}{\sqrt{|Q^2|}} p_F \left(-1 + \frac{z_F}{2} \log\left|\frac{1 + z_F}{1 - z_F}\right|\right) \tag{C.14}$$

while for $Q^2 > 0$,

$$\mathrm{Re}\,\Pi^L_{\phi A}(Q) \simeq \frac{g_\phi e m_e}{\pi^2} \frac{Q^2}{q^2} \frac{q}{\sqrt{Q^2}} p_F \left(-1 + \frac{z_F}{2} \log\left|\frac{1 + z_F}{1 - z_F}\right|\right) \tag{C.15}$$

$$\mathrm{Im}\,\Pi^L_{\phi A}(Q) \simeq -\frac{g_\phi^2}{2\pi} E_F m_e \frac{q_0}{q} \frac{q}{\sqrt{Q^2}} \Theta\left(\left|\frac{v_F q}{q_0}\right| - 1\right) \tag{C.16}$$

C.3 Electron mass corrections

As mentioned at the start of this Appendix, for weakly-coupled plasmas it is sufficient to use the one-loop results for the self-energies. In particular, the scalar-vector mixing self-energy $\Pi^{\phi L}$ for an electron-coupled scalar is proportional to m_e, the in-vacuum electron mass, even when m_e is much smaller than collective scales in the plasma. This is because the scalar coupling $\phi\bar{\psi}\psi = \phi(\bar{\psi}_R\psi_L + \bar{\psi}_L\psi_R)$ mixes chiralities, whereas vector couplings preserve chirality, $X_\mu\bar{\psi}\gamma^\mu\psi = X_\mu\bar{\psi}_L\gamma^\mu\psi_L + X_\mu\bar{\psi}_R\gamma^\mu\psi_R$. If electrons were massless, there would be no way to match these chiralities, so the mixing self-energy would be zero.

To demonstrate the stronger claim that the one-loop result is quantitatively a good approximation, rather than just scaling in the correct way with m_e, we perform an illustrative calculation for the case of a relativistic degenerate plasma. The most important corrections to the one-loop result come from replacing the electron propagators in the loop with in-medium propagators. The leading contribution to the electron self-energy $\Sigma(K)$ is

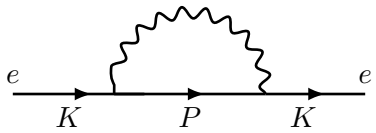

where K is the electron four-momentum. The in-medium propagator $S(K)$ is given by $-iS^{-1}(K) = \not{K} - m_e - \Sigma(K)$. For a degenerate electron gas, the integral is dominated by placing the internal electron with momentum P on-shell (rather than placing the photon on-shell, or considering positrons), and the real part of the self-energy Σ at one-loop order is given by

$$\Sigma(K) = 2e^2 \int \frac{\mathrm{d}^3p}{(2\pi)^3}\frac{1}{2E_p}\frac{2m_e - \not{P}}{(K-P)^2} f_e(E_p), \tag{C.17}$$

where $E_p = \sqrt{p^2 + m_e^2}$ and $K \equiv (k_0, \mathbf{k})$. We define an expansion of Σ in γ-matrices as $\Sigma(K) \equiv \gamma^0\Sigma_0 + \gamma^i k_i \Sigma_k + m_e\Sigma_m \equiv \not{\Sigma} + m_e\Sigma_m$. The three terms are given by

$$\Sigma_m = \frac{\alpha_{\mathrm{EM}}}{\pi k}\int_{m_e}^{+\infty} \mathrm{d}E \log\left|\frac{m_e^2 + k_0^2 - k^2 - 2Ek_0 + 2pk}{m_e^2 + k_0^2 - k^2 - 2Ek_0 - 2pk}\right| f_e(E), \tag{C.18}$$

$$\Sigma_0 = -\frac{\alpha_{\mathrm{EM}}}{2\pi k}\int_{m_e}^{+\infty} E\mathrm{d}E \log\left|\frac{m_e^2 + k_0^2 - k^2 - 2Ek_0 + 2pk}{m_e^2 + k_0^2 - k^2 - 2Ek_0 - 2pk}\right| f_e(E), \tag{C.19}$$

$$\Sigma_k = -\frac{1}{k^2}\left[-\frac{m_e^2 + K^2}{4}\Sigma_m - k_0\Sigma_0 + \frac{\alpha_{\mathrm{EM}}}{\pi}\int \mathrm{d}E\, p f_e(E)\right], \tag{C.20}$$

where $p \equiv \sqrt{E^2 - m_e^2}$ and $k \equiv |\mathbf{k}|$. In the zero temperature limit, the electron phase-space distribution is the step function $f_e(E) = \Theta(E_F - E)$.

In the one-loop expression for $\Pi^{\phi L}$ with in-medium electron propagators, the relevant Dirac trace is (for electron momenta K and $K - Q$ in the loop)

$$\begin{aligned}\Pi^{\phi\mu}(Q) &\propto \mathrm{tr}\left[(\not{K} - \not{\Sigma}(K) + m_e(1 + \Sigma_m(K)))\gamma^\mu(\not{K} - \not{Q} - \not{\Sigma}(K-Q) + m_e(1 + \Sigma_m(K-Q))\right] \\ &= 4m_e\left((1 + \Sigma_m(K-Q))(\not{K} - \not{\Sigma}(K)) + (1 + \Sigma_m(K))(\not{K} - \not{Q} - \not{\Sigma}(K-Q))\right)\end{aligned} \tag{C.21}$$

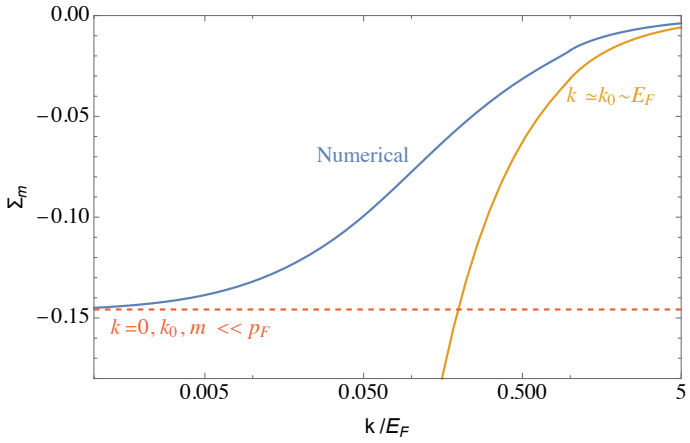

Figure 12. Plot of the quantity Σ_m, as defined in Eq. (C.18), for $\mu_e = 350$ MeV. The dashed line corresponds to the zero momentum approximation of Eq. (C.23), whereas the orange line corresponds to relativistic electrons and the approximation of Eq. (C.22). The blue line uses the full integral of Eq. (C.18) and the full numerical dispersion relation. This plot illustrates that corrections to the scalar-vector self energy $\Pi^{\phi L}$ from the 'modified electron mass' are small.

showing how this is proportional to the in-vacuum mass m_e. We are interested in evaluating this for K on the electron's in-medium dispersion relation [131]. For Q small, this means that the $\not{\Sigma}$ terms are $\sim eE_F$, so compared to the electron momenta $\sim E_F$ that dominate the loop integral, they do not change the result significantly (this is analogous to the argument for why the one-loop vector self-energies do not receive large corrections). The remaining question is how large the Σ_m terms are.

In Figure 12, we plot $\Sigma_m(k_0(k), k)$ (evaluated via Eq. (C.18)), solving numerically for the dispersion relation $k_0(k)$, for an ultra-relativistic degenerate electron gas. It is clear that the correction to $\Pi^{\phi\mu}$ is small for the entire range of k_0, k. We can understand some limiting cases analytically. For applications of interest, the electrons contributing the most have energies $\sim E_F \gg m_e$, for which $k_0 \simeq k$. In the limit $k_0 \simeq k \gg m_e$, we find

$$\Sigma_m \simeq \frac{\alpha_{\rm EM} E_F}{\pi k}\left[1 + \log\frac{m_e^2}{4E_F^2} + \frac{E_F - k}{E_F}\log\frac{|E_F - k|}{k}\right] \tag{C.22}$$

For smaller electron momenta k, the dispersion relation lies above the light-cone, so we can get some analytic handle in this case by considering the limit $k_0 \gg k$. Taking also $ep_F \gg m_e$, the $k_0 > 0$ dispersion relation and Σ_m are

$$k_0 \simeq \frac{ep_F}{2\sqrt{2}\pi}, \quad \Sigma_m \simeq -\frac{2\alpha_{\rm EM} p_F}{\pi k_0}\left(1 + \frac{k_0}{2p_F}\log\frac{2p_F}{k_0}\right) \simeq -\frac{e\sqrt{2}}{\pi}\left(1 + \frac{e}{4\pi\sqrt{2}}\log\frac{4\pi\sqrt{2}}{e}\right), \tag{C.23}$$

As we see from Figure 12, these approximations match the full integral well in their regions of validity.

D EM sum rule limits

Causality imposes constraints on the properties of in-medium propagators, and as discussed in Section 2.1, this allows us to place constraints on certain types of scattering rates. In particular, for a dark photon mediator, we have $\mathrm{Im}(\Pi^{XX}_{\mathrm{tot}})_{\mu\nu} = \kappa^2 Q^4 \,\mathrm{Im}\,(-iD_{\mu\nu})$, where $D_{\mu\nu}$ is the in-medium propagator for the SM photon, in Lorenz gauge. More specifically, $D_{\mu\nu}$ is the analytic continuation of the in-medium imaginary-time propagator. In the real-time formalism, we can write the photon propagator $(D_{\mu\nu})_{ab}$ as [40]

$$(D_{\mu\nu})_{ab}(Q) = \begin{pmatrix} \sqrt{n(q_0)+1} & \sqrt{n(q_0)} \\ \sqrt{n(q_0)} & \sqrt{n(q_0)+1} \end{pmatrix} \begin{pmatrix} D_{\mu\nu} & 0 \\ 0 & (D_{\mu\nu})^* \end{pmatrix} \begin{pmatrix} \sqrt{n(q_0)+1} & \sqrt{n(q_0)} \\ \sqrt{n(q_0)} & \sqrt{n(q_0)+1} \end{pmatrix} \tag{D.1}$$

where $n(q_0) \equiv (e^{|q_0|/T} - 1)^{-1}$, so $D_{\mu\nu}$ corresponds to the 'diagonal component'.

Consequently, to constrain the DM scattering rate via a dark photon mediator, we are interested in the properties of the SM photon propagator. In general, if we are allowed to tune the medium properties and the initial DM velocity, we can obtain arbitrarily large scattering rates, via matching the on-shell momentum transfers possible for the DM particle to the dispersion of weakly-damped excitations in the medium (so that we obtain resonant scattering at all momentum transfers). However, if we are interested in the average scattering rate across different incoming DM directions, such tuning is no longer possible, and as we will see, it is possible to place general limits on the scattering rate. Equivalently, instead of thinking in terms of averaging over different DM directions, we can consider a DM particle scattering from an isotropic medium (with mediator self-energy obtained by averaging over different orientations of the original medium).

In an isotropic medium, we can decompose $D_{\mu\nu}$ into transverse and longitudial parts,

$$D_{\mu\nu}(Q) = \frac{i}{Q^2 - \Pi_T(Q)} P^T_{\mu\nu} + \frac{i}{Q^2 - \Pi_L(Q)} P^L_{\mu\nu} \tag{D.2}$$

where $P^{T,L}_{\mu\nu}$ are the transverse and longitudinal projectors, and $\Pi_{T,L}$ are the transverse and longitudinal photon self-energies, respectively (we have elided the $i\epsilon$ prescription for evaluating contour integrals, since these ambiguities do not affect our calculations). We can also define (following [40]) the 'spectral density' quantities $\rho_L(Q) \equiv 2\frac{Q^2}{q^2}\,\mathrm{Im}\,D_L(Q)$, and $\rho_T(Q) \equiv 2\,\mathrm{Im}\,D_T(Q)$, where $D_L(Q) = \frac{-1}{Q^2 - \Pi_L(Q)}$, $D_T(Q) = \frac{-1}{Q^2 - \Pi_T(Q)}$. Both ρ_L and ρ_T are always non-negative, for both timelike and spacelike Q (this is the point of the Q^2/q^2 factor in the definition of ρ_L). From the Kramers-Kronig relations, we have the 'sum rules'

$$\int_0^\infty \frac{dq_0}{q_0} \rho_T(q_0, q) = \frac{\pi}{q^2} \tag{D.3}$$

$$\int_0^\infty \frac{dq_0}{q_0} \rho_L(q_0, q) = \pi \left(\frac{1}{q^2} - D_L(0, q) \right) = \frac{\pi k_S^2}{q^2(q^2 + k_S^2)} \tag{D.4}$$

which hold for any q, where $k_S^2 = \Pi_L(0, q)$ is the static longitudinal screening scale (so $D_L(0, q) = \frac{1}{q^2 + k_S^2}$). Since $\rho_{L,T} \geq 0$, the integral over any range of q_0 is also bounded by the corresponding RHS. The $\rho_{L,T} \geq 0$ condition also implies that either $k_S^2 \geq 0$, or $k_S^2 \leq -q^2$

— intermediate values would violate the positivity of the LHS. If $k_S^2 \geq 0$, corresponding to screening (rather than anti-screening) of static fields, then the RHS of Eq. (D.4) is $\leq \pi/q^2$. While $\Pi(0,q)$ should be non-negative at small enough q for a stable system [132], it is possible to have $\Pi(0,q) < 0$ at q comparable to lattice scales — for example, this is probably the case for some metals, such as aluminium [132]. However, to obtain k_S^2 very slightly below $-q^2$, which is required for the RHS of Eq. (D.4) to be $\gg \pi/q^2$, would require very strong antiscreening, which is most likely only possible for a system very close to instability [132]. In this work, we assume that π/q^2 is a good approximate bound for the RHS of Eq. (D.4) (as is the case for the toy models we consider), and leave a more thorough investigation for future work.

Given Eqs. (D.4) and (D.3), we can place bounds on the scattering rate via a dark photon mediator. From Appendix A, the longitudinal scattering rate is

$$\Gamma_L = \frac{-1}{4\pi^2}\frac{g_\chi^2\kappa^2}{Ep}\int dq dq_0\, q(1+f(q_0))\frac{Q^2q^2}{(Q^2-m_X^2)^2}(E^2-p^2\cos^2\theta)\rho_L(q_0,q) \tag{D.5}$$

For a given q, we can write the $\int dq_0$ integral as

$$I_0 \equiv \int \frac{dq_0}{q_0}\rho_L(q_0,q)\left(\frac{-Q^2q^2}{(Q^2-m_X^2)^2}(1+f(q_0))q_0(E^2-p^2\cos^2\theta)\right) \tag{D.6}$$

From Eq. (D.4), this can be bounded by π/q^2 times the maximum of the bracketed term within the relevant q_0 interval. To take a simple example, for non-relativistic scattering, the bracketed term is approximately equal to

$$\frac{m_\chi^2 q^4}{(q^2+m_X^2)^2}\frac{q_0}{1-e^{-q_0/T}} \tag{D.7}$$

This is maximized by taking q_0 to be as large as it can be, for the given q. If we take the mediator to be heavy, and the temperature to be negligible, then the scattering rate is bounded by

$$\Gamma_L \lesssim \frac{1}{4\pi}\frac{g_\chi^2\kappa^2}{v_\chi m_X^4}\int_0^{2m_\chi v_\chi} dq\, q^3\left(qv_\chi - \frac{q^2}{2m_\chi}\right) = \frac{16}{15}\frac{g_\chi^2\kappa^2}{4\pi}m_\chi v_\chi\left(\frac{m_\chi v_\chi}{m_X}\right)^4 \tag{D.8}$$

as derived in [35]. Similarly, for a light mediator, we have

$$\Gamma_L \lesssim \frac{g_\chi^2\kappa^2}{4\pi}m_\chi v_\chi \tag{D.9}$$

For relativistic χ, the bracketed term in Eq. (D.6) might not be maximized at the maximum value $q_{0,\max}$ of q_0, for given q. We attain $q_0 = q_{0,\max}$ at $\cos\theta = 1$, where θ is the scattering angle. Consequently, the $E^2 - p^2\cos^2\theta$ term in Eq. (D.5) is $= m_\chi^2$, which can be much smaller than its maximum value of E^2, if $E \gg m_\chi$. Consequently, it can be beneficial to take $\cos\theta$ somewhat smaller than 1. For example, in the case of a heavy mediator, the derivative of the bracketed term in Eq. (D.6) with respect to q_0, evaluated at $q_0 = q_{0,\max}$, is

$$\frac{E^2q^4}{m_X^4}\left((1-6v_\chi^2+5v_\chi^4)+\mathcal{O}(q/E)\right) \tag{D.10}$$

where we have expanded in large E. For small q, we can see that if $v_\chi \geq 1/\sqrt{5} \simeq 0.45$, then the derivative at $q_{0,\max}$ is negative, so the quantity is maximized at some smaller q_0. When this is true, we can still derive sum rule limits by optimizing numerically. Figure 13 shows the results of such numerical calculations; in the ultra-relativistic limit, the scattering rate upper-bound scales $\sim g_\chi^2 \kappa^2 E^5/m_X^4$ for a heavy mediator, and $\sim g_\chi^2 \kappa^2 E$ for a light mediator).

We can incorporate a non-zero medium temperature by keeping the $1 + f(q_0)$ factor in Eq. (D.6). However, as noted in Section 3, if the temperature is large enough to significantly affect scattering rates, then one is often interested in the *net* capture rate once upscattering has been taken into account.

D.1 Transverse limits

We can put similar bounds on the scattering rate via transverse dark photon modes. The total scattering rate is given by

$$\Gamma_T = \frac{1}{8\pi^2}\frac{g_\chi^2\kappa^2}{Ep}\int dq dq_0\, q(1+f(q_0))\frac{Q^4}{(Q^2-m_X^2)^2}(-Q^2+2p^2\sin^2\theta)\rho_T(q_0,q) \tag{D.11}$$

So, for given q, the $\int dq_0$ integral is

$$I_0 \equiv \int \frac{dq_0}{q_0}\rho_T(q_0,q)\left(\frac{Q^4}{(Q^2-m_X^2)^2}(1+f(q_0))q_0(-Q^2+2p^2\sin^2\theta)\right) \tag{D.12}$$

and we want to maximize the bracketed term over the relevant q_0 range. Since the $-Q^2 + 2p^2\sin^2\theta$ term is somewhat more complicated, in the non-relativistic case, than the equivalent in the longitudinal case, we simply optimize numerically. Doing so, as illustrated in Figure 13, we find that in the non-relativistic limit, the bound scales as

$$\Gamma_T \lesssim 1.16 \times \frac{g_\chi^2\kappa^2}{4\pi}\frac{m_\chi^5 v_\chi^7}{m_X^4} \tag{D.13}$$

for a heavy mediator (the parametric scaling can be obtained from taking the loose bound $-Q^2 + 2p^2\sin^2\theta \leq q^2 + 2p^2$; the numerics provide the constant) For a light mediator, we have $\Gamma_T \lesssim 0.53 \times \frac{g_\chi^2\kappa^2}{4\pi}$. We can see that at small v_χ, the transverse bounds are suppressed by $\sim v_\chi^2$ relative to the longitudinal bounds, as expected from the forms of Γ_L and Γ_T. Numerically, the Γ_T limit (for a heavy mediator) becomes larger than the Γ_L limit for $v \gtrsim 0.7$ — at ultra-relativistic velocities, Γ_T is ~ 7 times larger.

E DM velocity distribution

For our purposes, the most important quantity related to the DM halo velocity distribution is

$$F_\infty(\delta) \equiv \int_0^\delta dE_K f_\infty(m_\chi + E_K) \tag{E.1}$$

as introduced in Section 3. This definition is phrased in a manner appropriate to isotropic DM velocity distributions, for which f_∞ is purely a function of the energy. However, in

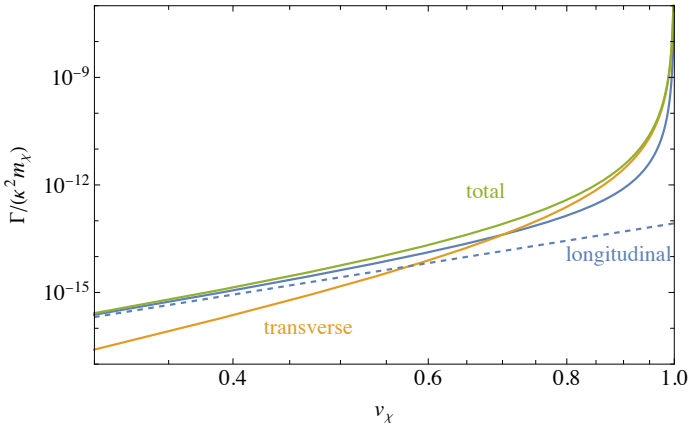

Figure 13. Plot of sum rule limits on the scattering rate for spin-1/2 DM via a heavy dark photon mediator (specifically, taking $m_X = 10^3 m_\chi$), in a cold medium, as a function of the DM particle's velocity v_χ. The green curve corresponds to the total limit, while the blue and orange curves correspond to the limits on the scattering rate via longitudinal and transverse modes respectively. The dotted blue line corresponds to the $\Gamma \propto v_\chi^5$ limit for non-relativistic velocities.

most cases, a star will have some non-zero velocity relative to the DM halo (which will not necessarily have an isotropic velocity distribution in any case [133–138]). Nevertheless, if the orientation of the star is unimportant for the capture rate (e.g. if the star is spherical, and the medium response is isotropic, both of which are reasonable approximations in the parameter space of interest to us), then we can imagine averaging over different orientations of the halo DM velocity distribution relative to the star, to obtain an isotropic velocity distribution in the rest frame of the star which would give the same capture rate. Consequently, we can take the more general definition

$$F_\infty(\delta) = \frac{m_\chi}{4\pi} \int_0^{v_\delta} d^3v \frac{f_\infty(m_\chi v)}{v} = \frac{2\pi^2 n_\chi}{g_s m_\chi^2} \int_0^{v_\delta} d^3v \frac{p_v(v)}{v} \tag{E.2}$$

where v_δ is such that $m_\chi v_\delta^2/2 = \delta$ (we assume that the DM halo velocities are non-relativistic), and we view f_∞ as a function of momentum.

In many circumstances, the halo DM velocity distribution in the rest frame of the star is reasonably well-modelled by an offset Maxwell distribution [99, 139], of the form

$$p_v(v) = (2\pi v_0^2)^{-3/2} \exp\left(-\frac{(v - v_\star)^2}{2v_0^2}\right) \tag{E.3}$$

where v_0 is the velocity dispersion of the DM halo, and $v_\star$ is the relative velocity of the star (a truncated Maxwell distribution, which is cut off for velocities higher than the halo escape velocity, can be a better approximation, but for integrals such as Eq. (E.2), which are weighted towards smaller v, this will make little difference). Using this form of the velocity distribution, we have

$$F_\infty(\delta) = \frac{n_\chi \pi^2}{g_s m_\chi^2 v_\star} \left(2\,\mathrm{erf}\left(\frac{v_\star}{\sqrt{2}v_0}\right) + \mathrm{erf}\left(\frac{v_\delta - v_\star}{\sqrt{2}v_0}\right) - \mathrm{erf}\left(\frac{v_\delta + v_\star}{\sqrt{2}v_0}\right)\right) \tag{E.4}$$

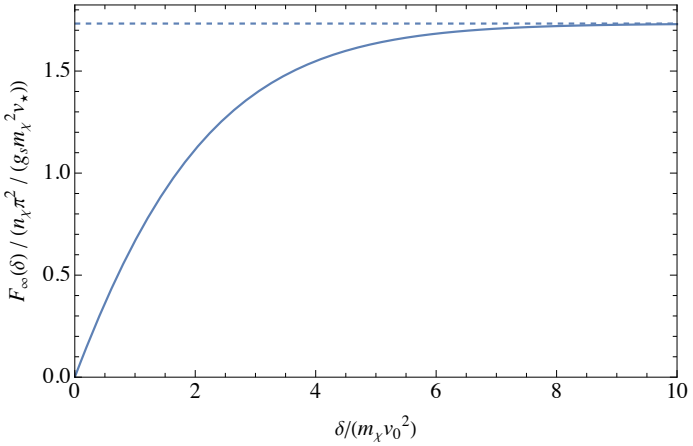

Figure 14. Plot of $F_\infty(\delta)$ from Eq. (E.4), for DM halo parameters $v_0 = 160\,\mathrm{km\,s^{-1}}$ and $v_\star = 240\,\mathrm{km\,s^{-1}}$ as used in the text. The dashed curve shows the asymptotic value of F_∞, from Eq. (E.6).

This function is plotted in Figure 14, for the $v_0 = 160\,\mathrm{km\,s^{-1}}$, $v_\star = 240\,\mathrm{km\,s^{-1}}$ parameters used in the text. In the limit of very small $v_\star$, this becomes

$$F_\infty(\delta) = \frac{(2\pi)^{3/2} n_\chi}{g_s m_\chi^2 v_0} \left(1 - e^{-\delta/(m_\chi v_0^2)}\right) \tag{E.5}$$

If capture is dominated by hard scatterings, then the quantity of interest is

$$F_\infty(\infty) = \frac{2\pi^2 n_\chi}{g_s m_\chi^2} \left\langle \frac{1}{v_\infty} \right\rangle \tag{E.6}$$

For an offset Maxwell distribution, we have

$$\left\langle \frac{1}{v_\infty} \right\rangle = \frac{1}{v_\star} \,\mathrm{erf}\left(\frac{v_\star}{\sqrt{2} v_0}\right) \simeq \sqrt{\frac{2}{\pi}} \frac{1}{v_0} \tag{E.7}$$

where the last equality applies for $v_\star \ll v_0$.

F Resonant scalar emission

Though the main subject of this paper is dark matter scattering, our self-energy calculations can also be applied to particle emission rates, as per [36]. As an illustrative example, our calculations show that the rate for resonant (electron-coupled) scalar emission from SN1987A in the literature, calculated in [73], is parametrically too large. This is because [73] takes the $\Pi^{\phi L}$ mixing self-energy to be $\propto m_e^{\mathrm{eff}}$, where $m_e^{\mathrm{eff}} \simeq 12\,\mathrm{MeV}$ is the 'effective electron mass' in the supernova core [131]. However, as we derived in Appendix C, the mixing self-energy is actually $\sim m_e(1 + \mathcal{O}(e))$, where m_e is the in-vacuum electron mass. Physically, this is because the mixing requires a chirality flip, and so an insertion of the fermion mass (the in-medium 'effective mass' does not mix chiralities, but is simply a parameterization of how far the dispersion relation lies from the light-cone). Numerically,

this will result in a resonant emission rate ~ 500 times smaller than calculated in [73], for an equivalent scalar-electron coupling. We leave a fuller calculation of the emission rate, and its consequence for scalar coupling constraints, to future work.

References

[1] D. Gonzalez and A. Reisenegger, *Internal heating of old neutron stars: contrasting different mechanisms*, *A&A Astrophysics* **522** (oct, 2010) A16.

[2] M. Baryakhtar, J. Bramante, S. W. Li, T. Linden and N. Raj, *Dark kinetic heating of neutron stars and an infrared window on WIMPs, SIMPs, and pure higgsinos*, *Phys. Rev. Lett.* **119** (sep, 2017) .

[3] N. Raj, P. Tanedo and H.-B. Yu, *Neutron stars at the dark matter direct detection frontier*, *Phys. Rev. D* **97** (feb, 2018) .

[4] N. F. Bell, G. Busoni and S. Robles, *Heating up neutron stars with inelastic dark matter*, *J. Cosmol. Astropart. Phys.* **2018** (sep, 2018) 018–018.

[5] D. A. Camargo, F. S. Queiroz and R. Sturani, *Detecting dark matter with neutron star spectroscopy*, *J. Cosmol. Astropart. Phys.* **2019** (sep, 2019) 051–051.

[6] N. F. Bell, G. Busoni and S. Robles, *Capture of leptophilic dark matter in neutron stars*, *J. Cosmol. Astropart. Phys.* **2019** (jun, 2019) 054–054.

[7] R. Garani and J. Heeck, *Dark matter interactions with muons in neutron stars*, *Phys. Rev. D* **100** (aug, 2019) .

[8] J. F. Acevedo, J. Bramante, R. K. Leane and N. Raj, *Warming nuclear pasta with dark matter: kinetic and annihilation heating of neutron star crusts*, *J. Cosmol. Astropart. Phys.* **2020** (mar, 2020) 038–038.

[9] A. Joglekar, N. Raj, P. Tanedo and H.-B. Yu, *Relativistic capture of dark matter by electrons in neutron stars*, *Physics Letters B* **809** (oct, 2020) 135767.

[10] C. Kouvaris, *WIMP annihilation and cooling of neutron stars*, *Phys. Rev. D* **77** (jan, 2008) .

[11] G. Bertone and M. Fairbairn, *Compact stars as dark matter probes*, *Phys. Rev. D* **77** (feb, 2008) .

[12] C. Kouvaris and P. Tinyakov, *Can neutron stars constrain dark matter?*, *Phys. Rev. D* **82** (sep, 2010) .

[13] I. Goldman and S. Nussinov, *Weakly interacting massive particles and neutron stars*, *Phys. Rev. D* **40** (nov, 1989) 3221–3230.

[14] C. Kouvaris and P. Tinyakov, *Constraining asymmetric dark matter through observations of compact stars*, *Phys. Rev. D* **83** (apr, 2011) .

[15] C. Kouvaris and P. Tinyakov, *Excluding light asymmetric bosonic dark matter*, *Phys. Rev. Lett.* **107** (aug, 2011) .

[16] S. D. McDermott, H.-B. Yu and K. M. Zurek, *Constraints on scalar asymmetric dark matter from black hole formation in neutron stars*, *Phys. Rev. D* **85** (jan, 2012) .

[17] T. Güver, A. E. Erkoca, M. H. Reno and I. Sarcevic, *On the capture of dark matter by neutron stars*, *J. Cosmol. Astropart. Phys.* **2014** (may, 2014) 013–013.

[18] N. F. Bell, A. Melatos and K. Petraki, *Realistic neutron star constraints on bosonic asymmetric dark matter*, *Phys. Rev. D* **87** (jun, 2013) .

[19] J. Bramante, K. Fukushima, J. Kumar and E. Stopnitzky, *Bounds on self-interacting fermion dark matter from observations of old neutron stars*, *Phys. Rev. D* **89** (jan, 2014) .

[20] B. Bertoni, A. E. Nelson and S. Reddy, *Dark matter thermalization in neutron stars*, *Phys. Rev. D* **88** (dec, 2013) .

[21] R. Garani, Y. Genolini and T. Hambye, *New analysis of neutron star constraints on asymmetric dark matter*, *J. Cosmol. Astropart. Phys.* **2019** (may, 2019) 035–035.

[22] R. Garani, A. Gupta and N. Raj, *Observing the thermalization of dark matter in neutron stars*, *Phys. Rev. D* **103** (2021) 043019, [2009.10728].

[23] S. A. R. Ellis, *Premature Black Hole Death of Population III Stars by Dark Matter*, 2111.02414.

[24] A. C. Vincent, *Dark matter in stars*, 2009.00663.

[25] A. Gould and G. Raffelt, *Thermal conduction by massive particles*, *ApJ* **352** (apr, 1990) 654.

[26] A. Gould and G. Raffelt, *Cosmion energy transfer in stars - the knudsen limit*, *ApJ* **352** (apr, 1990) 669.

[27] A. C. Vincent and P. Scott, *Thermal conduction by dark matter with velocity and momentum-dependent cross-sections*, *J. Cosmol. Astropart. Phys.* **2014** (apr, 2014) 019–019.

[28] B. Geytenbeek, S. Rao, P. Scott, A. Serenelli, A. C. Vincent, M. White et al., *Effect of electromagnetic dipole dark matter on energy transport in the solar interior*, *J. Cosmol. Astropart. Phys.* **2017** (mar, 2017) 029–029.

[29] J. Casanellas and I. Lopes, *FIRST ASTEROSEISMIC LIMITS ON THE NATURE OF DARK MATTER*, *ApJ* **765** (feb, 2013) L21.

[30] J. Casanellas, I. Brandão and Y. Lebreton, *Stellar convective cores as dark matter probes*, *Phys. Rev. D* **91** (may, 2015) .

[31] A. Martins, I. Lopes and J. Casanellas, *Asteroseismic constraints on asymmetric dark matter: Light particles with an effective spin-dependent coupling*, *Phys. Rev. D* **95** (jan, 2017) .

[32] G. B. Gelmini, V. Takhistov and E. Vitagliano, *Scalar direct detection: In-medium effects*, *Physics Letters B* **809** (oct, 2020) 135779.

[33] Y. Hochberg, Y. Kahn, N. Kurinsky, B. V. Lehmann, T. C. Yu and K. K. Berggren, *Determining dark-matter–electron scattering rates from the dielectric function*, *Phys. Rev. Lett.* **127** (oct, 2021) .

[34] S. Knapen, J. Kozaczuk and T. Lin, *Dark matter-electron scattering in dielectrics*, *Phys. Rev. D* **104** (jul, 2021) .

[35] R. Lasenby and A. Prabhu, *DM-electron scattering in materials: sum rules and heterostructures*, 2110.01587.

[36] E. Hardy and R. Lasenby, *Stellar cooling bounds on new light particles: plasma mixing effects*, *JHEP* **02** (2017) 033, [1611.05852].

[37] S. M. Girvin and K. Yang, *Modern Condensed Matter Physics*. Cambridge University Press, Feb., 2019, 10.1017/9781316480649.

[38] B. Holdom, *Two u(1)'s and ϵ charge shifts*, *Physics Letters B* **166** (Jan., 1986) 196–198.

[39] J. Redondo and G. Raffelt, *Solar constraints on hidden photons re-visited*, *J. Cosmol. Astropart. Phys.* **2013** (aug, 2013) 034–034.

[40] M. L. Bellac, *Thermal Field Theory*. Cambridge University Press, Aug, 1996, 10.1017/cbo9780511721700.

[41] N. F. Bell, G. Busoni, S. Robles and M. Virgato, *Improved treatment of dark matter capture in neutron stars*, *Journal of Cosmology and Astroparticle Physics* **2020** (Sept., 2020) 028–028.

[42] M. Salaris, E. Garcia-Berro, M. Hernanz, J. Isern and D. Saumon, *The ages of very cool hydrogen-rich white dwarfs*, *ApJ* **544** (dec, 2000) 1036–1043.

[43] D. L. Kaplan, J. Boyles, B. H. Dunlap, S. P. Tendulkar, A. T. Deller, S. M. Ransom et al., *A 1.05m COMPANION TO PSR j2222–0137: THE COOLEST KNOWN WHITE DWARF?*, *ApJ* **789** (jun, 2014) 119.

[44] P. Amaro-Seoane, J. Casanellas, R. Schödel, E. Davidson and J. Cuadra, *Probing dark matter crests with white dwarfs and IMBHs*, *Mon. Not. R. Astron. Soc.* **459** (mar, 2016) 695–700.

[45] G. Panotopoulos and I. Lopes, *Constraints on light dark matter particles using white dwarf stars*, *Int. J. Mod. Phys. D* **29** (jun, 2020) 2050058.

[46] N. F. Bell, G. Busoni, M. E. Ramirez-Quezada, S. Robles and M. Virgato, *Improved treatment of dark matter capture in white dwarfs*, *Journal of Cosmology and Astroparticle Physics* **2021** (Oct., 2021) 083.

[47] P. W. Graham, R. Janish, V. Narayan, S. Rajendran and P. Riggins, *White dwarfs as dark matter detectors*, *Phys. Rev. D* **98** (dec, 2018) .

[48] M. A. Fedderke, P. W. Graham and S. Rajendran, *White dwarf bounds on charged massive particles*, *Phys. Rev. D* **101** (jun, 2020) .

[49] P. W. Graham, S. Rajendran and J. Varela, *Dark matter triggers of supernovae*, *Phys. Rev. D* **92** (sep, 2015) .

[50] B. M. Hansen and J. Liebert, *Cool white dwarfs*, *Annu. Rev. Astron. Astrophys.* **41** (sep, 2003) 465–515.

[51] G. Gabadadze and R. A. Rosen, *Charged condensate and helium dwarf stars*, *J. Cosmol. Astropart. Phys.* **2008** (oct, 2008) 030.

[52] G. Raffelt, *Stars as laboratories for fundamental physics: The astrophysics of neutrinos, axions, and other weakly interacting particles*. University of Chicago Press, 5, 1996.

[53] G. D. Mahan, *Condensed Matter in a Nutshell*. Princeton University Press, dec, 2011, 10.1515/9781400837021.

[54] S. L. Shapiro and S. A. Teukolsky, *Black Holes, White Dwarfs, and Neutron Stars*. Wiley, July, 1983, 10.1002/9783527617661.

[55] S. M. Griffin, K. Inzani, T. Trickle, Z. Zhang and K. M. Zurek, *Multichannel direct detection of light dark matter: Target comparison*, *Phys. Rev. D* **101** (mar, 2020) .

[56] A. Coskuner, T. Trickle, Z. Zhang and K. M. Zurek, *Directional detectability of dark matter with single phonon excitations: Target comparison*, *Physical Review D* **105** (Jan., 2022) .

[57] N. W. Ashcroft and N. D. Mermin, *Solid State Physics*. Holt-Saunders, 1976.

[58] R. Garani and S. Palomares-Ruiz, *Evaporation of dark matter from celestial bodies*, 2104.12757.

[59] P. Agnes, I. Albuquerque, T. Alexander, A. Alton, G. Araujo, D. Asner et al., *Constraints on sub-GeV dark-matter–electron scattering from the DarkSide-50 experiment*, *Phys. Rev. Lett.* **121** (sep, 2018) .

[60] J. Angle, E. Aprile, F. Arneodo, L. Baudis, A. Bernstein, A. I. Bolozdynya et al., *Search for light dark matter in XENON10 data*, *Phys. Rev. Lett.* **107** (jul, 2011) .

[61] E. Aprile, J. Aalbers, F. Agostini, M. Alfonsi, F. Amaro, M. Anthony et al., *Low-mass dark matter search using ionization signals in XENON100*, *Phys. Rev. D* **94** (nov, 2016) .

[62] G. Angloher, P. Bauer, A. Bento, C. Bucci, L. Canonica, X. Defay et al., *Results on MeV-scale dark matter from a gram-scale cryogenic calorimeter operated above ground*, *Eur. Phys. J. C* **77** (sep, 2017) .

[63] F. Petricca, G. Angloher, P. Bauer, A. Bento, C. Bucci, L. Canonica et al., *First results on low-mass dark matter from the CRESST-III experiment*, 1711.07692.

[64] R. Agnese, A. Anderson, T. Aramaki, M. Asai, W. Baker, D. Balakishiyeva et al., *New results from the search for low-mass weakly interacting massive particles with the CDMS low ionization threshold experiment*, *Phys. Rev. Lett.* **116** (feb, 2016) .

[65] D. Akerib, S. Alsum, H. Araújo, X. Bai, A. Bailey, J. Balajthy et al., *Results from a search for dark matter in the complete LUX exposure*, *Phys. Rev. Lett.* **118** (jan, 2017) .

[66] M. Crisler, R. Essig, J. Estrada, G. Fernandez, J. Tiffenberg, M. S. Haro et al., *SENSEI: First direct-detection constraints on sub-GeV dark matter from a surface run*, *Physical Review Letters* **121** (Aug., 2018) .

[67] O. Abramoff, L. Barak, I. M. Bloch, L. Chaplinsky, M. Crisler, Dawa et al., *SENSEI: Direct-detection constraints on sub-GeV dark matter from a shallow underground run using a prototype skipper CCD*, *Phys. Rev. Lett.* **122** (apr, 2019) .

[68] L. Barak, I. M. Bloch, M. Cababie, G. Cancelo, L. Chaplinsky, F. Chierchie et al., *SENSEI: Direct-detection results on sub-GeV dark matter from a new skipper CCD*, *Phys. Rev. Lett.* **125** (oct, 2020) .

[69] R. Agnese, A. Anderson, T. Aramaki, I. Arnquist, W. Baker, D. Barker et al., *Projected sensitivity of the SuperCDMS SNOLAB experiment*, *Phys. Rev. D* **95** (apr, 2017) .

[70] J. L. Feng and J. Smolinsky, *Impact of a resonance on thermal targets for invisible dark photon searches*, *Phys. Rev. D* **96** (nov, 2017) .

[71] C. Giovanetti, M. Lisanti, H. Liu and J. T. Ruderman, *Joint CMB and BBN Constraints on Light Dark Sectors with Dark Radiation*, 2109.03246.

[72] J. H. Chang, R. Essig and S. D. McDermott, *Supernova 1987a constraints on sub-GeV dark sectors, millicharged particles, the QCD axion, and an axion-like particle*, *J. High Energ. Phys.* **2018** (sep, 2018) .

[73] S. Knapen, T. Lin and K. M. Zurek, *Light Dark Matter: Models and Constraints*, *Phys. Rev. D* **96** (2017) 115021, [1709.07882].

[74] B. Batell, M. Pospelov and A. Ritz, *Exploring portals to a hidden sector through fixed targets*, *Phys. Rev. D* **80** (nov, 2009) .

[75] B. Batell, R. Essig and Z. Surujon, *Strong constraints on sub-GeV dark sectors from SLAC beam dump e137*, *Phys. Rev. Lett.* **113** (oct, 2014) .

[76] J. P. L. et al, *Search for invisible decays of a dark photon produced in e + e- collisions at babar*, *Phys. Rev. Lett.* **119** (sep, 2017) .

[77] K. Blum and D. Kushnir, *NEUTRINO SIGNAL OF COLLAPSE-INDUCED THERMONUCLEAR SUPERNOVAE: THE CASE FOR PROMPT BLACK HOLE FORMATION IN SN 1987a*, *ApJ* **828** (aug, 2016) 31.

[78] J. A. Dror, R. Lasenby and M. Pospelov, *Dark forces coupled to nonconserved currents*, *Phys. Rev. D* **96** (oct, 2017) .

[79] P. W. Graham, D. E. Kaplan, J. Mardon, S. Rajendran and W. A. Terrano, *Dark matter direct detection with accelerometers*, *Phys. Rev. D* **93** (apr, 2016) .

[80] J. Fan, A. Katz and J. Shelton, *Direct and indirect detection of dissipative dark matter*, *J. Cosmol. Astropart. Phys.* **2014** (jun, 2014) 059–059.

[81] E. Hardy and R. Lasenby, *Stellar cooling bounds on new light particles: plasma mixing effects*, *Journal of High Energy Physics* **2017** (Feb, 2017) .

[82] H. An, M. Pospelov and J. Pradler, *New stellar constraints on dark photons*, *Phys. Lett. B* **725** (2013) 190–195, [1302.3884].

[83] H. Vogel and J. Redondo, *Dark radiation constraints on minicharged particles in models with a hidden photon*, *J. Cosmol. Astropart. Phys.* **2014** (feb, 2014) 029–029.

[84] R. Essig, A. Manalaysay, J. Mardon, P. Sorensen and T. Volansky, *First direct detection limits on sub-GeV dark matter from XENON10*, *Phys. Rev. Lett.* **109** (jul, 2012) .

[85] R. Essig, T. Volansky and T.-T. Yu, *New constraints and prospects for sub-GeV dark matter scattering off electrons in xenon*, *Phys. Rev. D* **96** (aug, 2017) .

[86] A. Stebbins and G. Krnjaic, *New limits on charged dark matter from large-scale coherent magnetic fields*, *J. Cosmol. Astropart. Phys.* **2019** (dec, 2019) 003–003.

[87] L. Chuzhoy and E. W. Kolb, *Reopening the window on charged dark matter*, *J. Cosmol. Astropart. Phys.* **2009** (jul, 2009) 014–014.

[88] S. D. McDermott, H.-B. Yu and K. M. Zurek, *Turning off the lights: How dark is dark matter?*, *Phys. Rev. D* **83** (mar, 2011) .

[89] K. Kadota, T. Sekiguchi and H. Tashiro, *A new constraint on millicharged dark matter from galaxy clusters*, 1602.04009.

[90] P.-K. Hu, A. Kusenko and V. Takhistov, *Dark cosmic rays*, *Physics Letters B* **768** (may, 2017) 18–22.

[91] D. Dunsky, L. J. Hall and K. Harigaya, *CHAMP cosmic rays*, *J. Cosmol. Astropart. Phys.* **2019** (jul, 2019) 015–015.

[92] R. Lasenby, *Long range dark matter self-interactions and plasma instabilities*, *J. Cosmol. Astropart. Phys.* **2020** (nov, 2020) 034–034.

[93] M. Baryakhtar, J. Bramante, S. W. Li, T. Linden and N. Raj, *Dark kinetic heating of*

neutron stars and an infrared window on WIMPs, SIMPs, and pure higgsinos, *Phys. Rev. Lett.* **119** (sep, 2017) .

[94] H. Heiselberg and V. Pandharipande, *Recent progress in neutron star theory*, *Annu. Rev. Nucl. Part. Sci.* **50** (dec, 2000) 481–524.

[95] F. Weber, *Strange quark matter and compact stars*, *Progress in Particle and Nuclear Physics* **54** (mar, 2005) 193–288.

[96] K. Rajagopal and F. Wilczek, *Enforced electrical neutrality of the color flavor locked phase*, *Phys. Rev. Lett.* **86** (2001) 3492–3495, [hep-ph/0012039].

[97] J. C. D'Olivo and J. F. Nieves, *Nucleon effects on the photon dispersion relations in matter*, *Physical Review D* **57** (Mar., 1998) 3116–3130.

[98] N. F. Bell, G. Busoni, S. Robles and M. Virgato, *Improved treatment of dark matter capture in neutron stars II: leptonic targets*, *Journal of Cosmology and Astroparticle Physics* **2021** (Mar., 2021) 086.

[99] C. McCabe, *Astrophysical uncertainties of dark matter direct detection experiments*, *Physical Review D* **82** (July, 2010) .

[100] H. An, M. Pospelov, J. Pradler and A. Ritz, *Directly detecting MeV-scale dark matter via solar reflection*, *Phys. Rev. Lett.* **120** (apr, 2018) .

[101] H. An, H. Nie, M. Pospelov, J. Pradler and A. Ritz, *Solar reflection of dark matter*, *Phys. Rev. D* **104** (nov, 2021) .

[102] C. Kouvaris, *Probing light dark matter via evaporation from the sun*, *Phys. Rev. D* **92** (oct, 2015) .

[103] T. Tanaka, K. Abe, Y. Hayato, T. Iida, J. Kameda, Y. Koshio et al., *AN INDIRECT SEARCH FOR WEAKLY INTERACTING MASSIVE PARTICLES IN THE SUN USING 3109.6 DAYS OF UPWARD-GOING MUONS IN SUPER-KAMIOKANDE*, *ApJ* **742** (nov, 2011) 78.

[104] T. S.-K. Collaboration, :, K. Choi, K. Abe, Y. Haga, Y. Hayato et al., *Search for neutrinos from annihilation of captured low-mass dark matter particles in the sun by super-kamiokande*, 1503.04858.

[105] S. Adrián-Martínez, A. Albert, M. André, G. Anton, M. Ardid, J.-J. Aubert et al., *A search for secluded dark matter in the sun with the ANTARES neutrino telescope*, *J. Cosmol. Astropart. Phys.* **2016** (may, 2016) 016–016.

[106] S. Adrián-Martínez, A. Albert, M. André, G. Anton, M. Ardid, J.-J. Aubert et al., *Limits on dark matter annihilation in the sun using the ANTARES neutrino telescope*, *Physics Letters B* **759** (aug, 2016) 69–74.

[107] M. G. Aartsen, M. Ackermann, J. Adams, J. A. Aguilar, M. Ahlers, M. Ahrens et al., *Search for annihilating dark matter in the sun with 3 years of IceCube data*, *Eur. Phys. J. C* **77** (mar, 2017) .

[108] P. Schuster, N. Toro and I. Yavin, *Terrestrial and solar limits on long-lived particles in a dark sector*, *Phys. Rev. D* **81** (jan, 2010) .

[109] N. F. Bell and K. Petraki, *Enhanced neutrino signals from dark matter annihilation in the sun via metastable mediators*, *J. Cosmol. Astropart. Phys.* **2011** (apr, 2011) 003–003.

[110] J. L. Feng, J. Smolinsky and P. Tanedo, *Detecting dark matter through dark photons from the sun: Charged particle signatures*, *Phys. Rev. D* **93** (jun, 2016) .

[111] R. K. Leane, K. C. Ng and J. F. Beacom, *Powerful solar signatures of long-lived dark mediators*, *Phys. Rev. D* **95** (jun, 2017) .

[112] J. N. Bahcall, A. M. Serenelli and S. Basu, *New solar opacities, abundances, helioseismology, and neutrino fluxes*, *The Astrophysical Journal* **621** (Jan., 2005) L85–L88.

[113] M. Asplund, N. Grevesse, A. J. Sauval and P. Scott, *The chemical composition of the sun*, *Annual Review of Astronomy and Astrophysics* **47** (Sept., 2009) 481–522.

[114] R. Fitzpatrick, *Plasma physics : an introduction*. CRC Press, Taylor & Francis Group, 2015.

[115] C. Gaidau and J. Shelton, *Singularities in the gravitational capture of dark matter through long-range interactions*, 2110.02234.

[116] A. Berlin and K. Schutz, *A helioscope for gravitationally bound millicharged particles*, 2111.01796.

[117] L. DiLella and K. Zioutas, *Observational evidence for gravitationally trapped massive axion(-like) particles*, *Astroparticle Physics* **19** (apr, 2003) 145–170.

[118] B. Morgan, N. Spooner, M. Armel-Funkhouser, D. Hoffmann, J. Jacoby, D. Snowden-Ifft et al., *Searches for solar kaluza–klein axions with gas TPCs*, *Astroparticle Physics* **23** (apr, 2005) 287–302.

[119] and N Oka, K. Abe, K. Hiraide, K. Ichimura, Y. Kishimoto, K. Kobayashi et al., *Search for solar kaluza–klein axions by annual modulation with the XMASS-i detector*, *Progress of Theoretical and Experimental Physics* **2017** (oct, 2017) .

[120] K. V. Tilburg, *Stellar basins of gravitationally bound particles*, *Phys. Rev. D* **104** (jul, 2021) .

[121] R. Lasenby and K. V. Tilburg, *Dark photons in the solar basin*, *Phys. Rev. D* **104** (jul, 2021) .

[122] D. Smith and N. Weiner, *Inelastic dark matter*, *Physical Review D* **64** (July, 2001) .

[123] M. Baryakhtar, A. Berlin, H. Liu and N. Weiner, *Electromagnetic Signals of Inelastic Dark Matter Scattering*, 2006.13918.

[124] H. Vogel and J. Redondo, *Dark radiation constraints on minicharged particles in models with a hidden photon*, *J. Cosmol. Astropart. Phys.* **2014** (feb, 2014) 029–029.

[125] C. Dvorkin, T. Lin and K. Schutz, *Making dark matter out of light: Freeze-in from plasma effects*, *Phys. Rev. D* **99** (jun, 2019) .

[126] C. Dvorkin, T. Lin and K. Schutz, *Cosmology of sub-MeV dark matter freeze-in*, *Phys. Rev. Lett.* **127** (sep, 2021) .

[127] L. Ackerman, M. R. Buckley, S. M. Carroll and M. Kamionkowski, *Dark matter and dark radiation*, *Physical Review D* **79** (Jan., 2009) .

[128] P. Agrawal, F.-Y. Cyr-Racine, L. Randall and J. Scholtz, *Make dark matter charged again*, *Journal of Cosmology and Astroparticle Physics* **2017** (May, 2017) 022–022.

[129] E. Braaten and D. Segel, *Neutrino energy loss from the plasma process at all temperatures and densities*, *Physical Review D* **48** (Aug., 1993) 1478–1491.

[130] B. D. Fried and S. D. Conte, *The Plasma Dispersion Function*. Elsevier, 1961, 10.1016/c2013-0-12176-9.

[131] E. Braaten, *Neutrino emissivity of an ultrarelativistic plasma from positron and plasmino annihilation*, *ApJ* **392** (jun, 1992) 70.

[132] O. V. Dolgov, D. A. Kirzhnits and E. G. Maksimov, *On an admissible sign of the static dielectric function of matter*, *Rev. Mod. Phys.* **53** (jan, 1981) 81–93.

[133] N. W. Evans and J. H. An, *Distribution function of dark matter*, *Phys. Rev. D* **73** (jan, 2006) .

[134] R. Wojtak, E. L. Łokas, G. A. Mamon, S. Gottlöber, A. Klypin and Y. Hoffman, *The distribution function of dark matter in massive haloes*, *Monthly Notices of the Royal Astronomical Society* **388** (aug, 2008) 815–828.

[135] A. D. Ludlow, J. F. Navarro, S. D. M. White, M. Boylan-Kolchin, V. Springel, A. Jenkins et al., *The density and pseudo-phase-space density profiles of cold dark matter haloes*, *Monthly Notices of the Royal Astronomical Society* **415** (jun, 2011) 3895–3902.

[136] D. Lemze, R. Wagner, Y. Rephaeli, S. Sadeh, M. L. Norman, R. Barkana et al., *PROFILES OF DARK MATTER VELOCITY ANISOTROPY IN SIMULATED CLUSTERS*, *ApJ* **752** (jun, 2012) 141.

[137] M. Sparre and S. H. Hansen, *The behaviour of shape and velocity anisotropy in dark matter haloes*, *J. Cosmol. Astropart. Phys.* **2012** (oct, 2012) 049–049.

[138] R. Wojtak, S. Gottlöber and A. Klypin, *Orbital anisotropy in cosmological haloes revisited*, *Monthly Notices of the Royal Astronomical Society* **434** (jul, 2013) 1576–1585.

[139] M. Lisanti, *Lectures on dark matter physics*, in *New Frontiers in Fields and Strings*, WORLD SCIENTIFIC, nov, 2016. DOI.